AFRL-RQ-WP-TR-2015-0040

QUANTITATIVE TECHNOLOGY ASSESSMENT (QTA)
Delivery Order 0007: Vehicle Design Technology Developments for Uninhabited Aerial Systems (UAS)

Richard V. Beblo, John Puttmann, and Cody Ray

University of Dayton Research Institute

FEBRUARY 2015
Final Report

STINFO COPY

AIR FORCE RESEARCH LABORATORY
AEROSPACE SYSTEMS DIRECTORATE
WRIGHT-PATTERSON AIR FORCE BASE, OH 45433-7541
AIR FORCE MATERIEL COMMAND
UNITED STATES AIR FORCE

NOTICE AND SIGNATURE PAGE

*//Signature//

GREGORY W. REICH
Aerospace Engineer
Design and Analysis Branch
Aerospace Vehicles Division

//Signature//

MARK D. GABBARD, Chief
Design and Analysis Branch
Aerospace Vehicles Division

//Signature//

PHILIP S. BERAN
Branch Technical Advisor
Aerospace Vehicles Division
Aerospace Systems Directorate

REPORT DOCUMENTATION PAGE

1. REPORT DATE *(DD-MM-YY)*	2. REPORT TYPE	3. DATES COVERED *(From - To)*
February 2015	Final	23 November 2011 – 30 November 2014

4. TITLE AND SUBTITLE

QUANTITATIVE TECHNOLOGY ASSESSMENT (QTA)
Delivery Order 0007: Vehicle Design Technology Developments for Uninhabited Aerial Systems (UAS)

5a. CONTRACT NUMBER
FA8650-09-D-3944-0007

5b. GRANT NUMBER

5c. PROGRAM ELEMENT NUMBER
62201F

6. AUTHOR(S)

Richard V. Beblo, John Puttmann, and Cody Ray

5d. PROJECT NUMBER
2401

5e. TASK NUMBER

5f. WORK UNIT NUMBER
Q12T

7. PERFORMING ORGANIZATION NAME(S) AND ADDRESS(ES)

University of Dayton Research Institute
Aerospace Mechanics Division
300 College Park
Dayton, OH 45469-0013

8. PERFORMING ORGANIZATION REPORT NUMBER

9. SPONSORING/MONITORING AGENCY NAME(S) AND ADDRESS(ES)

Air Force Research Laboratory
Aerospace Systems Directorate
Wright-Patterson Air Force Base, OH 45433-7541
Air Force Materiel Command
United States Air Force

10. SPONSORING/MONITORING AGENCY ACRONYM(S)
AFRL/RQVC

11. SPONSORING/MONITORING AGENCY REPORT NUMBER(S)
AFRL-RQ-WP-TR-2015-0040

12. DISTRIBUTION/AVAILABILITY STATEMENT
Approved for public release; distribution unlimited.

13. SUPPLEMENTARY NOTES
PA Case Number: 88ABW-2015-1236; Clearance Date: 19 Mar 2015.

14. ABSTRACT

Reconfigurable structures have been the topic of much research in recent years. Articulation, mechanisms, skin materials, and sensory systems to increase maneuverability and flight mission performance have all been studied. In this report, a particular type of artificial hair sensor is studied for use as a flow sensor for advanced maneuvering. Additionally, skins for reconfigurable wings are considered in terms of a cellular structure filled with a variable stiffness material, such as honeycomb filled with shape memory polymer (SMP).

15. SUBJECT TERMS
reconfigurable skins, morphing aircraft, artificial hair sensors

16. SECURITY CLASSIFICATION OF:			17. LIMITATION OF ABSTRACT:	18. NUMBER OF PAGES	19a. NAME OF RESPONSIBLE PERSON (Monitor)
a. REPORT Unclassified	**b. ABSTRACT** Unclassified	**c. THIS PAGE** Unclassified	SAR	100	Gregory W. Reich 19b. TELEPHONE NUMBER *(Include Area Code)* N/A

TABLE OF CONTENTS

Section   Page

Approved for public release; distribution unlimited.

LIST OF FIGURES

Approved for public release; distribution unlimited.

LIST OF TABLES

FOREWORD

1   EXECUTIVE SUMMARY

Reconfigurable structures have been the topic of much research in recent years. Articulation, mechanisms, skin materials, and sensory systems to increase maneuverability and flight mission performance have all been studied. In this report, a particular type of artificial hair sensor is studied for use as a flow sensor for advanced maneuvering. Additionally, skins for reconfigurable wings are considered in terms of a cellular structure filled with a variable stiffness material, such as honeycomb filled with shape memory polymer (SMP). The presented work outlines an investigative effort to determine the feasibility of such a system, mechanically characterize the system given chosen candidate materials, and develop an optimization scheme for tailoring the system to specific applications. The chosen candidate materials of epoxy SMP and aluminum honeycomb are individually characterized. Using these materials, the Young's moduli and shear moduli of the filled honeycomb composite are also experimentally determined above and below the transition temperature of the polymer. These results are then used to validate an analytical model taking into account the geometry of the honeycomb. A finite element analysis (FEA) is also presented for comparison with the experimental results and analytic model. Once validated, the analytic model is then used in an optimization scheme to optimize the honeycomb geometry given an assumed set of constraints and desired skin properties. Finally, limitations of each element of the analysis and future work are discussed.

2 ENERGY-BASED RECONFIGURABLE MICRO-AERIAL VEHICLE (MAV) FLIGHT STRUCTURES DESIGN

2.1 Background

Although robust control strategies have improved flight system performance in the presence of unmodeled disturbances such as gusts, aircraft are nonetheless susceptible to disturbances that cause significant departure from linear behavior. In this work, artificial hair sensor array feedback is combined and utilized in a recurrent neural network (RNN) approach to predict airfoil loading as a consequence of incident gusts. It is demonstrated that with proper recurrent neural network architecture, distributed sensory array information can be effectively combined and utilized to predict disturbances in lift and moment. Such results indicate that empirical learning-based approaches to utilizing uncharacterized, massive arrays of flow sensors may be both practical and beneficial.

2.2 Introduction

Despite their success, engineered flight systems have yet to achieve the performance of biological flying systems in terms of maneuverability, efficiency and robustness to disturbances. Robust control strategies for flight systems have been developed that provide improved stability and performance; however, such systems are susceptible to unmodeled disturbances such as gusts. In this work, an approach to disturbance awareness using RNNs and distributed artificial hair sensor feedback is developed. Specifically, an RNN is used to estimate body reaction (in terms of force and moment) to flow disturbances using spatially distributed artificial hair sensor feedback.

Biological systems present a variety of sensory adaptations that potentially provide the same, or very similar, information engineered flight systems require to achieve performance similar to their biological counterparts. For instance, the bat may use muscle and hair sensor feedback to achieve extraordinary flight performance [1, 2]. In fact, hair sensors may be the most sensitive sensory modality developed in nature [3]. In response to these observations, engineers have begun developing insect-grade flow sensors – cheap, numerous and uncharacterized sensors – and investigating potential benefits of fly-by-feel flight systems. Algorithms and hardware that can deal effectively with massively distributed and uncharacterized sensory arrays will be necessary for such systems to come to fruition.

Engineered flying systems currently utilize sensors for situational awareness and state/parameter estimation, but the number of sensors is limited and the sensors are comparatively expensive. As such, emphasis is placed on point-wise sensor accuracy rather than redundancy. Sensor redundancy is not only useful but necessary for biological systems [4, 5]. There are several reasons to consider highly redundant, distributed sensory systems for flight control. First and foremost, redundancy provides robustness to sensor failure – a systemic problem in systems with very few high-grade sensors. Redundancy also provides more information regarding estimated quantities. In contrast to engineered systems, biology generally employs enormous levels of redundancy in both control and estimation systems [6].

As described later, the flow features of interest here take the form of wind-vector fields over an aircraft. Such features are inherently nonlinear, spatially distributed, and unsteady. An accurate

physics-based model that describes these features exists, but a real-time solution of the nonlinear Navier-Stokes equations is computationally intractable at this time. Nevertheless, such flow features are easily observable by a variety of sensor types and lend themselves immediately to very successful empirical approaches that utilize them directly for flow and aircraft state estimation [7, 8]. Flow fields incident on an aircraft contain information regarding aircraft state and relative wind. Temporal variations in flow topology may also serve as a means for prediction of fluid-body interaction. For instance, temporal and spatial variations in distributed hair sensor signals may provide reliable prediction of an impending consequential flow-state change. At the very least, such signals are intimately related to aircraft body forces and moments, as described in [7, 8] and the references therein. Hence, RNNs are investigated as a means to provide both state and parameter estimates, as well as a means of predicting future body forces and moments – a capability conducive to a fly-by-feel paradigm.

2.3   Flow Features, Artificial Hair Sensors, and Distributed Sensor Arrays

All flow sensing hairs have been found on many biological models, including, but not limited to, crickets, spiders, locusts, fish, and bats [1, 9, 10]. Such sensory adaptations are used for predator evasion, environmental awareness, and flight performance. Even blind fish have demonstrated the ability to school by using distributed hair-like sensors, a behavioral fact that indicates the use of distributed flow measurements [11]. Like most biological sensory modalities, these systems are generally fairly robust due to redundancy, material properties, directional sensitivity, and the adaptive nature of neurological systems. Hair sensors are a fairly new addition to the suite of anemometers, and function by measuring the mechanical response of a beam-like extension into a flow field. Drag from hair-flow interaction results in forces and moments, measured at the base of the hair, which are a function of the local flow velocity field. Output from hair sensors is a result of drag along the fully wetted hair surface and can be calculated as the moment integral of drag on the hair. A noteworthy review of hair-like sensors is provided in [10], with interesting experimental and theoretical analysis provided by [12, 13] and the references therein. Some groups have devised several designs for single and arrays of artificial hair flow-sensors, some of which have been implemented successfully in flow experiments [10, 14]. Until recently, most of the research has been limited to material and mechanical design studies. Several groups have now begun investigating identification of aerodynamic phenomena and aerodynamic control/estimation strategies that utilize artificial hair sensors [15, 16]. Computational analysis has yielded promising results indicating that such sensors can be used for boundary layer and flow estimation. In this work, we provide preliminary results indicating AHS do offer the capability for flow estimation and flow feature identification.

Furthermore, hair sensors offer the potential for observation beyond point measurements, providing direct access to observable flow features that result from fluid-structure interaction. Intuition and research suggest that flying animals likely react to flow structures as they are encountered and are doing so based on previous experience and memory. Such flow structures may be identifiable by observing patterns and features in the flow velocity field near and upon a body in flight. Thus, hair sensors may directly sense flow structures (and temporal variations thereof) as important features, or observables, to provide an organism a predictive capability to adjust control strategies to achieve a goal even in the face of changing flow conditions and disturbances.

When distributed arrays of flow sensors are used, observation of such features becomes similar to image or pattern recognition problems of artificial intelligence. Spatially distributed sensors enable imaging of flow feature observables, including stagnation, separation, and reattachment points (lines) such as those illustrated in Figure 1. Such features are intimately related to flight body state and stability and can thus be used for both control and estimation of meaningful parameters and states [8]. For instance, Mangalam et al. have developed a strategy for direct observation and real-time extraction of critical aerodynamic flow characteristics, loads, and moments from surface signatures [7, 8]. In their approach, hot-film anemometry is used to directly measure location of the flow features mentioned above, along with flow transition, turbulence, shock, vortices, etc. Related approaches such as that by Goman and Khrabrov in [17] demonstrated that unsteady lift, drag, and moments can be expressed as functions of the instantaneous separation point location, angle of attack, and pitch rate.
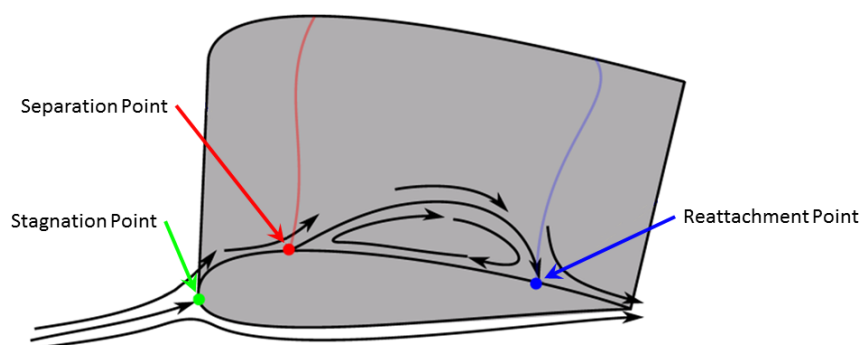
Figure 1: Stagnation, Separation, and Reattachment Flow Features

Fundamentally, all practical approaches can be described as striving to introduce a priori knowledge into an estimation scheme that will uniquely and robustly determine useful aerodynamic parameters. Therefore, it seems logical to consider whether or not the problem of aircraft state estimation and control can be enhanced by using a nonlinear system identification approach that utilizes a plethora of redundant sensors, rather than relying upon complex mathematical models requiring online numerical integration. After all, it seems nature is already solving the nonlinear equations of motion exactly; why burden engineered flight systems with mere approximations when such systems can instead feel their way through flight and at times, learn and adapt through experience. The complexity of dealing with hundreds, if not thousands, of spatially distributed sensors is traditionally either computationally burdensome or relies upon extensive offline statistical analysis and system identification. Although adaptive estimation and control methodologies exist for such applications, these generally still require physics-based models that do not exist (and may never) for such nonlinear problems. Neural networks stand as a strong candidate for alleviating the above challenges.

Consider a large array of sensors, with distributed neural networks to combine and adapt for each local group of sensors, the signals of which feed upward through an architecture similar to that shown in Figure 2. With sufficient theoretical understanding, the majority of computation could be performed locally. Local computation results could be fed upward into a traditional control design, modified to utilize such data. It is the author's opinion that traditional control methodologies shouldn't be replaced, but rather augmented with rich sensory feedback and learning-based architectures such as that presented here.
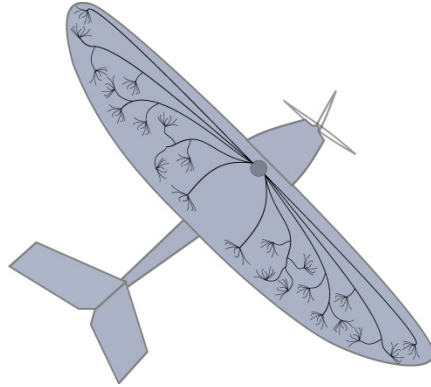
Figure 2: Biologically Inspired Sensory Architecture

2.4 Artificial Hair Sensor Principles

Artificial hair is strongly biologically inspired. It is now well-known that biological models utilize wind chill and/or microscopic hairs for wind orientation, turbulence detection, among other adaptations. For example bats may use hair for flow detection applications. D'Angelo et al. investigated bats' use of hair for turbulence and consequences of hair removal upon bat flight. Bat flight metrics experience degradation upon hair removal [1]. Other animals utilizing hair or hair-like structures for sensing flows include insects and fish [12, 11]. Hair as a sensor is a successful strategy in biology for multiple reasons including low mass-density and regrowth capability.

In light of the aforementioned biological discoveries, our group has designed and constructed artificial hair sensors from microscale glass fibers and carbon nanotubes. Figure 3 depicts a hair sensor undergoing deflection due to drag forces. As the hair is effectively cantilever from a surface, it protrudes within and potentially out of a boundary layer, as illustrated alongside the hair. Thus, fluid motion induces drag upon the hair, causing a moment and shear force to exist at the hair base. By growing carbon nanotubes along the hair contained within the glass pore, hair deflections can be made to cause changes in resistance due to nanotube deformations.

Approved for public release; distribution unlimited.
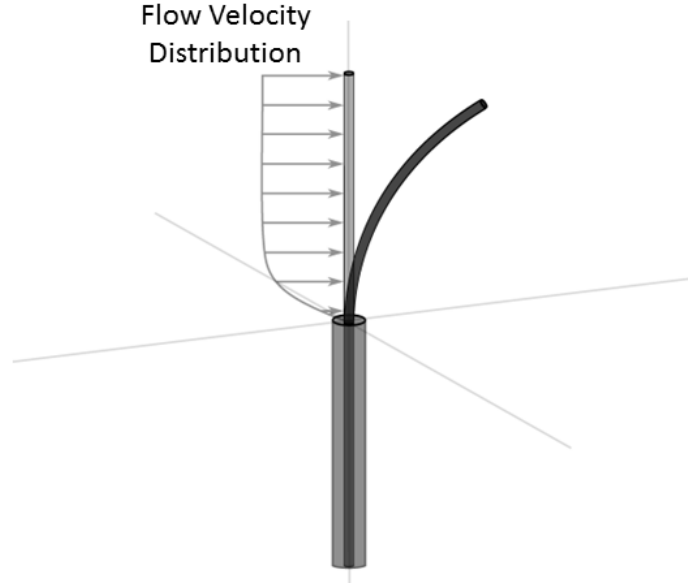
Figure 3: Artificial Hair Function Concept

To be specific, if a coordinate axis is set up such that elevation along the hair is represented by z, total hair height as z_h and drag upon the hair (drag normal to the hair axis as a function of z) represented by $\delta(z)$, the total drag upon the hair can be integrated to yield (for one dimension)

$$M_y = \int_0^{z_h} \delta(z)z \, dz \tag{1}$$

$$F_x = \int_0^{z_h} \delta(z) \, dz \tag{2}$$

where M_y, F_x are the moment about the y axis and force along the x-axis, respectively. The drag δ is a function of Reynolds number and is classically defined as

$$\delta = \frac{1}{2}\rho v^2 C_D A \tag{3}$$

where ρ is fluid mass density, v is the magnitude of the flow velocity vector normal to the hair center axis (scalar), C_D is the coefficient of drag and is empirically determined to combine form and skin drag, and A is reference area. Thus, by measuring moment, force, or some combination of the two, the velocity of flow at hair location can be estimated.

2.5 RNNs and Real Time Recurrent Learning

Repeated (in space or time) measurements of a quantity generally provides more information regarding the quantity of interest. In general, Bayes' theorem provides a systematic approach to solving most estimation problems. In the case of linear systems with characterized Gaussian noise in process and measurement, the well-known Kalman filter provides an optimal solution,

extracting precisely the available information from all measurements. However, such optimal closed-form solutions only exist in very constrained circumstances. Furthermore, the Kalman filter is also problematic in high dimensional settings, exhibiting both numerical instability and undesirable computational burden. Nonlinear problems such as those involving flight and flow dynamics generally necessitate development of approximate estimators or learning-based approaches, especially those for which accurate models do not exist [18].

Making a difficult problem even more so, a disturbance in a flow can occur over a short period of time. The resulting dynamic prediction problem presents a difficulty for classical disturbance observation or prediction frameworks (based on dual or joint Kalman filters, etc.). Such approaches require great computational speed to accurately estimate the undesired input to the flight system all the while providing sufficient time for an actuator system to reject it. Systems such as light detection and ranging (LIDAR) attempt to overcome such issues by directly observing a disturbance ahead of the craft [19]. Control strategies can then be used to mitigate the impending disturbance. However, LIDAR systems are complex and costly. The ability to predict impending disturbances based on changing local flow features could be beneficial to smaller flight systems that cannot support systems like LIDAR.

The success of biological models is likely due to the utilization of prior knowledge in the form of predictions based on previous experience and training. Prior knowledge is important for accurate estimation and prediction in complex dynamic environments and can be obtained through machine learning techniques. Furthermore, in contrast to model based control and estimation strategies, the prediction of external disturbances could provide a solution much like that of LIDAR, except as an inferred prediction.

Considering the potential complexity of flow features, massively distributed flow sensor arrays and the naturally ill-posed problem of dynamic prediction, machine-learning techniques and specifically RNNs appear as strong candidates for a practical solution. RNNs are fully connected networks containing internal feedback and time delay, extending the concept of standard neural networks to nonlinear dynamic systems. Figure 4 illustrates a RNN consisting of an input layer, hidden inter-connected neurons, and output layer. However, unlike standard neural networks, the hidden units are fully connected. RNNs can provide universal approximation for any nonlinear function of both space and time, provided sufficient hidden neurons [18].
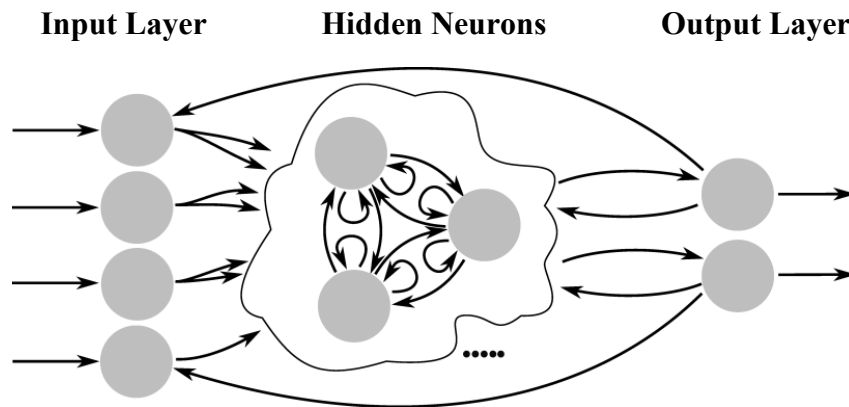
Figure 4: Example RNN Architecture

Consider a noise-free input and RNN system like the one previously illustrated. Consider a connection between any two neurons at time step n with states x_n^j and x_n^i respectively, where x_n is a vector of size $q \times 1$. The weight describing the connection for a signal propagating from neuron j to neuron I can be written W_a^{ij}. Consider any subset of neurons in a network as being input and output units, with state vectors denoted as u_n and y_n and sizes $m \times 1$ and $p \times 1$, respectively. Then, the operation of any RNN can be written in the form (directly from [18]).

$$x_{n+1} = \Phi(W_a x_n + W_b u_n) \tag{4}$$

$$y_n = W_c x_n \tag{5}$$

where W_b is a $p \times q$ input weight matrix, and $\Phi: R^q \rightarrow R^q$ is the activation function for hidden units. The network output is available by sampling whichever neurons are chosen as output nodes. The matrices W_a and W_b determine the connectivity of the neurons, which can include connectivity between inputs, outputs, hidden units, or any combination thereof. The matrix W_c specifies the output neurons and can be considered a measurement model in the sense of MIMO systems. It is generally populated sparsely by ones, which return output layer neuron values.

Here, Φ is chosen as the hyperbolic tangent for hidden units and the linear output function for all output layer neurons. Delays are implicit in the structure of Equation (4), as input signals to the system may take some time to elicit a response in distant neurons, depending on the sparsity of the matrix W. Also, the generality of the above form allows for customization of network architecture, trimming of specific connections (setting relevant entries of W to zero), etc. Equation (4) takes a general form similar to discretized equations of motion, which not only intuitively supports the aforementioned universal approximation theorem, but suggests why it is important to use a sufficient number of hidden neurons to approximate a given system.

2.6 Neural Network Training Using the Extended Kalman Filter

Many algorithms exist for training RNNs. Recently, supervised training using nonlinear sequential state estimators has emerged as one of the most successful approaches [18, 20]. Here, an extended Kalman filter (EKF) is used to train the connection weights in a prediction/correction strategy, using a training set consisting of hair sensor output and desired network response (lift and moment on an airfoil). Because inputs and desired outputs are known a priori, the network becomes a function of the weights that are fully observable to the algorithm. Thus, application of the EKF to estimation of the weights, taken here as system states, is straightforward, but does require computation of the gradient of output with respect to weights [18]. From Haykin [18], the algorithm can be summarized as follows. Given the training sample set $\{u_n, d_n\}_{n-1}^N$, where u_n is the input vector applied to the RNN and d_n is the corresponding desired response, direct application of the EKF to the dynamic system composing the RNN becomes:

$$G_n = P_{n|n-1} B_n^T \left[B_n P_{n|n-1} B_n^T + Q_{v,n} \right]^{-1} \tag{6}$$

$$\alpha_n = d_n - b_n \left(\hat{w}_{n|n-1}, v_n, u_n \right) \tag{7}$$

$$\hat{w}_{n|n+1} = \hat{w}_{n|n-1} + G_n \alpha_n \tag{8}$$

$$P_{n|n} = P_{n|n-1} - G_n B_n P_{n|n-1} \tag{9}$$

$$P_{n+1|n} = P_{n|n} + Q_{\omega,n} \tag{10}$$

where G_n denotes the Kalman gain matrix, B denotes a linearized measurement matrix, b_n is a function denoting the RNN, w is a vector composed of RNN connection weights, P is the measurement error covariance matrix, and $Q_{v,w}$ is a measurement/process noise covariance matrix. The reader interested in a detailed derivation and discussion of the above algorithm should consult Haykin [18]. In the next section, a potential flow gust simulation is briefly described that provides approximate hair sensor output alongside airfoil force and moment time history. Taken together, this information forms a set of training data for a RNN.

2.7   Quasi-Steady Potential Flow Simulation

In order to approximate a flow disturbance, such as a gust, airfoil loading due to nearby convection of vortex structures in a potential flow is simulated. The approach used here is largely based on theory in [21], is similar to the approach found in [22], and consists of a Joukowski airfoil in a flow. A pair of vortices is introduced into the flow, one contained within the airfoil and one external. The position of the internal vortex is calculated as to ensure the airfoil boundary is a streamline, effectively satisfying a non-penetrative wall boundary condition. The vortex propagates downstream according to Routh's rule [23], passing by the airfoil. Total airfoil circulation is modified at each time step such that the Kutta condition is satisfied, resulting in loading of the airfoil. A second order Runge-Kutta integration scheme is used to compute a solution to the vortex convection. During execution of this algorithm, local flow velocity along the airfoil is computed at discrete locations, chosen a priori as artificial hair sensor locations. The magnitude of these velocities is then computed, emulating response of an array of directionally insensitive artificial hair sensors. Consider a cylinder of radius a, located at point $\zeta = \zeta_0$, in an irrotational, two-dimensional flow of incompressible inviscid fluid in what will be referred to as the ζ-plane. Then, by potential flow theory, the complex potential describing the η-plane flow can be written as

$$w = U_\infty e^{i\alpha}(\zeta - \zeta_0) + U_\infty a^2 e^{-i\alpha}/(\zeta - \zeta_0) \tag{11}$$

where α is the angle of incidence of the free stream with respect to the horizontal axis. If a vortex of strength κ is located at ζ_1, and the cylinder has circulation of strength κ_0, then the potential becomes

$$w = U_\infty e^{i\alpha}(\zeta - \zeta_0) + \frac{U_\infty a^2 e^{-i\alpha}}{(\zeta - \zeta_0)} + i\kappa_0 \log(\zeta - \zeta_0 - \zeta_1) - i\kappa_1 \log(\zeta - \zeta_0 - \frac{a^2}{\zeta_1}) \tag{12}$$

with the additional terms representing the contribution of the cylinder circulation, the vortex at point ζ_1, and a matching vortex inside the cylinder ensuring the cylinder boundary is a streamline. If the external vortex is allowed to convect according to the external flow, the terms in Equation (12) must be modified according to a numerical integration routine. To compute the

flow about a Joukowski airfoil, a coordinate transformation is applied, resulting in a conformal mapping. This mapping is generally called Joukowski's transformation, and takes the form

$$z = \zeta + {L^2}/{\zeta}$$

Computation of the velocity field about the airfoil (in the z-plane) is straightforward, and immediately results from differentiation of Equation (12) with respect to z. From the resulting transformed flow, the velocity, pressure, and therefore forces and moments acting upon the airfoil can be computed. Hair sensor response is taken to be completely in phase and proportional to the magnitude of flow velocity at discrete points along the airfoil boundary. The theorem of Blasius [21] is used to calculate forces and moments on the airfoil. Figure 5 depicts a snapshot of a convecting vortex near an airfoil. The imaginary component of the flow potential is plotted as a contour surface, the contours of which describe streamlines. Note that although the vortex has severely modified the flow, the airfoil boundary is a streamline. An example result of vortex convection near an airfoil is illustrated in Figure 5 and Figure 6, in which an airfoil at zero angle of attack, Reynolds number of 3.5×10^6, is exposed to a vortex as it convects downstream. The initial position of the vortex was chosen by sampling a uniform distribution, modified to ensure that the vortex would not convect closer than five chord lengths to the airfoil. The initial distance upstream is specified as 100 chord lengths. Strength of the vortex was also generated randomly to have vorticity $-10 \text{ s}^{-1} < \kappa_1 < 10 \text{ s}^{-1}$.
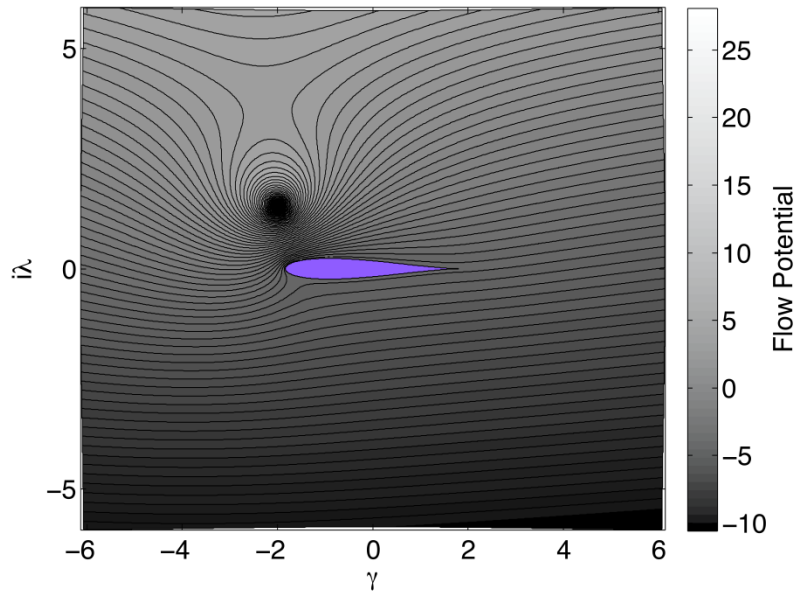
Figure 5: Snapshot of Vortex with Airfoil (Imaginary Component of Potential)

The lift and moment resulting from such a vortex gust is illustrated in Figure 5, with leading edge hair sensor responses illustrated in Figure 6 and Figure 7 as an interpolated surface. One can readily identify movement of forward stagnation point in Figure 7 as a dark region. The movement of stagnation point is related to airfoil loading, as can be inferred visually by comparing the major features of Figure 5, Figure 6, and Figure 7. Only a small time span has been plotted which contains the relevant information. Lift, moment and hair sensor output all

Approved for public release; distribution unlimited.

asymptotically approach zero as one moves away from the time of maximum airfoil-vortex interaction.
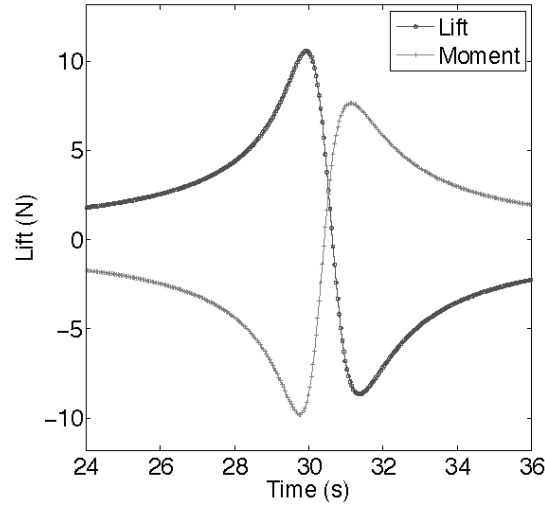
Figure 6: Lift and Moment Time History
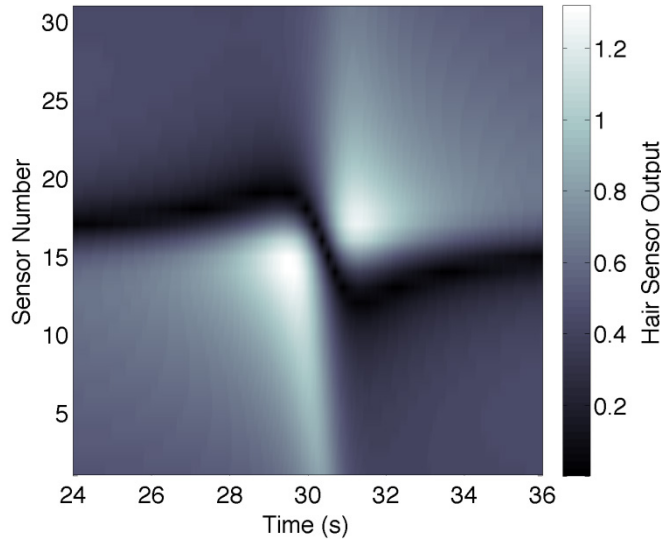
Figure 7: Hair Sensor Response vs. Time

2.8 Simulation Results

The potential flow simulation described previously was then used to produce training sets by randomly selecting vortex strength and initial position, but with airfoil angle of attack maintained at zero (to simplify preliminary study) and free-stream velocity dictated by a specified Reynolds number. As such, parameters were non-dimensionalized according to chord length, and the Reynolds number was set at 3.5106. For the present investigation, hair length is assumed to be sufficient to be dominated by flow external to any boundary layer that would actually be present. Obviously, a hair fully contained within a boundary layer can no longer be assumed to provide such a response, but the present learning-based approach is largely an effort to render such

Approved for public release; distribution unlimited.

modeling complexity irrelevant. A training set serves to manifest a physically meaningful relationship between hair sensor 12 response and aerodynamic loading. The goal here was to construct a nonlinear model (a RNN) that approximates the complex hair sensor-flow relationship with regard to external disturbances, while encouraging a predictive capability. A RNN architecture was chosen which consists of an input layer of size (n + 3), where n is the number of hair sensors, with three additional input neurons for bias and net output feedback (lift and moment estimates). For the results presented here, three hair sensors were used, extending from mid-chord on both upper and lower airfoil surfaces, equally spaced around the leading edge. The RNN, consisting of six input neurons, six hidden neurons and two output neurons, was trained on the aforementioned gust simulation data. Preliminary results indicate success as far as training a RNN to accurately describe airfoil loading as a function of hair sensor feedback. Figure 8, Figure 9, and Figure 10 depict training results from a single gust simulation. Using the hair output of Figure 8, a RNN can be trained by repeatedly looping through the time history of the training set. Here, repeated loops are referred to as epochs. The total error in time (Euclidean norm) is illustrated for each epoch in Figure 9. Within 80 epochs, the system converged to a degree resulting in imperceptible difference between RNN and desired response. While such a training methodology would likely yield poor generalization to other gusts, it demonstrates the effectiveness of the training algorithm chosen.
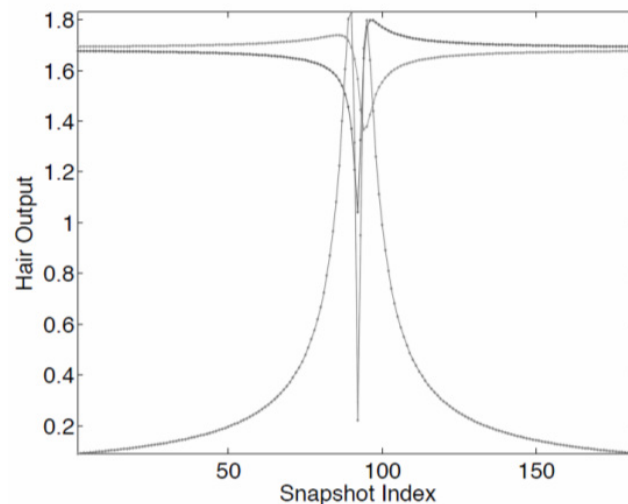
Figure 8: Hair Output Time History
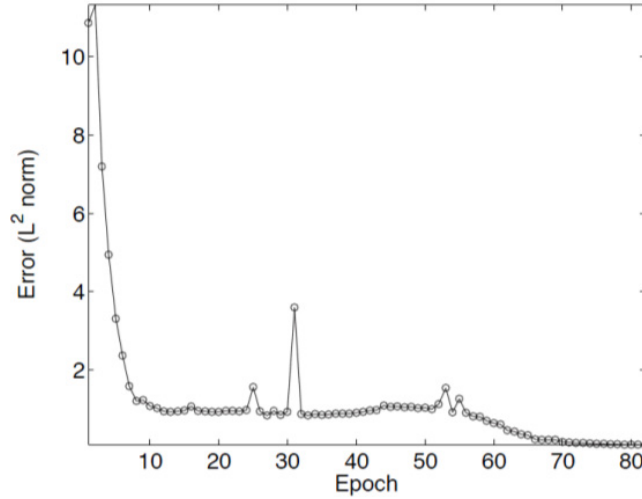
Figure 9: Training Error vs. Epoch

The desired output of the RNN as a function of hair sensor input agrees well with the desired lift and moment functions, as can be seen in Figure 10. The real question is whether or not such a network can predict the lift and moment for a general vortex. Such questions will be addressed in the final manuscript.
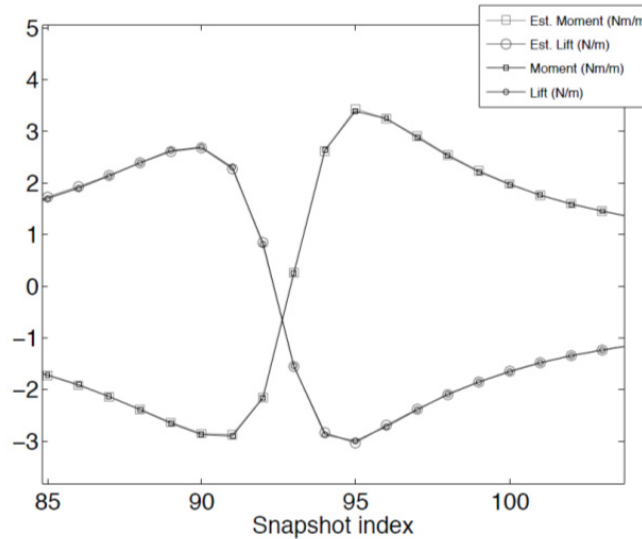
Figure 10: Desired Output vs. Network Output After Training

We anticipate results that will describe a network architecture that uses distributed hair sensor signals to predict the forces and moments resulting from a gust. Such an architecture will utilize a two-component neural network system, the first consisting of hair sensor fusion layers which are not recurrent, but provide an internal output to a RNN that is dedicated to prediction. Such an architecture serves as a foundation for investigating distributed sensor compression and associative memory design for discovering critical flow features, such as stagnation point, and for modeling in an effective and practical manner the complex physics of the problem. The proposed architecture may also lend itself to incorporating other sensory modalities such as

pressure and/or structural. As the potential flow model used in this work was fairly crude, a high-fidelity Navier-Stokes simulation will be used to generate equivalent, but much more realistic hair sensor and airfoil loading data for future investigation. Such a simulation includes unsteady, complex flow phenomena such as turbulence and separation. Indeed, it is these phenomena that are of the utmost interest for this work, and the results that come from such a study will be extremely interesting.

2.9   Experimental System Demonstration

To demonstrate the functionality of the hair sensors and the application of the above neural network control algorithms, the flow characteristics around a cylinder in cross-flow was experimentally measured using a hair sensor. A single hair sensor was mounted to a cylinder and the resistance across the top and bottom electrode measured at various angles as the cylinder was rotated in the flow. Sensor output at each angle measured is shown in Figure 11. Relatively stable signal was achieved at each angle as shown by the limited amount of variation along the Time axis and the standard deviation for each angle shown in Figure 12.
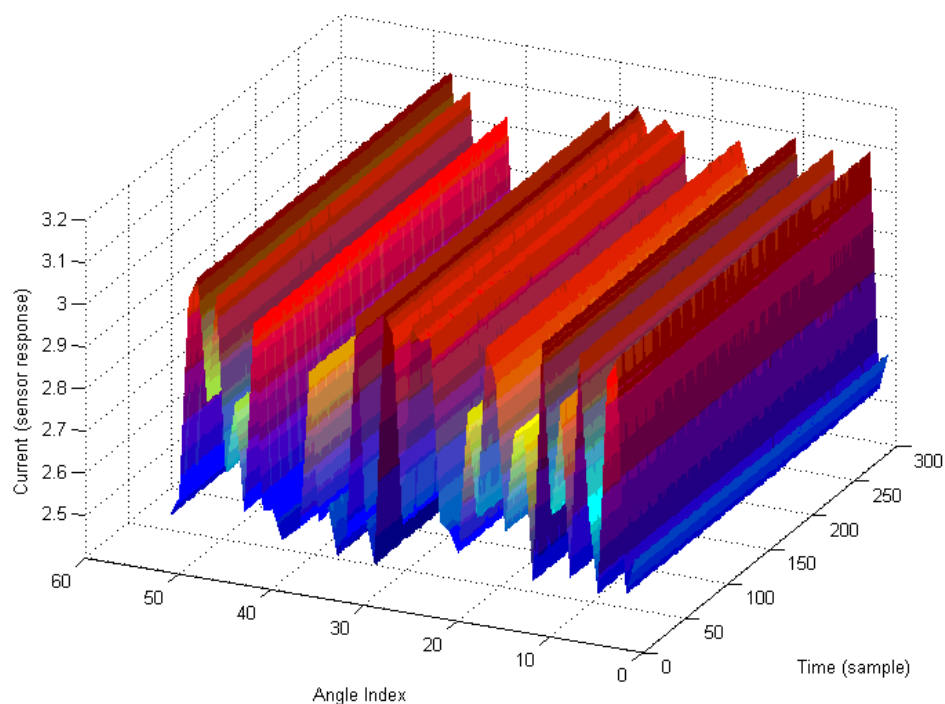
Figure 11: Sensor Response Surface
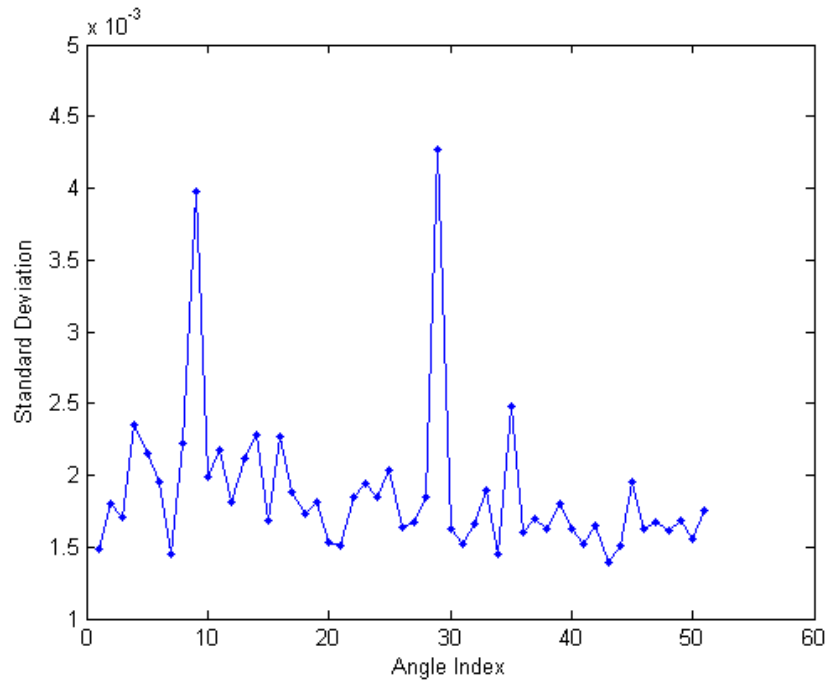
Figure 12: Sensor Standard Deviation

Relative flow velocity around the cylinder using PIV is shown in Figure 13. Interior to the cylinder is the output from the hair sensor. Flow velocity, the stagnation point, and separation point are accurately measured.
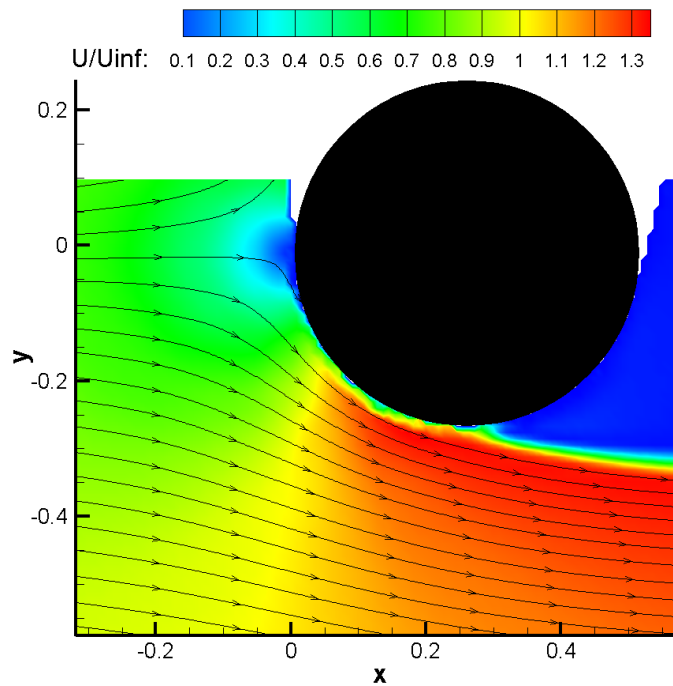
Figure 13: Experimental PIV Wind Tunnel Data

2.10 Artificial Hair Sensor Conclusion

While preliminary, the main conclusion that can be garnered from this work is that RNNs and EKF-based training are very effective for learning overall system behavior. A challenge, however, lies in generating a successful network architecture to achieve a desired end. Indeed, this is one of the main problems with using neural networks in practical application. However, as was demonstrated, even a simple approach can nonetheless yield valuable results for a problem that might otherwise be intractable. The nonlinear modeling capabilities of RNNs are extraordinary and have begun to evoke excitement in the robotics and machine learning community due to their learning and memory potential. However, their application to flight estimation and control applications is largely uninvestigated. With the potential to offer both predictive and accurate nonlinear system approximation capabilities, RNNs may yield performance and robustness enhancements that were previously unobtainable. Future work will address the concepts and ideas mentioned throughout this document with the end goal of testing such strategies in wind tunnel experimentation. How one might utilize the present RNN approach in current aircraft control systems will also be addressed. The success of the current control paradigm is unquestionable, but methods of incorporating flow features into such a framework have been, to date, entirely ad hoc. As such, RNNs may offer a consistent empirical approach to dealing with massive amounts of complex, dynamic sensory data to improve aircraft performance.

3 RECONFIGURABLE SKIN SYSTEM DESIGN

3.1 Introduction

Reconfigurable structures have been the topic of much research in recent years including candidate materials and systems used to cover them, aka skins. It has also been proposed that one such skin could be made of a cellular structure filled with a variable stiffness material, such as honeycomb filled with shape memory polymer (SMP). [24, 25, 26, 27]

3.2 Concept Description and Motivation

The aerodynamic performance of aircraft for specific mission profile segments can be improved through changes in wing shape [28]. Andersen showed that in a variety of mission segments such as dash, cruise, climb, and loiter a different wing configuration optimized aerodynamic performance. The current goal is to create a monolithic skin that does not wrinkle when deformed and is able to strain more than traditional materials while supporting aerodynamic loads.

Cellular structures can be designed with relatively low in-plane and high out-of-plane stiffness. Low stiffness is obtained by the empty space within each cell, providing space for the nearby thin structures to deform. Deformation of these thin beam structures can be inhibited by filling the empty space or by adhering face sheets. Thus the stiffness of the cellular composite can be controlled by judicious choice of materials. If a phase change or variable stiffness material such as shape memory polymer is used, the effective stiffness of the skin is controllable both in magnitude and direction. By manipulating the stiffness of individual cells, for example by thermal means such as shown in Figure 14, in specific patterns the global material properties of the skin can be tailored to the specific in-flight needs of the aircraft. A few potential patterns are shown in Figure 15. One of the goals of the presented research is an experimental investigation into the possible range of effective skin properties, representing bounded limits of the system. As a representative system, epoxy shape memory polymer and aluminum honeycomb were used to demonstrate the system and validate the developed models.
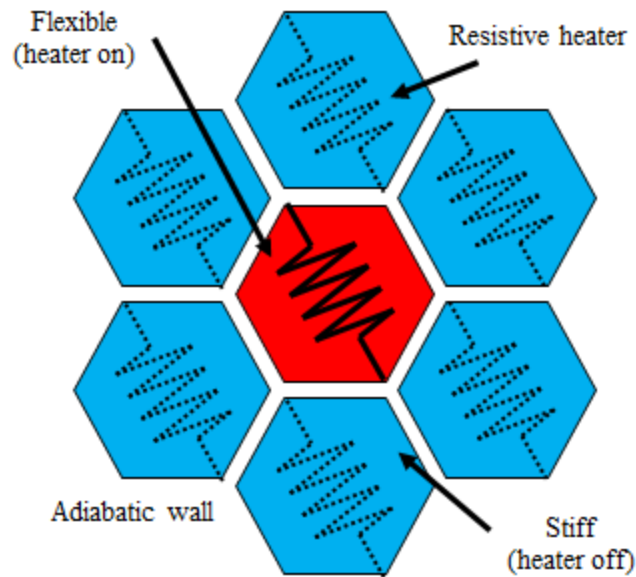
Figure 14: Filled Honeycomb Concept
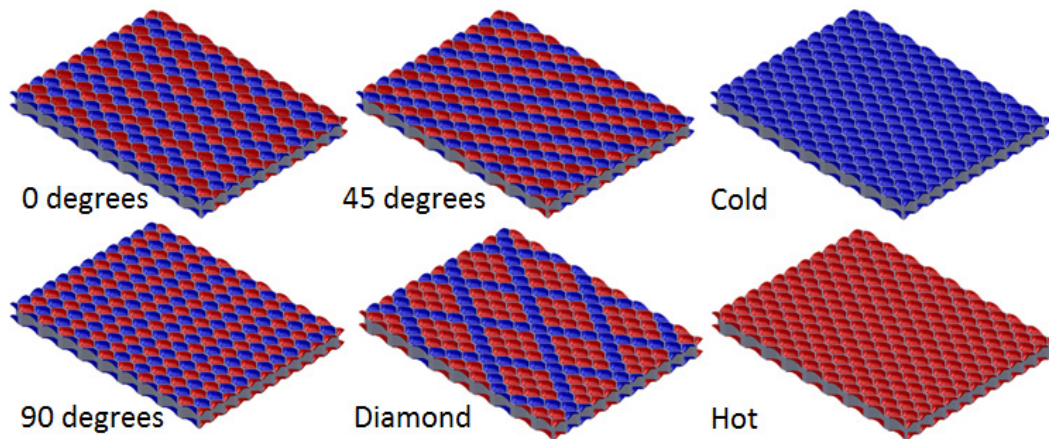
Figure 15: Conceptual Heating Patterns

Thus the properties of the proposed filled honeycomb reconfigurable skin require experimental validation, modelling, and optimization. This was accomplished by experimentally characterizing the epoxy SMP, aluminum honeycomb, and SMP/honeycomb composite at ambient and above T_g temperatures in both in-plane cardinal directions. This data along with FEA was then used to validate an analytical model. Finally, using the experimentally validated analytical model, topology optimization on the composite skin was performed to find the ideal honeycomb geometry given a prescribed set of boundary conditions.

One of the major remaining barriers to the widespread adoption of thermally activated shape memory polymer is the method used to heat them. Presented is an investigation into using 5 μm

nickel particles aligned into chains as embedded Joule heaters for epoxy SMP. The high density of particle chain heaters reduces the time and energy required to reach transition by minimizing excess heat required due to the low thermal conductivity of the polymer by heating the material more uniformly. The chains are formed by curing the polymer in a uniform magnetic field generated by two sets of N42SH Neodymium magnets above and below the sample. Modeling of the induced magnetic field within and between particles during curing and an analytical model predicting particle mobility in a fluid with respect to vibration frequency and amplitude are presented and discussed in context to the current work. Since epoxy resin has a high viscosity, particle mobility is encouraged by sonicating the sample at 300 Hz at an amplitude of approximately 50 μm prior to polymerization using an industrial shaker and Teflon guides. Copper mesh electrodes are attached to the resulting samples using 10 percent by volume nickel particle SMP epoxy. Significant particle alignment is confirmed via optical microscope images. Electrical resistivity is measured as low as 57 Ω-mm at Nickel volume concentrations of 1.0 percent. Infrared images of the samples during heating are presented and electrical energy required with respect to sample thermal capacity estimated.

The Morphing Aircraft Structures (MAS) phase II program is used to demonstrate the capabilities of the system and as a realistic design optimization criteria. Program requirements are listed in Table 1 and include aerodynamic load specifications, desired skin dimensions, weight limits, and skin functionality requirements.

Table 1: MAS Program Skin Requirements

MAS Requirements	English	SI
Total Skin Weight	< 0.95 lb/sq-ft	< 4638.31 g/m2
Out-of-plane Air Loads	400 lb/sq-ft	19,152.1 Pa
Nominal Panel Size	15" by 20"	0.381 by 0.508 m
Max Out-of-plane Deflection	0.1"	2.54 mm
Shear Capability	30 – 75 degrees	~ p/4 – 2p/3 radians
No wrinkling of skin in any position		
Enforced displacement in-plane		
Aerodynamic loads out-of-plane		

3.3 Embedded Heating Elements

Reconfigurable skins have been proposed for a multitude of applications including morphing aircraft, deployable satellites, and shape changing cars. One of the main correlations between these applications is the need for a skin material with controllable, adaptable material properties that offer both structural load bearing capabilities as well as low stiffness configurations during reconfiguration. For this purpose, SMP filled honeycomb cores have been proposed. [29, 30, 31, 25, 32]

One of the main barriers to implementation of such a skin system is the method used to heat the SMP. Methods of making SMPs conductive and thus electrically activated through joule heating have been extensively studied. Systems including carbon fibers, carbon nanotubes, carbon black, exfoliated graphite, metallic nanostrands, metallic powders, small wires, and oxide powders have all been proposed. [33, 34, 35, 36, 37] Luo and Mather were able to achieve sub-2-second

activation using continuous carbon nanofibers in an epoxy SMP matrix. The glass transition temperature, T_g, for the sample, 50 °C, was lower than many applications require however and the sample was very thin, whereas transitioning a thick sample is more complicated. Nickel coated graphite fibers [33, 34] and stainless steel fibers [34] have been used to create conductive polypropylene composites with some success however require sophisticated manufacturing techniques. Nickel powders have been used similarly to the presented study by Leng et al., providing joule heating by aligning the particles into chains using lower viscosity resins and a weaker polymer. [35, 36] Similar to the presented work, they aligned metallic particles using magnets in a thin strip of uncured polymer resin. The resulting nickel chains greatly reduced the electrical resistance of the sample and were shown to retain their integrity after several strain cycles.

3.3.1 Particle Chain Spacing

The SMP used in the current study is an epoxy SMP comprising of EPON826 and JeffamineD230. This polymer was chosen for its known characteristics and tailorable properties. Compositions, cure cycle, and manufacturing procedures are published by Xie et al. [38] The resistive heating elements embedded in the SMP are constructed of Nickel particles, chosen for their resistive heating, magnetic, and corrosion properties. The particles are approximately 5 μm in diameter spheres supplied by Sigma-Aldrich. Material properties for both the SMP and Nickel particles are shown in Table 2 and Table 3.

Table 2: Nickel Particle Properties

Material Property	Value
Density (g/m^3)	8.908e6
Young's Modulus (Pa)	207e9
Electrical Resistivity (Ω-cm)	6.4e-6
Magnetic Permeability	1240
Particle Diameter (m)	5e-6
Thermal Capacity (J/m^3/C)	0.46
Thermal Conductivity (W/m/K)	60.7

Table 3: Shape Memory Polymer Properties

Material Property	< Tg	> Tg
Young's Modulus (Pa)	1.3e9	1.9e7
Thermal Cond. (W/m/K)	0.206	0.234
Thermal Capacity (J/m^3/K)	1.43e6	2.45e6
Density (g/m^3)	1.153e6	
T_g (C)	78	
Viscosity 25C (Pa-s)	8	
Viscosity 75C (Pa-s)	0.08	
Thermal Expansion Coefficient (m/m/K)	55e-6	

Some of the advantages of the chosen heating scheme are its inherent flexibility in material selection, ease of manufacturability, and tailorable properties. Unfortunately since the polymer

has a relatively low thermal diffusivity, either extremely long times are required to heat the polymer to transition or the material nearest the heat source will be significantly above T_g; both of which are undesirable. One of the principal advantages of distributed heat sources such as the presented Nickel particle chains is the excess thermal energy required to heat the polymer quickly is minimized by minimizing the distance between heat sources.

Using a simple 1D thermal model described by Equations (13) through (24), the minimum volume density of particles needed to heat the SMP to T_g in a given time can be calculated. Particle chains are modeled as cylinders with effective radii based on surface area, r in Figure 16. If the chains are efficiently packed in the material and spaced *2b* apart, then each chain is approximately responsible for heating a cylindrical area of radius *b'* from the center of the chain. The SMP is then modeled as a hollow cylinder with inner radius r and outer radius *b'*. The outer radius is assumed to be adiabatic due to symmetry while a uniform heat flux, q_{in}, is applied to the inner radius. The cylinder is assumed to be at uniform initial temperature and thermal properties of the polymer are allowed to vary with temperature; which has been shown to have a significant impact on the calculated thermal energy and time required to reach transition. [39] With an initial temperature of 25 °C and the temperature at the interface between the chain and polymer limited to 200 °C to prevent damage to the polymer, the time required for the temperature *b'* from the center of the chain to reach T_g is calculated. Supplied power is distributed over a cube of SMP 1 cm by 1 cm in area and 5 mm thick.
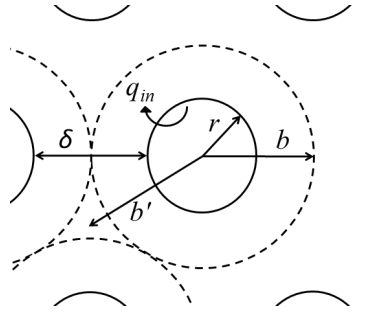
Figure 16: Parameters for 1D Thermal Diffusion Between Chains

$$T(r,t) = w(r,t) + s(r) + T_m(t) \tag{13}$$

$$T_m(t) = \overline{f} + \frac{2q_{in}at}{C_p(\delta^2 - a^2)} \tag{14}$$

$$s(r) = \frac{q_{in}a}{k(\delta^2 - a^2)}\left(\frac{r^2}{2} - \delta^2 \ln(r)\right) + C \tag{15}$$

$$C = -\frac{q_{in}a}{6k}\frac{(\delta^3 - a^3)}{(\delta^2 - a^2)(\delta - a)} +$$
$$\frac{q_{in}a\delta^2}{k(\delta^2 - a^2)(\delta - a)}[\delta(\ln(\delta) - 1) - a(\ln(a) - 1)] \tag{16}$$

$$w(r,t) = \sum_{n=1}^{\infty} A_n \phi_n(r) e^{-\lambda_n \alpha t} \tag{17}$$

$$A_n = \frac{\int_a^b F(r)\phi_n(r)r\partial r}{\int_a^b \phi_n^2(r)r\partial r} \tag{18}$$

$$F(r) = f(r) - s(r) - \overline{f} \tag{19}$$

$$\left.\frac{\partial T}{\partial r}\right|_{r=a} = \frac{-q_{in}}{k} \tag{20}$$

$$\left.\frac{\partial T}{\partial r}\right|_{r=\delta} = 0 \tag{21}$$

$$T(r, t=0) = f(r) \tag{22}$$

$$\delta = \frac{2b\sqrt{3}}{3} \tag{23}$$

$$h = b\sqrt{3} \tag{24}$$

Figure 17 shows the time required for the temperature b' from the particle chain to reach 78 °C with respect to the volume fraction of Nickel particles. An order of magnitude increase in the volume fraction of Nickel particles results in only a 12% reduction in heating time. Interestingly, the low thermal conductivity of the polymer and limiting the temperature at the interface to prevent damage results in the peak supplied power having little effect on the excess energy required to reach transition, thus only one curve is visible in Figure 18. Excess energy being defined as the amount of thermal energy delivered to the polymer beyond what would be required if the polymer were uniformly at T_g. In each case the temperature of the polymer near the particle chain reaches 200 °C before the temperature at b' reaches T_g. This results in the amount of excess thermal energy required having a similar trend to that of the time required for transition with approximately 13% less energy being required using 10 vol% Nickel than 1 vol% while the peak supplied power has little to no effect.
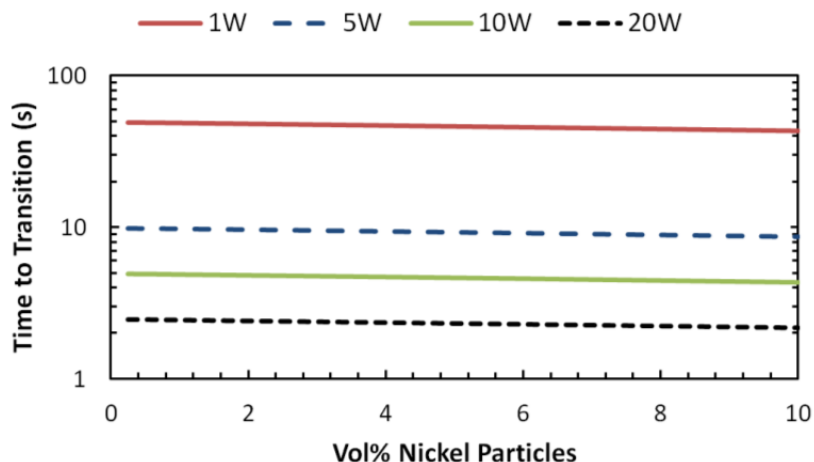
Figure 17: Minimum Time to Reach T$_g$ Given Volume Fraction of Particles and Heating Power
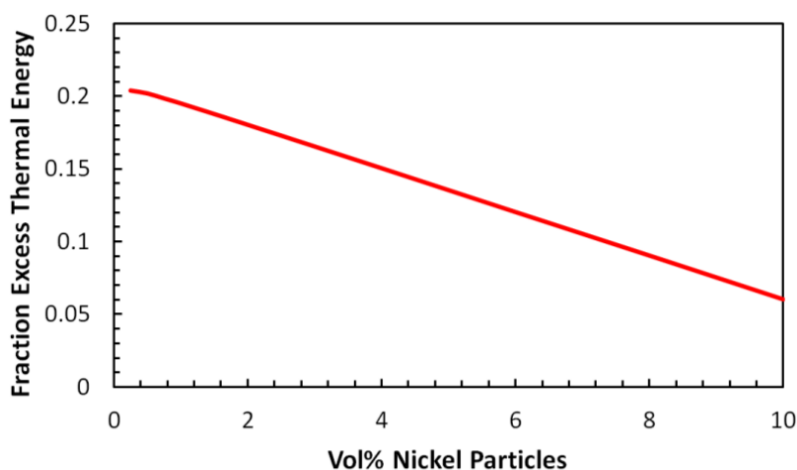
Figure 18: Excess Energy Required to Reach T$_g$ Given Volume Fraction of Nickel Particles

A system with perfectly dispersed chains is of course unrealistic. The chains formed in a real system are not evenly spaced, have non-connecting branches and sections, and may be more than one particle in thickness. Thus, the above predictions represent the minimum power and particle fraction required for a desired heating time.

3.3.2   Nickel Particle Chain Formation and Characterization

3.3.2.1   *Particle Alignment Due to Magnetic Fields*
To align the particles into chains, randomly dispersed particles in uncured SMP resin are subjected to a magnetic field. Neodymium N42SH magnets, serviceable up to 150 °C, encased in aluminum fixtures are suspended above and below the sample as shown in Figure 19 and Figure 24. The magnets are 60 mm apart with the sample placed in the center. Each magnet is 101.6 mm wide and 3.175 mm thick. The sample shown in Figure 19 is 127 mm in length and 5mm thick. The polymer resin sample is in an open Teflon® mold which sits in two "C" shaped Teflon® guide blocks. The magnetic field surrounding the sample is modeled using the freeware

Approved for public release; distribution unlimited.

program Finite Element Method Magnetics (FEMM) version 4.2. The magnetic field within the sample has an average strength of 4.77e4 A/m, with a standard deviation of 1.9e4 A/m (40%). While there is significant variation in magnetic field strength horizontally, particularly near the edges, vertically the field is nearly uniform with a standard deviation of 1.82e3 A/m (3.8%). Placing the magnets closer together increases the vertical standard deviation of field strength making the field less uniform. A non-uniform field causes a net non-zero magnetic force between the particles in the sample and the magnets which causes the particles to collect on the top and bottom surfaces rather than form chains.

Also shown is the induced magnetic field between three vertically aligned Ni particles. The magnetic polarization created in the particles dramatically increases the field density between nearby particles. The three particles shown in Figure 19 are 5 μm and 15 μm apart. The magnetic polarization created in the particles by the magnets causes the particles to be attracted to one another when aligned vertically; forming chains along the magnetic field lines between the two magnets. The entire assembly is placed in an oven at 100 °C for 3 hours to cure, ensuring good particle alignment during the expansion and shrinking that occurs during curing.

	1.046e+005 : >1.100e+005
	9.920e+004 : 1.046e+005
	9.380e+004 : 9.920e+004
	8.840e+004 : 9.380e+004
	8.300e+004 : 8.840e+004
	7.760e+004 : 8.300e+004
	7.220e+004 : 7.760e+004
	6.680e+004 : 7.220e+004
	6.140e+004 : 6.680e+004
	5.600e+004 : 6.140e+004
	5.060e+004 : 5.600e+004
	4.520e+004 : 5.060e+004
	3.980e+004 : 4.520e+004
	3.440e+004 : 3.980e+004
	2.900e+004 : 3.440e+004
	2.360e+004 : 2.900e+004
	1.820e+004 : 2.360e+004
	1.280e+004 : 1.820e+004
	7.400e+003 : 1.280e+004
	<2.000e+003 : 7.400e+003

Density Plot: |H|, A/m

Figure 19: Magnetic Field Intensity Surrounding the Sample (Top) and Between Particles (Bottom)
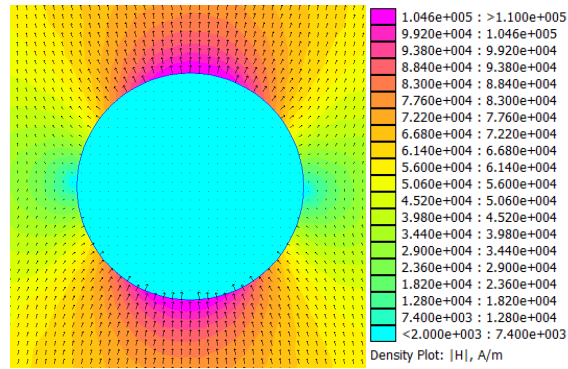
Figure 20: Magnetic Field Intensity and Direction Near a Nickel Particle

Using FEMM, the attractive or repulsive force between a pair of particles can be calculated. Particles aligned vertically attract while particles in the same plane aligned horizontally repel. The magnetically induced attractive force between two vertically aligned spherical Nickel particles is shown in Figure 21 as a function of the distance between the particles. A similar negative curve can be generated for the repulsive force between particles in plane.
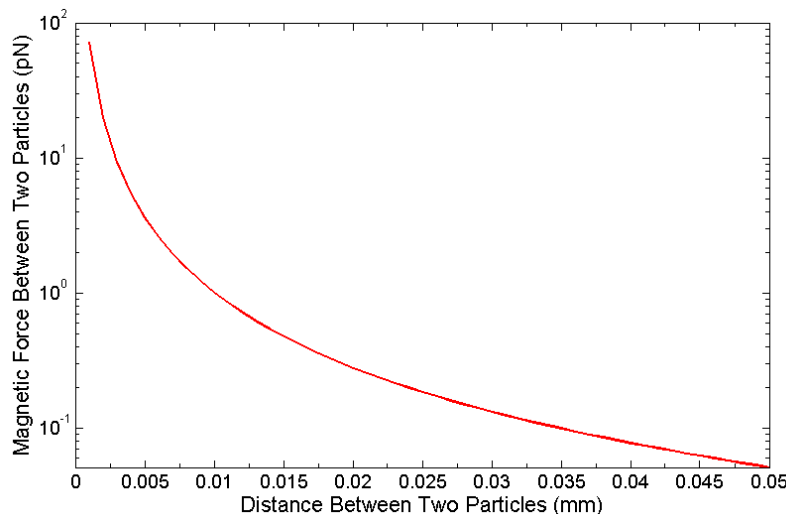
Figure 21: Magnetic Attractive Force Between Vertically Aligned Particles

The net downward force on a particle taking into account gravity and buoyancy is 4.97 pN. Thus, for any positive vertical movement the magnetic force between two vertically aligned particles must be higher than 4.97 pN. With the above magnetic setup this occurs only for particles less than 4.2 μm apart. At 1 vol%, if the particles are efficiently dispersed there is an average 19 μm between each particle. At 19 μm, the magnetic force between two vertically aligned particles is 0.31 pN, far less than is required. While the magnetic field is sufficient to vertically align particles in close proximity, it is insufficient to properly attract particles more than a diameter apart.

It is possible to increase the strength of the magnetic field and thus the induced magnetic field within each particle resulting in stronger magnetic forces between particles. The distance between the magnets pictured in Figure 19 can be decreased or the strength of the magnets can

be increased. Either of these methods however would increase the magnetic field gradient experienced by the sample. A strong gradient results in a net non-zero magnetic force between the particles and magnets attracting the particles to either the top or bottom surface of the sample. While not directly studied, increased particle densities near the surface of the sample and significant surface texturing were seen for magnet spacings less than 40 mm apart.

3.3.2.2 *Particle Alignment Due to Linear Vibrations*

To supplement the force on the particles generated by the magnetic field, linear polarized vibration is introduced to the sample to increase particle mobility. Particle motion in a vibrating fluid has been extensively studied and modelled. [40] Figure 22 shows the direction of forces generated on a particle for any pair of particles aligned along one of the three cardinal axes when subjected to a polarized vibrating fluid.
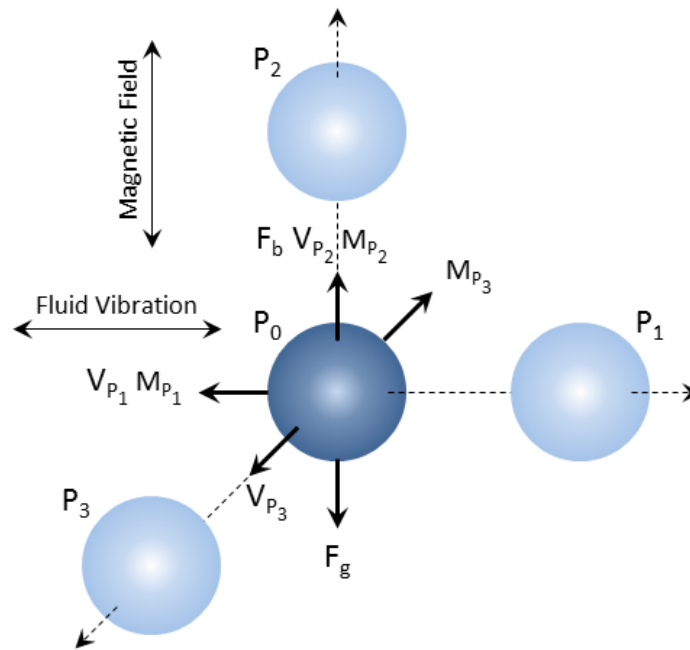
Figure 22: Gravity, Buoyancy, Vibration, and Magnetic Forces on a Suspended Particle

In Figure 22 F_b is the buoyancy force, F_g is the force due to gravity, and V and M are forces induced by vibration and the magnetic field respectively with respect to the nearby particle noted in the subscript. Tangential vibratory forces such as that created between particles P_0 and P_1 cause neighboring particles to repel while normal vibrations such as that between P_0 and P_2 cause particles to attract. If the central particle P_0 were surrounded by particles on the negative axes as well as the particles shown in Figure 22 (six particles total) and each were the same size, shape, and distance from particle P_0, the resulting forces due to the vibrating fluid and magnetic field would cancel and the net force on the particle would simply be the difference between the force due to gravity and the buoyancy force. A perfectly uniform distribution of particles would then result in the particles simply settling. Non-uniform particle shape and size and varying distances between particles is believed to result in a net non-zero force on each particle causing them to preferentially align along magnetic field lines. Since all forces in-plane cause particles

to repel, the vibration frequency and amplitude and strength of the magnetic field can be optimized such that the distribution of chains is relatively uniform.

Lyubimov et al. derived the below equations for the force experienced by a pair of particles in a vibrating fluid dependent upon their orientation with respect to the vibration.

$$\nabla \bar{v}^2 = 3a^2 \omega^2 r^3 \frac{\rho_p - \rho_f}{\rho_f + 2\rho_p} \left(\frac{5\cos^2\theta - 1}{\delta^4} \vec{\tau} - 2 \frac{\cos\theta}{\delta^4} \vec{j} \right) \tag{25}$$

$$\vec{F} = \frac{3}{4} V_p \rho_f \frac{\rho_p - \rho_f}{\rho_p + \frac{1}{2}\rho_f} \nabla \bar{v}^2 \tag{26}$$

Where a and ω are the vibration amplitude and frequency, r is the particle radius, ρ_p is the particle density, ρ_f is the fluid density, V_p is the particle volume, δ is the distance between the two particles, $\vec{\tau}$ is a unit normal vector connecting the two particles, $\nabla \bar{v}^2$ is the gradient of the mean squared pulsational velocity averaged over the vibration period, $\vec{j} \bullet \vec{\tau} = \cos\theta$, and $\vec{F}$ is the force experienced by each particle. Particles normal to the flow ($\theta = \pi/2$) experience an attractive force while particles aligned parallel to the flow ($\theta = 0$) repel.

As predicted by Equations (25) and (26), particles normal to the flow experience a positive force causing them to attract while the magnetic forces and forces due to parallel flow cause particles to repel. This interplay between attractive and repulsive forces in plane causes banding to occur in the sample where parallel rows of particles accumulate perpendicular to the direction of vibration. This alignment of particle chains has been seen experimentally by Lyubimov for 2-degree-of-freedom systems in which a single layer of particles are subjected to vibrations in a fluid. The effect is also observable in samples from the presented work many particles thick as shown in Figure 23.
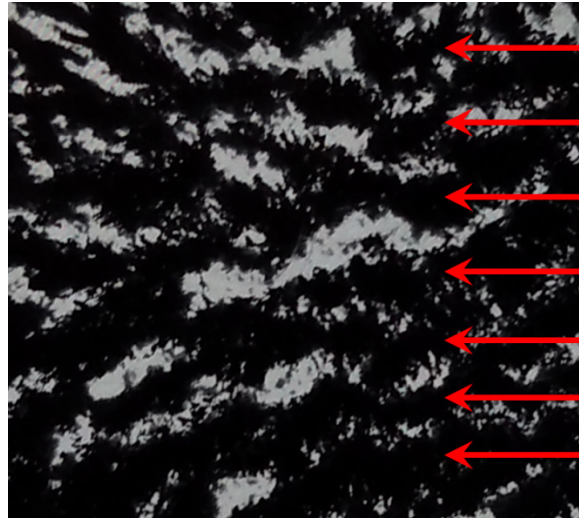
Figure 23: Backlit 10-mm Thick Sample

In Figure 23, particles are dark with a light background. Distinct banding spaced approximately 1 mm apart is highlighted with red arrows. The sample was subjected to both the magnetic field pictured in Figure 19 and 50 μm linear vibrations at 300 Hz. Slight particle alignment perpendicular to the direction of vibration in a 1-mm-thick sample subjected only to vibration (no magnetic field was applied) was also observed. While this and Figure 23 indicate that Equations (25) and (26) are applicable to the presented case, they are as of yet unverified for vibrational amplitudes larger than the diameter of the particles being modelled and thus are provided here as a qualitative reference. It should also be noted that the 50 μm 300 Hz vibration is applied to the mold. No attempt to measure the motion of the fluid was performed. It is also believed that fluid motion near the bottom, sides, and open top surface varies greatly. Imperfect particle shape and size differences are also factors in the resulting particle dynamics. The complexity of factors influencing particle motion is such that modeling the system dynamics directly is beyond the scope of the presented work. Thus, the presented theories are predominantly qualitative.

3.3.3   Sample Fabrication

The experimental setup used to achieve particle alignment is shown in Figure 24. The 300 Hz shaker motor signal is generated by a function generator. The fulcrum connecting the shaker and the mold reduces the stroke of the shaker 10:1 resulting in the sample experiencing an amplitude of approximately 50 μm. After curing, samples are lightly sanded and copper mesh electrodes are applied to the top and bottom surfaces using the same epoxy SMP with 10 vol% nickel particles. The electrodes are clamped between two thin sheets of Teflon and aluminum plates during curing ensuring good contact.
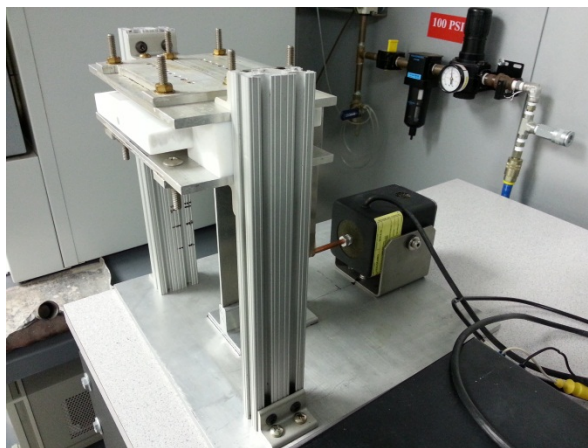
Figure 24: Experimental Magnetic and Vibration Setup

3.3.4   Experimental Results

3.3.4.1   Particle Alignment

Using the above method, nickel particle chains can be readily formed in epoxy resin during curing. The magnetic and vibratory forces are sufficient to generate particle motion such that no delay is required between mixing and curing the sample. The particles align in the oven during the first few minutes of the cure cycle before any significant polymerization. Figure 25 shows

Approved for public release; distribution unlimited.

the alignment achieved in a typical sample with 1 vol% Nickel particles. While there are several chains that terminate in the middle of the sample and the chains vary in thickness, there is generally good alignment and distribution.
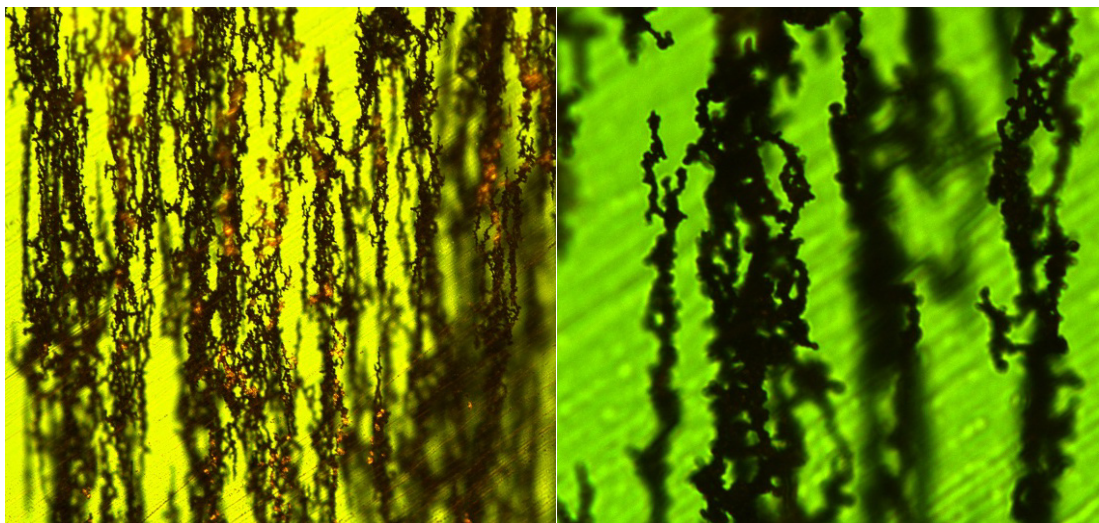
Figure 25: 10X (Left) and 50X (Right) View of 1 Vol% Nickel Particle Chains

3.3.4.2 *Electrical Properties*

As a measure of the quality of particle alignment and the heating capability of the nickel chains, the resistance of samples at various temperatures was measured and the resistivity of the material calculated. Figure 26 shows the results for a 1 vol% Nickel particle/epoxy SMP composite. At ambient temperature the average resistivity is 57 Ω-mm with very little variation between samples. As the temperature increases the resistivity of the samples increases until unreadably high resistance values are attained above 160 °C.
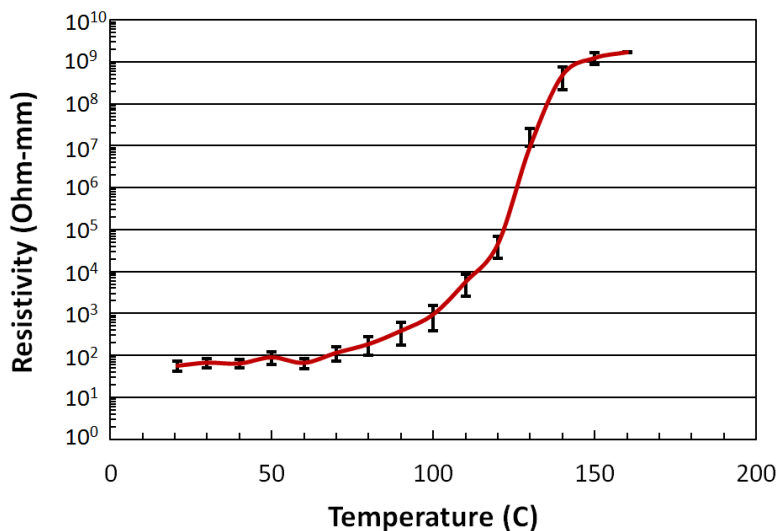
Figure 26: Average Resistivity and Standard Deviation of 12 Samples Allowed to Thermally Expand

The more than seven order of magnitude increase in resistivity can possibly be attributed to several factors, the dominant being thermal expansion. Between ambient and 160 °C the samples expand by approximately 0.8%. It is postulated that this is sufficient for the majority of particles to be pulled away from one another, ceasing to physically touch, resulting in an open circuit. Indeed, if a sample is placed in a vise in an over at 120 °C and gradually subjected to compressive strains the resistivity of the samples reduce to ambient temperature levels as shown in Figure 27.
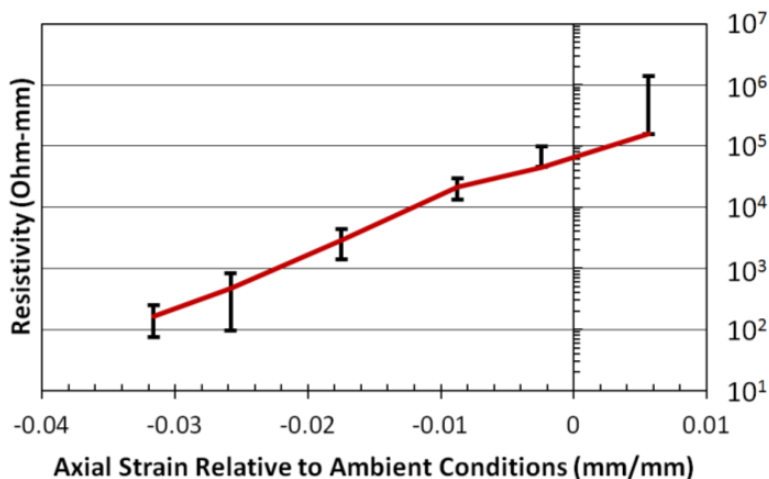
Figure 27: Average Resistivity of Samples at 120 °C Subjected to Compressive Strain

Measured resistivity of samples of varying nickel contents are shown in Figure 28. Samples with 0.75 vol% nickel and below have significantly higher resistivity at room temperature than those with 1 vol% or higher. While nickel content is believed to have a significant effect on sample resistivity, the cause of the difference in initial resistivity above and below 1 vol% is unclear. All volume fractions however increase in resistivity with increasing temperature, previously shown to be the result of thermal expansion.
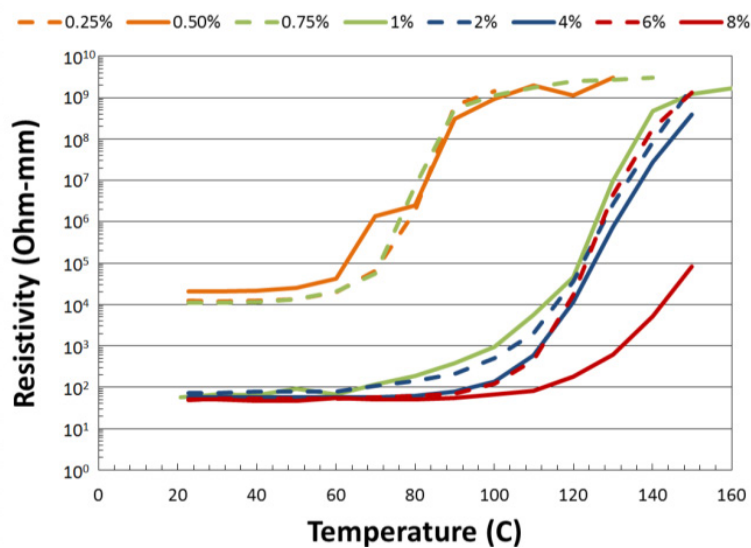
Figure 28: Resistivity Dependence on Temperature and Vol% Nickel Particles

3.3.4.3 Thermal Distribution

Regardless of the cause, the increase in resistivity results in two advantages. Due to the variation in the quality and distribution of the Nickel particle chains the samples are not perfectly uniform in their electrical properties. There exist pathways that are more conductive than others through the sample, causing current to preferentially flow through certain chains and not others. If unaltered, this would cause the samples to heat up non-uniformly drastically increasing the time and energy required to reach transition. Since the resistance of the sample increases with temperature (due to local thermal expansion), areas of high temperature have higher resistance than those of lower temperature. As current flows through a certain chain or set of chains, the temperature increases. As the resistance increases with increasing temperature; the path of least resistance shifts to another area. As current begins to flow through this new area; the temperature increases and the cycle continues. This results in the sample heating more evenly and quickly and can clearly be seen in the series of infra-red images in Figure 29. The top image shows the sample just after current has been applied where the left most particle chain is slightly warmer than the surrounding sample. After 0.55s, the temperature of the chain is high enough that the path of least resistance has moved to the right, Figure 29 middle. After 0.935s the SMP near the particle chains on the left side of the sample has reached Tg and the sample in this area has become non-conductive. Figure 30 shows a magnified section of the sample shown in Figure 29 at 0.935s overlaid with an optical image of the sample. Areas of increased temperature clearly align with areas with high densities of particle chains.

Approved for public release; distribution unlimited.
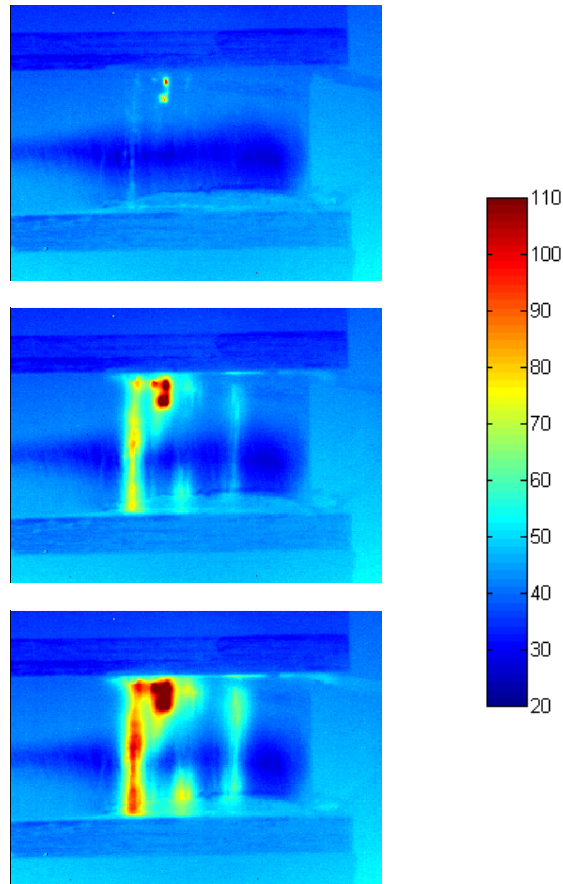
Figure 29: Infrared Images of 30V, 0.01A Applied to 8mm Tall by 2mm Thick Sample. 0.055s (Top), 0.55s (Middle), and 0.935s (Bottom) (Temperature scale in °C)
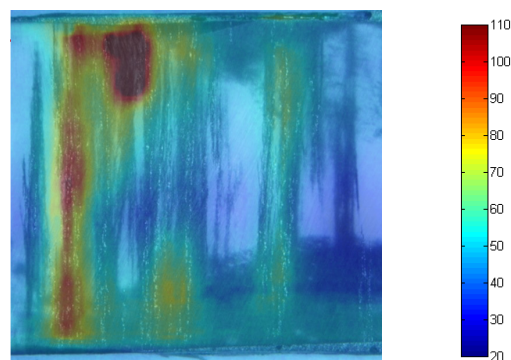
Figure 30: Infrared (Top), Optical (Bottom), and Overlay (Middle) Images of Nickel Chain Heating (Temperature scale in °C)

The second advantage of the composite increasing in resistivity with increased temperature is the ability to use the resistance of the sample as a temperature sensor. Rather than requiring a separate thermocouple to determine when the desired temperature has been reached, the resistance of the sample can be used to estimate temperature.

3.3.5   Nickel Chain Heating Elements Conclusions

A method for aligning magnetic particles in fluids with high viscosities has been demonstrated leading to an effective technique for quickly and uniformly heating shape memory polymer. It has been shown that sub-two second activation times are achievable with very low volume fractions (<1.0%) of conductive particles minimizing the added weight associated with many heating methods. The low volume fractions are made possible by aligning nickel particles into chains under a magnetic field and polarized vibration. The requirement that the particles be magnetic however limits the selection of particle materials and precludes many traditional dopants such as carbon black. Such dopants could however be used to increase the diffusivity of the composite, further reducing the transition time by decreasing temperature gradients in the polymer. The composite's increase in resistivity with increasing temperature was characterized and utilized experimentally to aid in uniformly heating the sample and as a thermoelectric switch signaling when the sample had reached the transition temperature. Significant differences in the time and power required to reach transition were measured and are believed to be due to variations in the quality of particle alignment within the samples. With optimization of manufacturing techniques the excess energy required over the thermal capacity of the polymer should be able to be reduced, making the presented heating method even more attractive for applications. The presented SMP heating method adds minimal additional weight, is simple to manufacture, results in uncomplicated designs, is low cost, and results in a relatively uniform temperature making it ideal for many shape memory polymer applications.

3.4   Material Characterization

Characterization of the material used in the presented study is detailed in the published interim report: FA8650-09-D-3944 Interim Report. Below is a brief synopsis of the conclusions.

3.4.1   SMP Characterization

The SMP infill used to experimentally validate the model is a two part epoxy consisting of 7.28 g EPON 826 to 2.3 g Jeffamine D-230 published by Xie and Rousseau [41]. The hand-mixed resin is placed in a medium vacuum to remove air bubbles and cured in an oven at 100 °C for 3 hours in an open Teflon® mold. Dogbone samples were cut from sheets of neat SMP according to ASTM standard D638 and tested in a screw-driven MTS ATest/1L tensile machine with an MTS 50 lb_f load cell. An MTS 634-11E-24 laser extensometer was used to measure strain with two thermocouples measuring air and sample temperature. Heat was supplied to a closed insulated chamber via a variable voltage source, electric resistance in-line heater, and compressed house air. The sample was allowed to reach equilibrium at each temperature for approximately five minutes before testing. Samples 6mm wide by 2.5-mm thick with 50-mm gage lengths were tested at a strain rate of approximately 1.5 $^{\%}/_{min}$. The modulus of the polymer was then calculated at various temperatures and fit with a modified Heaviside function to determine the cold and hot state moduli and glass transition temperature, T_g. Results are listed in Table 4. Experimental error values where appropriate to report represent 95% confidence intervals. Shear tests on neat SMP were also conducted using the fixture and method described below.

Table 4: Epoxy SMP Experimental Results

Material Property	Value
Young's Modulus $< T_g$	1309±120 MPa
Transition Temperature	78±4 °C
Young's Modulus $> T_g$	19.04±3.1 MPa
Shear Modulus $< T_g$	1270 MPa
Shear Modulus $> T_g$	1.06 MPa

3.4.2   Honeycomb Characterization

The honeycomb utilized in the study is aluminum alloy 3003 from McMaster-Carr with the dimensions listed in Table 5.

Table 5: Experimental Honeycomb Geometry

Dimension	Value
a	5.25 mm
l	9.33 mm
d	0.044 mm
c	6.39 mm
θ	0.799 rad
E_h	73.1 GPa

Samples were cut using scissors into sheets 127 mm wide by 254 mm long at orientations of $\alpha = 0$, $^\pi/_{12}$, $^\pi/_6$, $^\pi/_4$, and $^\pi/_2$ and tested using the same MTS load frame and load cell as the SMP samples at a strain rate of 1.8 $^\%/_{min}$. A laser extensometer was used to measure strain with a gage length of approximately 50 mm. Resulting values of Young's modulus at various angles are listed in Table 6 as well as their associated 95% confidence intervals.

Table 6: Experimental Young's Moduli for Empty Honeycomb

Angle (α)	Young's Modulus (Pa)
0°	5.55E4 ± 1.17E4
15°	4.72E5 ± 0.58E5
30°	7.83E5 ± 1.30E5
45°	6.37E5 ± 0.72E5
90°	2.01E4 ± 1.83E4

Several models available in the literature capable of predicting the in-plane moduli of honeycomb are listed in Table 10. Each model is used to predict the tensile modulus of an Aluminum Alloy 3003 (Young's modulus 73.1 GPa, shear modulus 25 GPa) honeycomb with the dimensions listed in Table 5. Since the chosen shape is not a standard honeycomb where a is equal to l and θ equal to $^\pi/_3$; the moduli in the $\alpha=0$ and $^\pi/_2$ directions are not equal, as shown in Table 7.

Approved for public release; distribution unlimited.

Table 7: Comparison Between Model Predictions of Young's Modulus for Empty Honeycomb

	Young's Modulus (kPa)	
	E_0	$E_{\pi/2}$
Beblo	26.24	8.945
Masters and Evans	26.24	8.945
Abd El-Sayed, et al	26.24	8.945
Gibson and Ashby (simple)	26.24	8.946
Gibson and Ashby (full)	209.8	71.54
Experimental Values	55.5	20.1

With the exception of the unabridged model by Gibson and Ashby, all of the models give nearly identical results underestimating the experimentally determined values.

3.4.3   Composite Characterization

3.4.3.1   Experimental Composite Characterization

Honeycomb samples were cut and etched in a 23.5% nitric acid bath for 10 minutes to clean the honeycomb and promote adhesion between the aluminum and the polymer. Samples were then rinsed and dried in an oven. Epoxy SMP was prepared as above and a thin coating applied to the bottom of a Teflon mold. The aluminum honeycomb was then placed in the mold and the assembly cured in an oven at 100°C for an hour. Every other row of cells was then filled with SMP and the assembly cured for another hour. Finally, the remaining cells were filled with SMP and the completed mold cured at 100°C for an additional three hours. This process was found to reduce damage due to shrinkage during curing.

Young's modulus was measured in the $\alpha=0$ and $^\pi/_2$ directions using 127 mm by 254 mm specimens, an MTS 2.2 kip screw driven load frame with a 2,250 lb$_f$ load cell, and a laser extensometer at 1.27 $^{mm}/_{min}$ strain rate. Above T$_g$ tests were conducted using a custom insulated thermal camber, in-line electrical resistance heater, house compressed air, and two thermocouples measuring air and sample temperature.

Table 8 shows experimental Young's moduli predictions for filled honeycomb above and below T$_g$. The range of values of stiffness in various directions is significantly reduced compared to empty honeycomb as the addition of SMP has an averaging effect on the stiffness of the composite. The difference between the analytically predicted Young's modulus in the $\alpha=0$ and $^\pi/_2$ directions and the experimentally determined values are less than 6.5% and 4.3% respectively.

Table 8: Experimental Composite Young's Modulus

Direction (α)	>T_g (MPa)	<T_g (MPa)
0	33.9±4.1	2190±110
θ	NA	NA
$\pi/2$	11.8±4.2	2040±140
$\theta+\pi/2$	NA	NA

Shear specimens were 100 mm square with holes drilled ¼ inch apart in a pattern along all four sides such that the aluminum honeycomb was not damaged. Specimens were loosely bolted to a picture frame style fixture while shear deformation was measured using digital image correlation. Tests were conducted on an MTS 2.2 kip screw driven load frame with a 2,250 lb$_f$ load cell. Above T_g tests were conducted with a custom insulated chamber, in-line electric heater, house compressed air, and two thermocouples measuring air and sample temperature. A typical picture frame fixture mounted as a diamond in the load frame requires that the shear modulus of the material in the XY and YX directions be equal. Since honeycomb is anisotropic in shear, tests were conducted in a custom shear test fixture simulating pure shear. The left side of the fixture at both the top and bottom were pinned to the load frame eliminating translation in the vertical and horizontal directions while allowing rotation. The bottom right pin of the fixture was free while the top right pin was attached to the crosshead of the load frame. This setup allows characterization of both the XY and YX shear properties of the material.

Table 9: Experimental Composite Shear Modulus

Direction (α)	>T_g (MPa)	<T_g (MPa)
$0,\pi/2$	13.9±3.5	1190±130
$\pi/2,0$	13.0±2.7	1130±130

3.4.3.2 FEA Composite Characterization

Extensive FEA modeling of a unit cell of filled honeycomb was performed, the details of which are presented in the interim report with a brief synopsis below. Periodic boundary conditions were applied to a unit cell of the composite in Abaqus using the materials and material properties listed previously, the results of which are used to investigate the mechanics of the honeycomb cell and validate the experimental and analytical results and assumptions. Test cases modeling the SMP infill in both the hard and soft state were conducted in the X, Y, XY, and YX directions with periodic boundary conditions. Figure 31 shows stress in the 0° direction when the sample is subjected to strain in the 0° direction. The stress in the infill along the slanted members in Figure 31 ranges from -0.12 to 0.2 Pa nearly linearly with the stress near the center of the beam approaching zero. Such distribution validates the same assumption employed in the development of the analytical model presented subsequently.
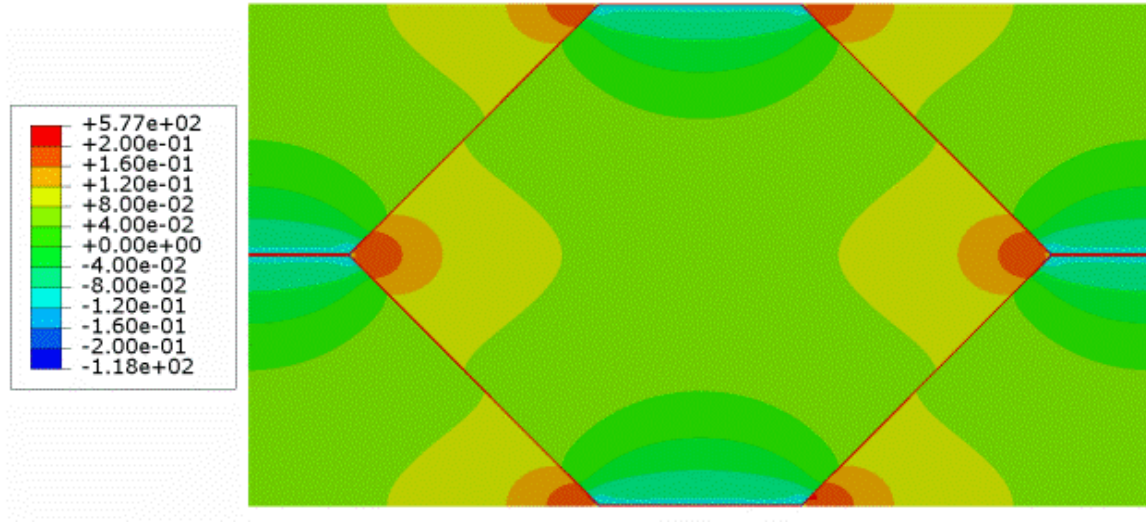
Figure 31: Stress in the 0° Direction With Soft Infill (Pa)

Figure 32 shows the stress in the infill in the π/2 direction when subjected to strains in the 0° direction. The stress along the slanted members is entirely negative and nearly uniform, correlating well with the model assumptions shown in Figure 52.
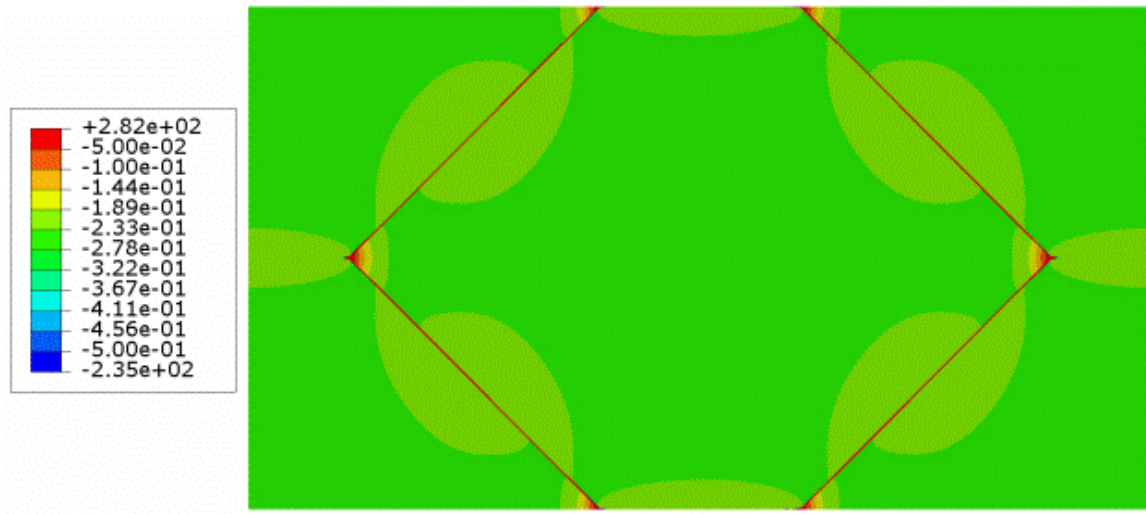
Figure 32: Stress in the π/2 Direction With Soft Infill (Pa)

The stress field as predicted by FEA can also be compared to experimental digital image correlation (DIC) results as shown in Figure 33. For clarity an orange hexagon is overlaid on the DIC results showing the approximate location of the honeycomb. Areas of high and low stress between the two results correlate well, validating the homogenization scheme and periodic boundary conditions used in the FEA.

Approved for public release; distribution unlimited.
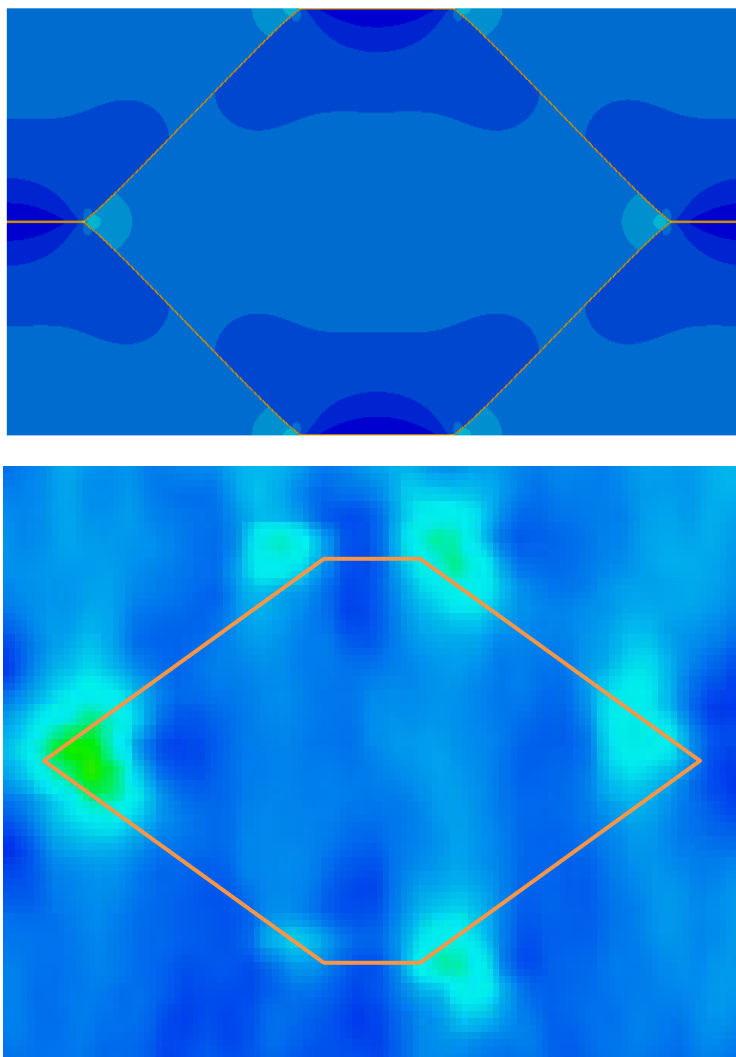
Figure 33: Top: FEA Von-Mises Stress, Bottom: DIC Experimental Von-Mises Stress

3.5 System Characterization

3.5.1 Fabrication Procedure

Fabrication of the composite panels is a multistep process ensuring electrical connectivity to each cell while isolating individual cells from neighboring cells both electrically and thermally. Each step in the process is detailed below.

Step 1

Aluminum 3003 honeycomb purchased from McMaster-Carr with dimensions listed in Table 5 is cut to the desired size using scissors. The samples are then etched for 10 minutes in a Nitric Acid solution: 1 part Fisher Scientific Nitric Acid (Certified ACS Plus 70% HNO3) to 3 parts tap water (pH 8.0). Samples are then thoroughly rinsed and allowed to air dry. This process helps to clean the honeycomb of residue and oxidation.

Figure 34: Nitric Acid Etching of Aluminum Honeycomb

Step 2

To electrically isolate the honeycomb two coats of neat Epoxy SMP are deposited on all surfaces of the honeycomb using a cotton tipped applicator. The sample is placed in a chemical hood overnight at room temperature and cured in a 100°C oven for three hours the following morning. This allows the SMP to partially set preventing excessive loss during the initial stages of curing. Alternatively, the SMP could be applied using an air brush or the sample dipped in a large container.
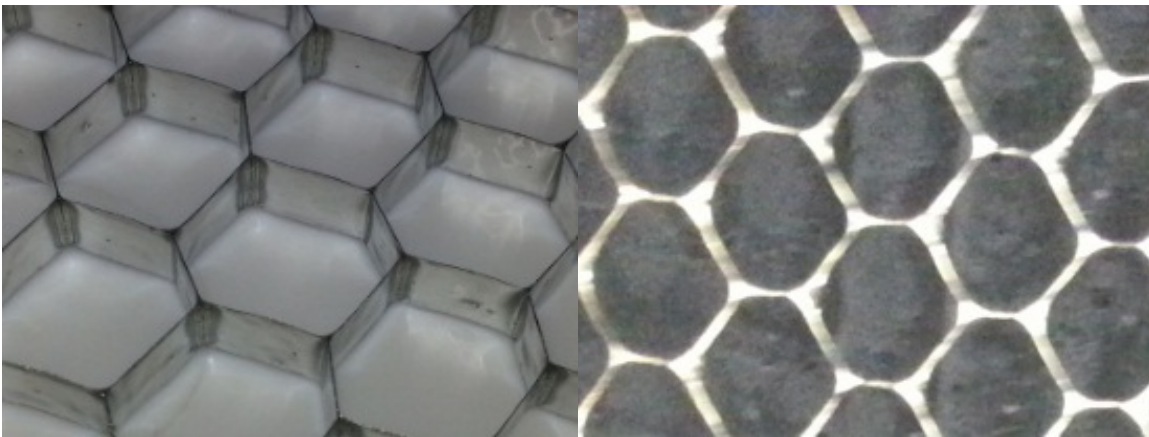
Figure 35: Aluminum Honeycomb Coated with SMP (Left) and the Resulting Cellular Separation (Right) Visible via a Backlit Sample

Step 3

Shrinkage of the SMP during curing can cause delamination between the SMP and the honeycomb with large samples. To prevent this, the honeycomb is filled in stages. Initially a thin layer of the desired SMP/Nickel composite is spread on the bottom of the mold and cured in a 100°C oven for 1.5 hours gluing the honeycomb to the mold. This allows every other row of the honeycomb to be filled and cured (with or without a magnetic field and/or vibration) allowing for shrinkage and preventing delamination.
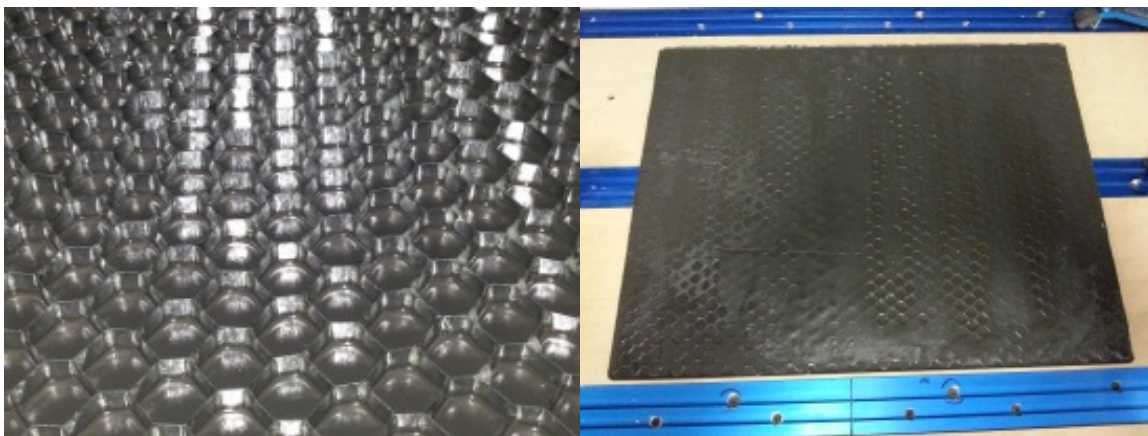
Figure 36: Honeycomb Glued to Mold Sealing the Bottom of Each Cell (Left) and a Filled Sample (Right)

Step 4

To electrically isolate each cell, channels 6.35 mm wide and 1.5 mm deep are milled along the top and bottom surfaces of the sample following the honeycomb providing electrode attachment points. These channels are then filled with neat SMP.
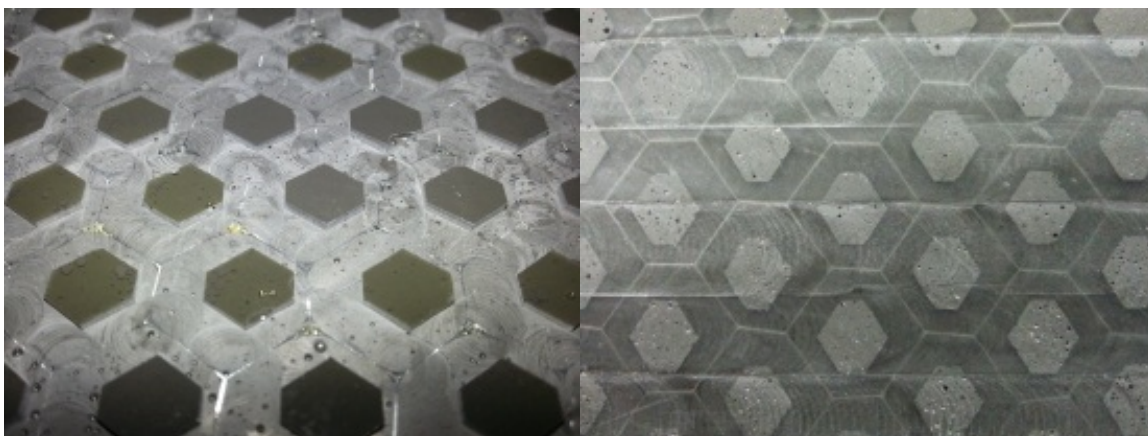
Figure 37: Electrode Attachment Points Before (Left) and After (Right) Being Backfilled with SMP

Step 5

Sheets of 100 by 100 copper mesh from McMaster-Carr are applied to the top and bottom surfaces of the sample using 10 vol% Nickel/SMP. The sample is clamped between two metal plates of similar size to the sample protected by thin Teflon sheets to prevent the sample from bonding to the plates.

Approved for public release; distribution unlimited.

Figure 38: Sample with Copper Mesh Adhered to Both Surfaces

Step 6

Individual electrodes are then fabricated by milling channels XX mm wide by YY mm deep on the top and bottom surfaces of the sample through the copper mesh following the honeycomb. A vertical column pattern is traced on one side and a horizontal row pattern is traced on the opposite side. This allows any single cell to be addressed using the standard row/column method.
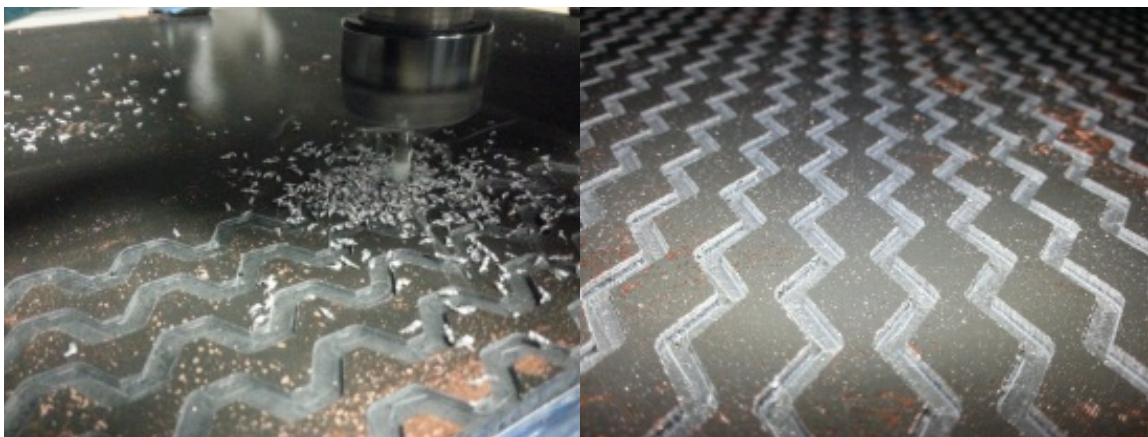
Figure 39: Milling of Row (Left) and Column (Right) Electrodes

Step 7

Finally, the traces delineating the electrodes are filled with neat SMP any required holes or other modifications to the sample are made for assembly with the test fixture. Electrical leads are soldered to each row and column of copper mesh connecting the sample to a voltage source and the sample is painted with a speckle pattern for DIC. The final sample has 48 columns and 26 rows.
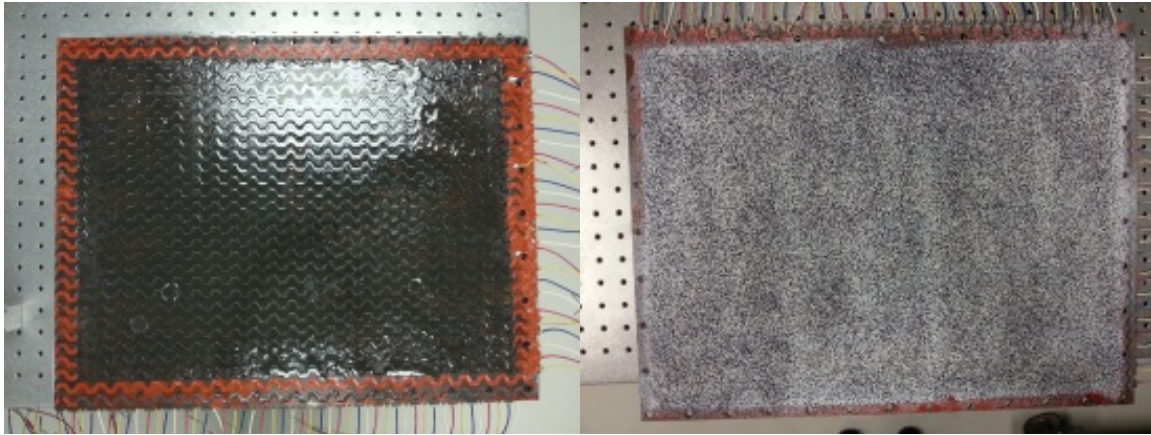
Figure 40: Final Sample with Electrode Leads Before (Left) and After (Right) a DIC Speckle Pattern is Applied

3.5.2 System Thermal Characterization

To demonstrate the functionality of the system, samples similar to those pictured in Figure 71 are connected to several National Instruments NI-9481 switch modules controlled by LabView® and a voltage source, see Figure 41. It is desired to supply samples with as much power as possible resulting in the quickest possible heating times. To prevent damage to the modules, voltage and current are limited to 41.8 V and 3.1 A. At low resistance values, current limits the amount of power that can be supplied to the sample. At high resistance values, voltage limits the power that can be supplied to the sample. Peak power is attained when both voltage and current are at their maximum allowable values when the sample has a resistance of 13.5 Ω, Figure 42. Iso-voltage and current lines are plotted against sample resistance with 40 V and 3 A highlighted.
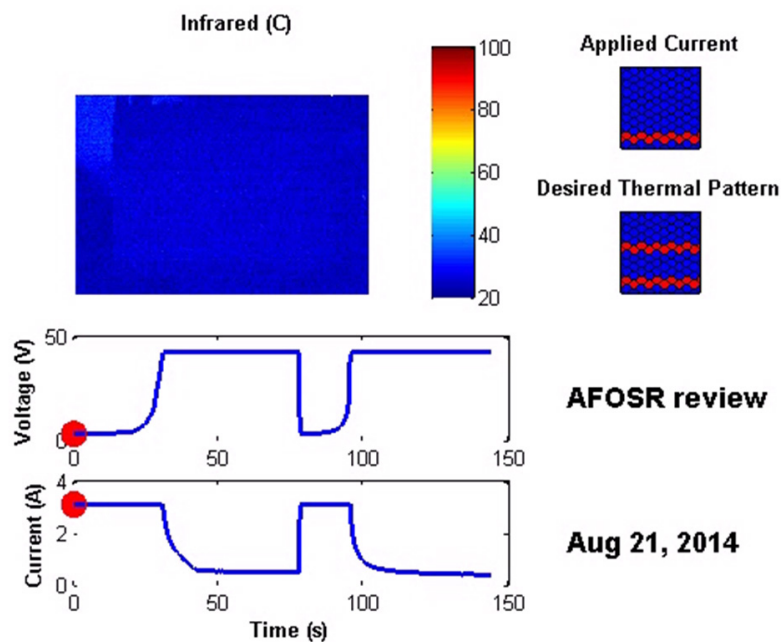
Figure 41: System Thermal Characterization Test Procedure

Approved for public release; distribution unlimited.
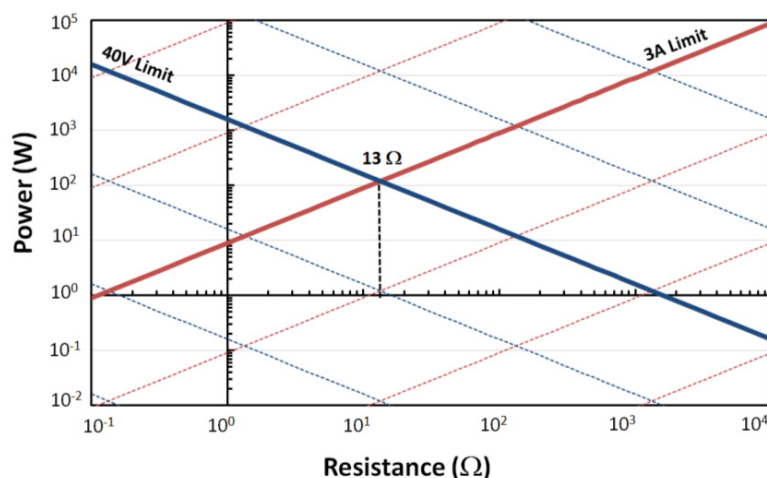
Figure 42. Power Supplied to the Sample Given Current and Voltage Limitations

Experimentally, the voltage and current can be continuously varied to deliver maximum power to the sample. When the voltage and current reach levels predetermined to correspond to a sufficiently high resistance indicating the sample has reached T_g, the current is turned off. For the example case shown in Figure 43, current is applied to sequential rows of cells of a 10- by 10-cell panel similar to pattern four in Figure 71. Initially, maximum power is achieved by maximizing the current with a low voltage. As the temperature and resistance of the sample increase, the voltage increases until the limit of the voltage source is reached at 37 seconds at which point the current begins to decrease. When the current reaches 0.4 A at 84 seconds, power is transferred to the row two rows above the first.
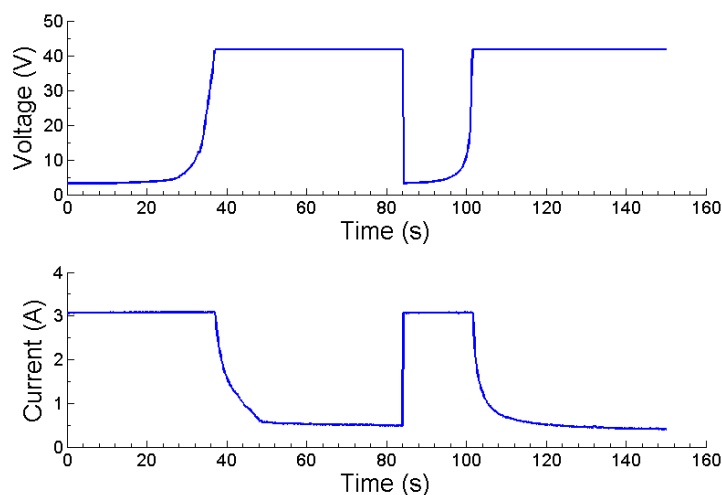
Figure 43. Demonstration of Using Increase in Resistance to Estimate Temperature

The total electrical power delivered to first row is 2125 J while 1523 J is delivered to the second row. The difference is likely attributable to differences in the quality of particle alignment and quality of the electrodes. Theoretically, increasing the temperature from ambient to 80 °C of samples 16.4 cm^2 and 6.6 mm thick should require only 907 J. From previous calculations, if 20% (181 J) of the excess energy can be attributed to the volume fraction of particles, Figure 18, the remaining 1037 J (49%) for the first row and 435 J (29%) for the second row is due to less

than ideal particle chains. It should be noted that the 10.8 cm^3 rows used here are significantly larger than the 0.5 cm^3 samples used in the previous analysis.

3.5.3   System Pressure Characterization

To verify the heating pattern models developed in Abaqus and the potential utility of the system, a full scale panel was constructed meeting MAS program dimensions. The panel was constructed using the procedure outlined previously where each cell is individually addressable. Various heating patterns were then subjected to various pressures using the custom manufactured pressure chamber in Figure 44.
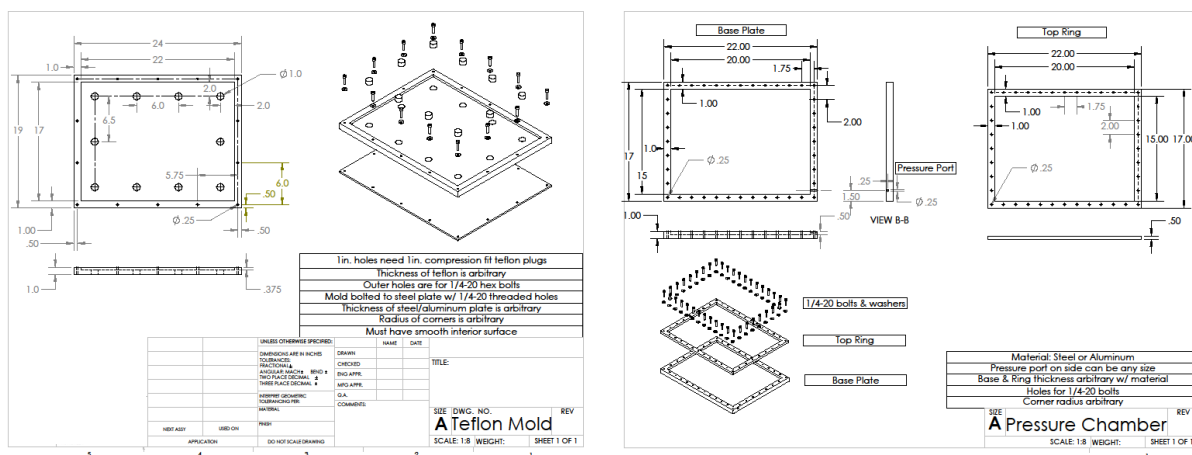
Figure 44: 15" by 20" Mold (Left) and Pressure Chamber (Right) Schematics

A full size, fully instrumented panel was subjected to an increasing uniform pressure load with various heating patterns. Full field temperature and deflection were measured and with an IR camera and DIC respectively. It should be noted that while the below results are presented as quasi-static, the temperature distribution of the sample is constantly evolving due to thermal conductance, as shown in Figure 45. Areas of cells at significantly lower temperature are also present. While each cell is individually conductive, due to the row/column method in fabricating the electrodes to reduce complexity (74 leads vs. 1249 leads) certain cells with higher resistances receive little current resulting in little temperature change.
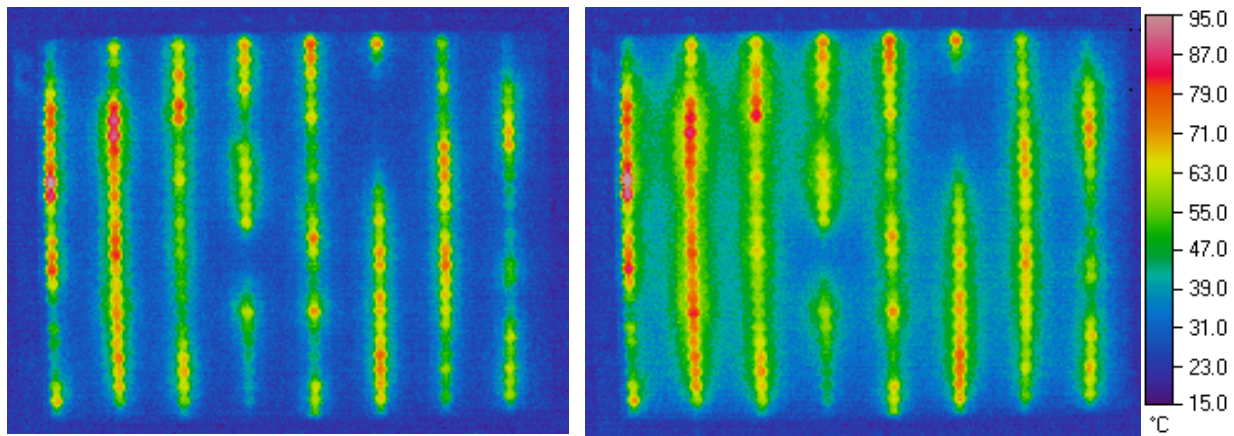
Figure 45: Infrared Images of an 8 Column Heating Pattern at the Beginning (Left) and End (Right) of a Pressure Test

For each heating pattern, current was applied to the desired cells raising their temperature before pressure was applied. The resulting thermal strains with no pressure behind the sample are shown in Figure 46 for an 8 column heating pattern. Areas of high strain clearly correlate well with areas of high temperature shown in Figure 45.
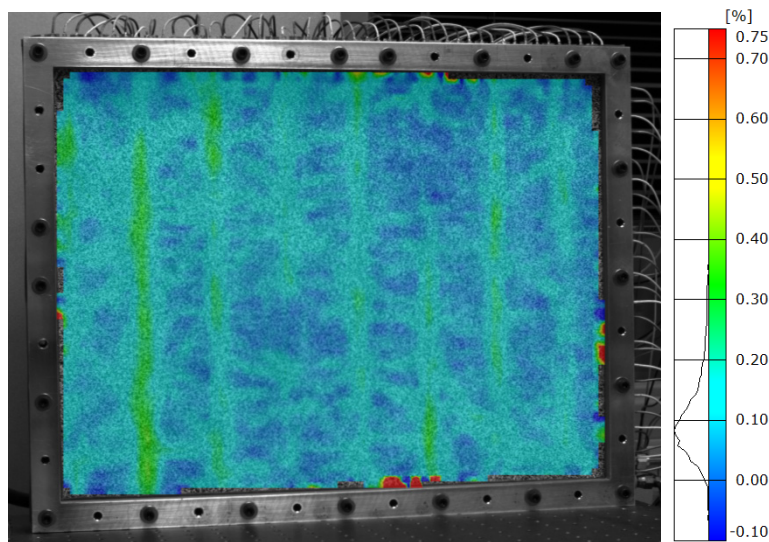
Figure 46: Thermal Strain on the Sample Before Pressure is Applied

Each heating pattern was subjected to pressures from 0 to 3.0 psi in 0.5 psi increments, exceeding the 2.78 psi threshold of the MAS program. As expected, areas of higher temperature, thus lower stiffness, bear higher strain under pressure as shown for the 8 column heating pattern in Figure 47.
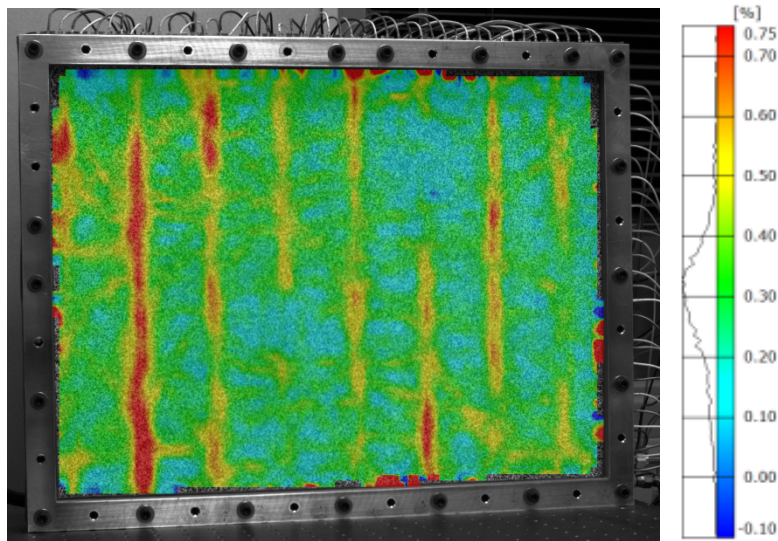
Figure 47: Major Strain on the Sample at 3.0 psi

Finally, the out of plane displacement of the sample was measured, Figure 48, with the center point deflection of the 0, 4, and 8 column heating patterns plotted with respect to pressure in Figure 49.
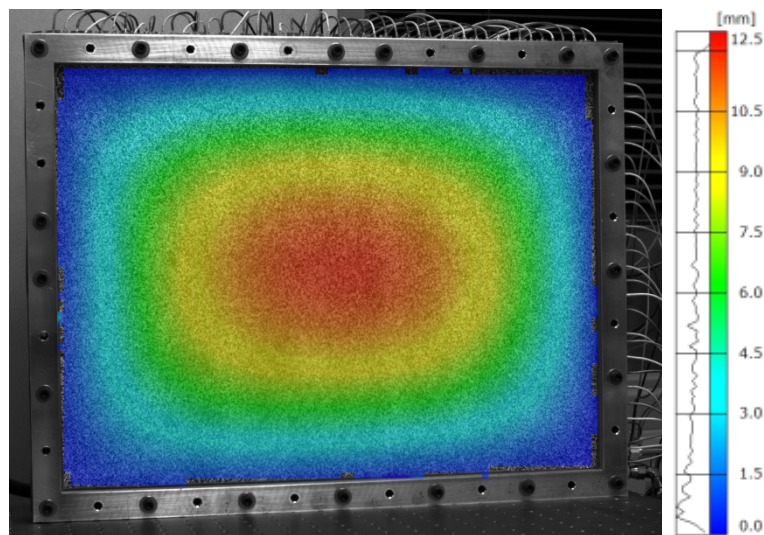
Figure 48: Z Displacement of the Sample at 3.0 psi
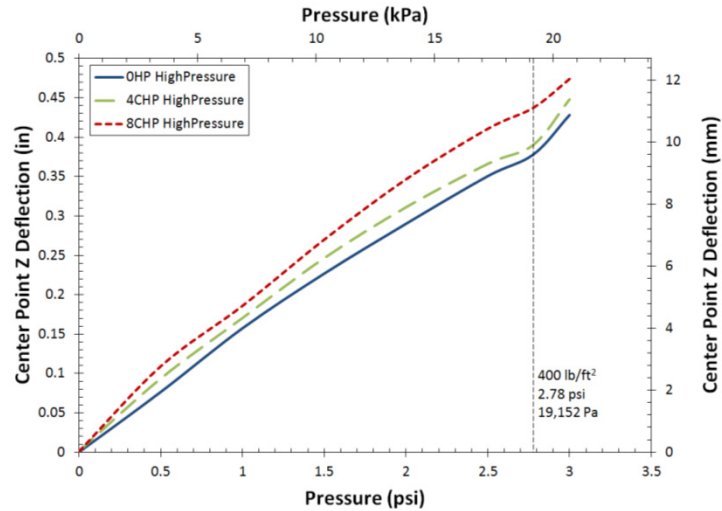
Figure 49: Center Point Deflection of a Full Size Panel Under Uniform Pressure with Various Columnar Heating Patterns

As detailed in Section 3.7.2, FEA analysis for various heating patterns can be performed yielding effective in plane stiffnesses that can be used to model the behavior of the skin in various environments. FEA of an 8 column heating pattern shown in Figure 45 results in Young's moduli of 2.63E8 and 1.02E9 Pa in the X and Y directions respectively. Flat plate theory then suggests the center point deflection of the sample under uniform pressure should be approximately double the observed experimental deflections in Figure 49. While there are many contributing factors such as sample fabrication, it is likely the areas of lower than desired temperatures, and thus higher modulus, result in a stiffer than desired sample and lower deflections. Although only columnar patterns are presented for brevity, virtually unlimited thermal patterns are attainable with the described system, such as the rows pictured in Figure 50 or the patterns analyzed performing system optimization shown in Figure 71.
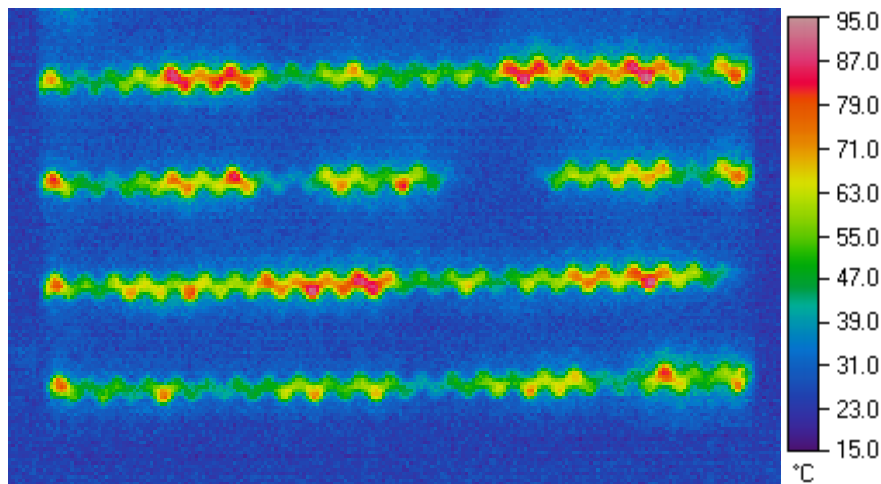
Figure 50: Infrared Images of a 4 Row Heating Pattern Temperature Profile

Finally, it should also be noted that the presented experimental investigation does not and was not intended to meet MAS requirements. The experimental panel was fabricated with available

Approved for public release; distribution unlimited.

techniques and honeycomb geometry. The test successfully demonstrates the concept of cellular heating and directionally controllable stiffness. A geometrically optimized solution meeting all MAS requirements is presented subsequently.

3.6 Honeycomb Modeling and Optimization

3.6.1 Modeling Introduction

Since analytical models describing filled honeycomb tend to be complicated and are valid only over a limited range of infill moduli, often researchers default to finite element modeling when investigating such structures. Such methods, however, have limited use in optimization. Works involving the modeling and experimental and FEA validation of filled and unfilled honeycomb and other cellular structures include those by: [42, 43, 30, 44, 45, 46, 47, 48, 49, 50] [51]

Regarding the modeling of filled honeycombs, more recent works by Gramüller, Pagitz, and Vos and their colleagues have resulted in filled and pressurized honeycomb models. In particular, Pagitz' work, inspired by the nastic movements of plants, utilizes pressure differences between honeycomb cells to achieve deformation. Their model assumes honeycomb made of rigid beams connected with springs. The properties of the structure and deformation are then calculated for various internal pressures. [52] Gramüller et al. recently used this method to demonstrate a morphing airfoil concept. [53] Similar models developed by Vos and Barrett relating the internal pressure of a honeycomb cell to mechanical work have also been used in the topology optimization of actuators for morphing leading and trailing edge flaps. Similar to Pagitz' work, changes in pressure in the honeycombs result in large scale deformation of the wing. Vos and Barrett showed that this style of analytical model correlates well with experimental results and FEA analysis. [54, 55, 56, 57] The major difference of these methods with respect to the proposed application is the forces exerted on the honeycomb walls by internal pressure differences are uniform and normal to the cell walls, neither of which hold true for solid infill.

To aid in the design and optimization of a cellular skin, it is helpful to develop an accurate analytical model of the system. The model can then be used to calculate in-plane composite mechanical properties such as Young's modulus and Poisson's ratio which in turn can be used by optimization routines. Understanding the mechanics of honeycomb and the methods used to model them are essential in developing an improved model of filled honeycomb. For this reason a brief description of three empty honeycomb models follows. The three models discussed here predicting the mechanical properties of unfilled honeycomb are listed in Table 10 (the coefficients of which are to be inserted into Equation (27) with $B_2=D_2=0$) with variable definitions shown in Figure 51. The first, by Masters and Evans, calculates the deflection of a honeycomb cell by first calculating deflection, axial strain, and shear using beam theory separately for each member before combining them into a single equation. [58] This results in the lowest predicted Young's modulus (see Table 7).

The second model, the simplified version by Gibson and Ashby, is the most widely used due to its relative accuracy and simplicity. [59] It is similar to more complicated models, except that it neglects all deformation besides bending. Although simplified, it is relatively accurate and consistent with other models. The third model presented in Table 10 is the unabridged version by Gibson and Ashby allowing for shear deformation, which has been successfully used as a basis by Olympio and Gandhi to model hybrid and accordion cellular cores. [25, 26, 27]

While there are many models that predict the properties of unfilled honeycomb, see Table 10, fewer predict the properties of filled honeycomb. Moreover, those that do are only accurate at very low infill moduli. Equation (27) is a generic model used to calculate the effective stiffness of filled honeycomb composite by separating the contributions of the honeycomb and the infill.

$$E_{cx} = B_1 E_h + B_2 E_i$$

$$E_{cy} = D_1 E_h + D_2 E_i$$

(27)

In Equation (27) E is Young's modulus, B and D are geometric coefficients listed in Table 10, subscript c represents composite quantities, h represents honeycomb quantities, i represents infill quantities, and x and y are coordinate directions. Note that this equation represents a generic model that captures the separate contribution of the infill and the honeycomb to the modulus of the combined system. This is valid for rule-of-mixtures models as well as more complicated models as described below.

Of particular interest to this work is the honeycomb mechanics model developed by Abd El-Sayed for honeycombs with a solid infill. [60, 61] Their work is the earliest presented and the bases for many other honeycomb models, including the often cited models by Gibson and Ashby. The model uses Castigliano's method to calculate the internal strain energy associated with each honeycomb member similarly to Gibson and Ashby's simplified model however includes axial deformation. Coefficients accounting for the contributions of the honeycomb and infill when modelling filled honeycomb are listed in Equation (28). El-Sayed's model predicts Young's modulus in two directions as well as Poisson's ratio in the elastic, elasto-plastic, and plastic deformation regions. The model is shown to correlate well with experimental data with an infill modulus between zero and four orders of magnitude or more lower than that of the honeycomb. The equations shown in Equations (28) through (31) were re-derived using the methods of Abd El-Sayed due to typos in the original articles.

$$B_1 = \frac{(a + x_0)}{y_0 \left(\dfrac{y_0^2 l}{d^3} + \dfrac{x_0^2}{ld} + \dfrac{a}{d} \right)}$$

(28)

$$D_1 = \frac{y_0}{(a + x_0) \left(\dfrac{x_0^2 l}{d^3} + \dfrac{y_0^2}{ld} \right)}$$

(29)

$$B_2 = \frac{K x_0^2 (a + x_0)}{2 y_0^3 (1 - v_i^2)}$$

(30)

$$D_2 = \frac{K y_0}{2 (a + x_0)(1 - v_i^2)}$$

(31)

$$K = \frac{y_0^3}{x_0^3} - \frac{ay_0^3}{x_0^4} + \frac{a^2 y_0^3}{2x_0^5} \ln\left(1 + \frac{2x_0}{a}\right) + \frac{x_0}{y_0} + \frac{a}{y_0} + \frac{2v_i y_0}{x_0}$$

El-Sayed's model provides acceptable approximations of E_{cx} and E_{cy} when E_i is much less than E_h. When E_i is relatively large, Equation (27) greatly overestimates the contribution of the infill resulting in overestimates of E_{cx} and E_{cy}. This is due primarily to the forces exerted on the beam members by the infill being non-uniformly distributed along the lengths of the honeycomb members and neglecting the resulting mechanical advantage. For this reason, a new model was developed in the same manner as the El-Sayed model to more accurately represent the internal distributed forces resulting from deformation of a filled honeycomb structure and improve the estimate of composite modulus for large values of infill modulus.

Table 10: Current Unfilled Honeycomb Model Coefficients

	B_1	D_1
Masters and Evans*	$\dfrac{(a+x_0)}{y_0\left(\dfrac{y_0^2 l}{d^3} + \dfrac{E_h y_0^2}{G_s l} + \dfrac{2al+x_0^2}{dl}\right)}$	$\dfrac{y_0}{(a+x_0)\left(\dfrac{lx_0^2}{d^3} + \dfrac{E_h x_0^2}{G_s dl} + \dfrac{y_0^2}{dl}\right)}$
ibson and Ashby simplified	$\dfrac{(a+x_0)}{y_0\left(\dfrac{y_0^2 l}{d^3}\right)}$	$\dfrac{y_0}{(a+x_0)\left(\dfrac{x_0^2 l}{d^3}\right)}$
Gibson and Ashby full**	$\dfrac{(a+x_0)}{y_0\left(\dfrac{y_0^2 l}{8d^3} + \dfrac{x_0^2}{2ld} + \dfrac{a}{d} + \dfrac{\kappa y_0^2}{2ld}\right)}$	$\dfrac{y_0}{(a+x_0)\left(\dfrac{x_0^2 l}{8d^3} + \dfrac{\kappa x_0^2}{2ld} + \dfrac{y_0^2}{2ld}\right)}$

* G_s = Honeycomb Shear Modulus
** $\kappa = 2.4 + 1.5 v_h$

3.6.2 Analytic Filled Honeycomb Model Derivation

If the honeycomb is viewed as a system comprised of beam elements rigidly connected at each end, significant mechanical advantage is generated by the infill resisting deformation of the honeycomb walls via a distributed load. Forces exerted by the infill due to strain near connection points have a much lower impact on the effective stiffness of the composite than forces far from connection points. It is postulated that neglecting this mechanical advantage is partially the cause of the limitation of low infill moduli of available models. To account for this mechanical advantage, the presented model estimates the effect of the infill by applying distributed loads directly to honeycomb beam members as functions of strain. Calculating strain energy in the infill directly is then unnecessary.

The following model predicting the effective in-plane Young's moduli of filled honeycomb is derived using thin beam theory and energy methods. Materials are assumed to be linearly elastic with each honeycomb member within the unit cell, see Figure 51, considered to be a slender beam rigidly attached at the ends.
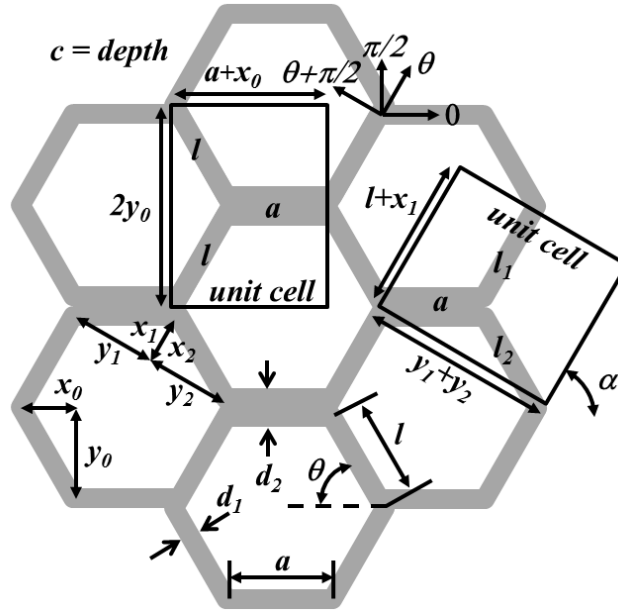
Figure 51: Honeycomb and Unit Cell Geometry and Dimensions

The majority of the external load is assumed to be carried by the honeycomb and Castigliano's method is used to calculate the force-deflection relationship of the honeycomb in each desired direction:

$$\delta_j = \sum_m \left\{ \left[\int_0^{L_m} \frac{N_m^2}{2E_m A_m} \partial z + \int_0^{L_m} \frac{M_{x,m}^2}{2E_m I_{x,m}} \partial z + \int_0^{L_m} \frac{k_m V_{y,m}^2}{2G_m A_m} \partial z \int_0^{L_m} \frac{T_m^2}{2G_m J_m} \partial z \right] \frac{\partial}{\partial f_j} \right\} \tag{32}$$

where δ is the deflection in the direction and at the point of the applied force f, m is the number of members, N is the axial load, E is Young's modulus, A is the cross-sectional area of the member, M is the moment, I is the second moment of area, k is a correction coefficient, V is the shear force, G is the shear modulus, T is the torque, and J is the polar moment of inertia. The subscript j represents the direction of the deflection being sought; in this case either 0, $^\pi/_2$, θ, or $\theta + ^\pi/_2$ shown as α in Figure 51.

$$I = \frac{cd^3}{12}$$
$$A = cd \tag{33}$$

With the unit cell corresponding to an α of 0 shown in Figure 51, the forces on the slanted and axial honeycomb segments within the unit cell are similar to those shown in Figure 52 and Figure 53.

Approved for public release; distribution unlimited.
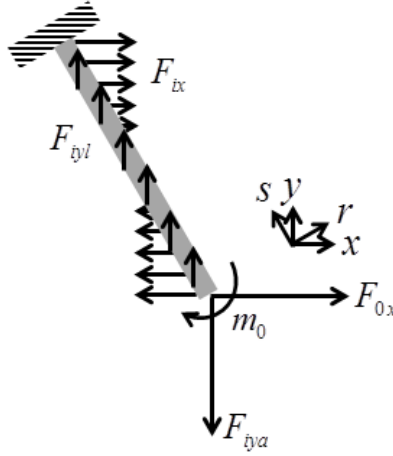
Figure 52: Forces on Slanted Members
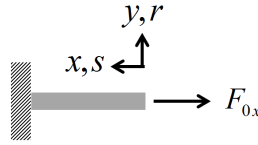
Figure 53: Forces on Horizontal Members

The subscript i indicates a force generated by straining the infill and the subscript 0 refers to an applied force. The moment m_0 is found such that a fixed end condition is imposed. Although some SMPs can exhibit nonlinear behavior, for simplicity the infill material is assumed linear here thus limiting the application of the following equations to small deflections within the linear elastic region of both the honeycomb and infill materials. At large strains, the presented equations become increasingly erroneous due to nonlinear effects and changing honeycomb geometry. The forces due to the infill in the $\alpha=0$ direction are

$$F_{0,ix}(s) = \frac{\delta_0 c E_i (l - 2s)}{l(a + 2x_0)} = F'_{0,ix} \delta_0 (l - 2s)$$

$$F_{0,iya} = \frac{\delta_0 c E_i x_0 a}{y_0^2} = F'_{0,iya} \delta_0 \tag{34}$$

$$F_{0,iyl}(s) = \frac{\delta_0 c E_i x_0^2}{2 l y_0^2} = F'_{0,iyl} \delta_0$$

The subscript i indicates a force due to the infill, x ($\alpha = 0$) or y ($\alpha = \pi/2$) indicates the direction of the force, a or l indicates the type of member the force acts on, either slanted or horizontal (see Figure 51). The remaining quantities are

$$x_0 = l\cos(\theta)$$
$$y_0 = l\sin(\theta)$$
$$\delta_{\pi/2} = \delta_0 \frac{2x_0}{y_0}$$

(35)

It should be noted that the infill also exerts shear and torque forces locally on the honeycomb members as well as the axial forces listed in Equation (34). These forces were found to have little influence on the effective stiffness of the composite and are thus neglected to simplify the equations. Decomposing the forces in Equation (34) into components in the r and s directions and neglecting torque and shear from Equation (32), the resulting deflection equation in the $\alpha=0$ direction is

$$\delta_0 = \delta_a\left(f_{0,0s}\right) + 2\delta_{l1r}\left(f_{0,0r}, f_{0,iyar}, f_{0,ixr}, f_{0,iyl1r}\right) + 2\delta_{l1s}\left(f_{0,0s}, f_{0,iyas}, f_{0,iyl1s}, f_{0,ixs}\right)$$

(36)

The subscripts a, l, $l1$, and $l2$ indicate the respective honeycomb members within the unit cell while the subscripts r and s indicate direction as shown in Figure 52 and Figure 53. In Equation (36) symmetry yields δ_{l1} and δ_{l2} are equivalent; thus, only one needs to be solved for and a factor of 2 applied. The lower case forces, f, correspond to the decomposed forces in Equations (34) in the r and s coordinate system. For example, the force deflection equation of a slanted beam due to the infill in the x direction ($F_{0,ix}$) is decomposed based on the honeycomb geometry (θ) into $f_{0,ixr}$ and $f_{0,ixs}$. Inserting the decomposed forces into Equation (36) and the rearranging terms yields the total deflection of the unit cell in the $\alpha=0$ direction:

$$\delta_0 = F_{0,0}\left[\frac{a}{Ecd_2} + \frac{ly_0^2}{2Ecd_1^3} + \frac{x_0^2}{2Ecd_1 l}\right] + F'_{0,iya}\delta_0\left[\frac{x_0 y_0}{Ecd_1 l} - \frac{lx_0 y_0}{Ecd_1^3}\right]$$
$$+ F'_{0,iyl}\delta_0\left[\frac{x_0 y_0}{2Ecd_1} - \frac{l^2 x_0 y_0}{2Ecd_1^3}\right] + F'_{0,ix}\delta_0\left[\frac{x_0^2 l}{6Ecd_1} - \frac{l^2 y_0^2}{5Ecd_1^3}\right]$$

(37)

Notice that Equation (37) is not solved for the deflection, δ_0, explicitly for clarity since the forces due to the infill are dependent upon deflection. Using Hooke's law, Equation (37), and the dimensions of the unit cell the tensile modulus in the $\alpha=0$ direction is

$$E_{c0} = \frac{\sigma}{\varepsilon} = \frac{F_{0,0}}{\delta_0}\frac{(a + x_0)}{2cy_0}$$

(38)

If the effect of the infill is ignored, Equation (38) can be simplified and shown to be equivalent to that of Abd El-Sayed shown in Table 10 and Equation (27). This method is then used to solve for the effective stiffness of the filled honeycomb in the remaining three directions: $\alpha = \{^\pi/_2, \theta,$ and $\theta+^\pi/_2\}$, the equations for which are shown in the appendix. A spline interpolation between each modulus is then used to estimate the modulus of the honeycomb/SMP composite in any direction. If the infill modulus is set to zero, the effective in-plane stiffness of empty honeycomb is captured.

A similar process can be employed to solve for the effective shear modulus of the composite. The force due to the infill is

$$F_{(0,\pi/2),iyl} = \frac{cE_i x_0}{y_0^2}\delta_0 = F'_{(0,\pi/2),iyl}\delta_0 \tag{39}$$

The force deflection equation for shear in the $\alpha = (0,\pi/2)$ direction is

$$\delta_0 = 2\delta_{lr}\left(f_{(0,\pi/2),0r}, f_{(0,\pi/2),ilr}\right) + 2\delta_{ls}\left(f_{(0,\pi/2),0s}, f_{(0,\pi/2),ils}\right) \tag{40}$$

Decomposing Equation (39) into r and s components, inserting them into Equation (40), and rearranging the terms yields:

$$\delta_0 = F_{0,0}\left[\frac{2ly_0^2}{Ecd^3} + \frac{2x_0^2}{Ecdl}\right] - \delta_0 F'_{(0,\pi/2),i}\left[\frac{l^2 x_0 y_0}{Ecd^3} - \frac{x_0 y_0}{Ecd}\right] \tag{41}$$

Using the definition of shear modulus, Equation (41), and the dimensions of the unit cell the effective shear modulus is then

$$G_{c(0,\pi/2)} = \frac{F_{0,0}}{\delta_0}\frac{2y_0}{c(a + x_0)} \tag{42}$$

This method can also be used to calculate the effective shear modulus of the filled honeycomb composite in the remaining three directions $\alpha = \{(\pi/2, 0), (\theta, \theta + \pi/2), \text{ and } (\theta, \theta + \pi/2)\}$, shown in the appendix. A spline interpolation between each point is then utilized to predict the shear modulus at any angle. If the infill modulus is set to zero, the effective in-plane shear modulus of empty honeycomb is found.

3.6.3   Analytic Filled Honeycomb Model Results

Table 11 and Figure 54 show the results of the presented analytical model predicting Young's moduli of empty honeycomb compared to the experimentally determined values at angles $\alpha = 0$, θ, $\theta + \pi/2$, and $\pi/2$. Analytical results are indicated by blue dots, a spline interpolation between data points is represented by a dotted blue line, and experimental values and their associated error bars are shown in red in Figure 54. For Figure 54 through Figure 58 the radial axis is Young's or shear modulus in MPa and the polar axis is α from Figure 51 in radians.
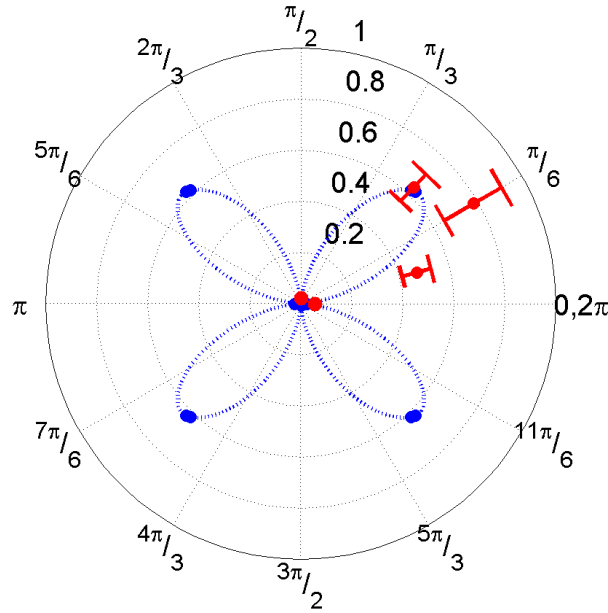
Figure 54: Empty Honeycomb Young's Modulus (MPa)

Table 11: Empty Honeycomb Young's Modulus

Direction (α)	Experimental (kPa)	Analytical (kPa)
0	55.5±11.7	26.4
$\pi/12$	472±58	206
$\pi/6$	783±130	511
θ	637±72	658
$\pi/2$	20.1±1.8	8.95
$\theta+\pi/2$	NA	667

$\theta = 0.799$ radians

Both the model and experimental data show a significant increase in stiffness in directions approaching the θ direction of the honeycomb. At an angle of $\alpha = \theta$, the applied load is axial to one of the slanted members of the honeycomb unit cell. Since the slanted members, l, are significantly longer than the horizontal members, a, and the dominant mode of deformation is bending of these members, total deformation is at a minimum when one of the slanted members is loaded axially, resulting in increased stiffness. If a standard honeycomb where the length of member a equals the length of members l and $\alpha = 60°$ is modeled, the predicted stiffness is nearly isotropic in-plane. From Figure 54 the maximum stiffness of the empty honeycomb was found to be when $\alpha = 30°$ experimentally whereas the model predicts the maximum modulus should occur at $\alpha = \theta$. There are two possible contributing factors for this discrepancy. The spline interpolation between data points (the dotted blue line in Figure 54) may be inappropriate and misleading resulting in a more pointed curve. Also, due to the geometry of the honeycomb there are large errors when measuring the modulus of the material at arbitrary angles as indicated

by the large error bars in Figure 54. It is possible that this discrepancy also occurs when the infill modulus is nonzero; however no experimental data is available.

Equations (39) through (42) are then used to calculate the shear modulus of empty honeycomb by setting the infill modulus to zero. From Table 12, the shear modulus of honeycomb follows a similar directional pattern as Young's modulus, however less pronounced.

Table 12: Empty Honeycomb Shear Modulus

Direction (α)	Analytical (kPa)
$0, \pi/2$	8.48
$\theta, \theta+\pi/2$	7.63
$\pi/2, 0$	25.4
$\theta+\pi/2, \theta$	7.58

Table 13 and Figure 55 show experimental and analytical Young's moduli predictions for filled honeycomb above T_g. The range of values of stiffness in various directions is significantly reduced compared to empty honeycomb as the addition of SMP has an averaging effect on the stiffness of the composite. The difference between the analytically predicted Young's modulus in the $\alpha=0$ and $\pi/2$ directions and the experimentally determined values are less than 6.5 and 4.3 percent, respectively.

Table 13: Composite Young's Modulus $>T_g$

Direction (α)	Experimental (MPa)	Analytical (MPa)	El-Sayed (MPa)
0	33.9±4.1	36.1	72.74
θ	NA	20.9	NA
$\pi/2$	11.8±4.2	12.3	24.80
$\theta+\pi/2$	NA	21.2	NA

$\theta = 0.799$ radians for the presented case
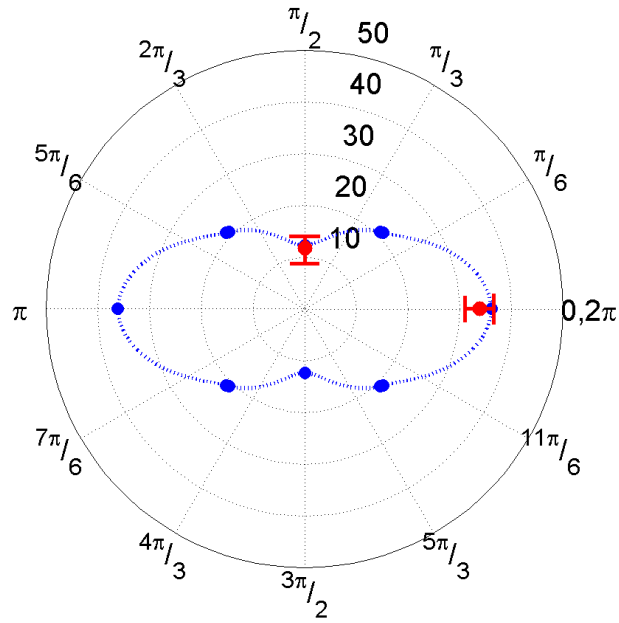
Figure 55: Composite Young's Modulus >T_g (MPa)

While the models available in the literature calculating Young's modulus of empty honeycomb are very similar to the presented model, the differences become apparent when the infill is considered. In Table 13, the filled honeycomb model by El-Sayed predicts more than double the experimentally determined composite stiffness in both the $\alpha = 0$ and $\pi/2$ directions.

When the shear modulus of the composite above T_g is graphed in a similar manner, the familiar flower shape returns. The error between the experimentally determined moduli and the presented model are 2.9% in the $(0,^\pi/_2)$ direction and 12.3% in the $(^\pi/_2,0)$ direction. The order of magnitude difference in the shear modulus of the material in the $(0,^\pi/_2)$ and $(^\pi/_2,0)$ directions compared to the $(\theta,\theta+^\pi/_2)$ and $(\theta+^\pi/_2,\theta)$ directions is believed to be due to the construction of the honeycomb. Honeycomb members a are twice as thick as members l, greatly increasing bending stiffness in certain directions.

Table 14: Composite Shear Modulus >T_g

Direction (α)	Experimental (MPa)	Analytical (MPa)
$0,^\pi/_2$	13.9±3.5	14.3
$\theta,\theta+^\pi/_2$	NA	0.230
$^\pi/_2,0$	13.0±2.7	11.4
$\theta+^\pi/_2,\theta$	NA	4.75
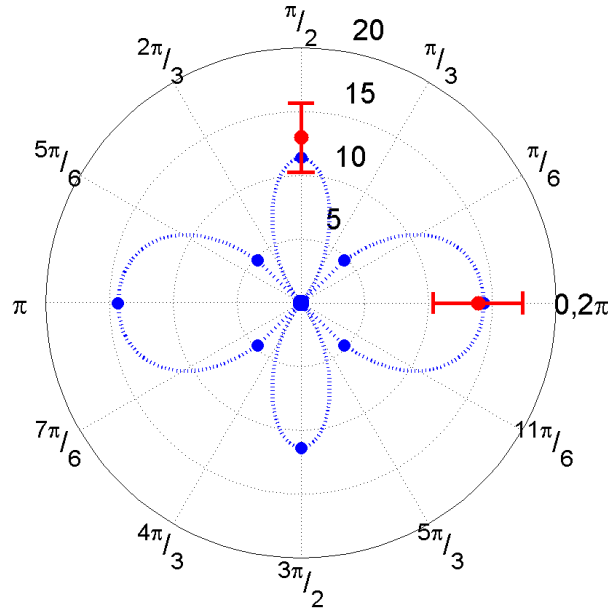
Figure 56: Composite Shear Modulus >T$_g$ (MPa)

In the cold state, the stiffness of the polymer is within 1.5 orders of magnitude of the aluminum honeycomb. When the two materials are this similar in moduli the dominant mode of deformation is no longer bending and the presented model becomes invalid. This is clearly shown in Table 15 and Figure 57, where the circular red dashed line represents the stiffness of the composite calculated using rule of mixtures. As the stiffness of the polymer approaches the stiffness of the honeycomb the composite's stiffness approaches that of a solid isotropic flat plate and rule of mixtures becomes more accurate than the presented model. In the presented case below T$_g$ rule of mixtures yields 1.86E9 Pa.

Table 15: Composite Young's Modulus <T$_g$

Direction (α)	Experimental (MPa)	Analytical (MPa)	El-Sayed (MPa)
0	2190±110	2480	4987
θ	NA	1390	NA
$\pi/2$	2040±140	846	1700
$\theta+\pi/2$	NA	1420	NA
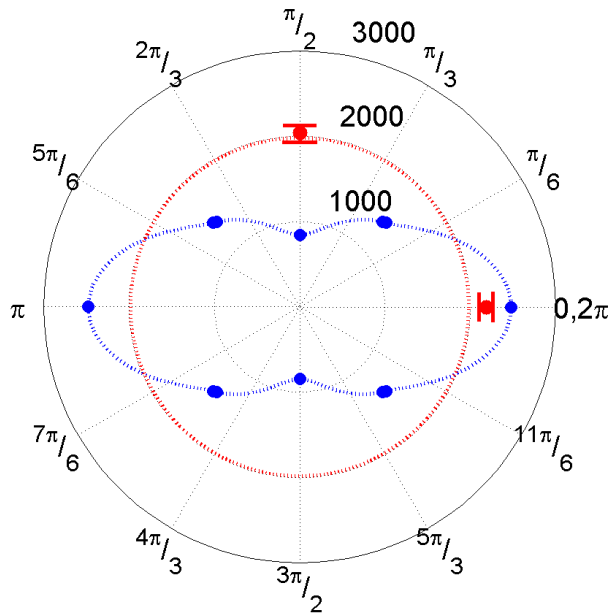
Figure 57: Composite Young's Modulus <T$_g$ (MPa)

As with Young's modulus, the error between the presented model and experimentally determined shear moduli values is much greater when the composite is below T$_g$, see Figure 58. Without further experimental investigations of the stiffness of the composite at angles other than 0 and $\square_2$ however, it is uncertain if the predicted shapes in Figure 54 through Figure 58 are realistic.
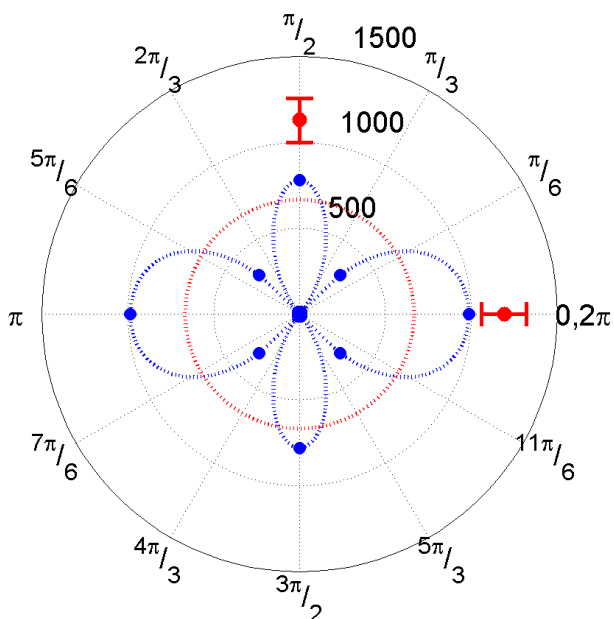
Figure 58: Composite Shear Modulus <T$_g$ (MPa)

3.6.4 Honeycomb Geometry Optimization

Using El-Sayed's equations for the equivalent Young's moduli and flat plate theory, the out of plane deflection of the honeycomb panel can be derived. The weight of the system is derived by computing the total number of cells in a panel, N.

$$N = \frac{A}{2y_o(a + x_o)} \tag{43}$$

where A is the area of the entire panel. The area of the infill and honeycomb in a unite cell is then:

$$A_I = 2(y_o - d)(x_o - d) + 2\big((a - d)(y_o - d)\big) \tag{44}$$

$$A_H = 2y_o(a + x_o) - A_I \tag{45}$$

The density of the infill and honeycomb are then used to calculate the weight (W) of the skin.

$$W = (A_I\rho_I + A_H\rho_H)cN \tag{46}$$

3.6.4.1 Optimization

The honeycomb unit cell geometry was optimized to minimize the Young's modulus in the x and y direction. This will ultimately reduce the actuation energy needed to morph the composite skin. The panel of interest was based on the MAS Phase II design requirements with dimensions of .508 x .381 m, constrained to deflect 2.5 mm in the middle of the plate when a 19,152 N/m^2 load is applied. The infill SMP has a modulus of 1.6e9 Pa, the soft state of the polymer, while the honeycomb has a modulus of 73.1 GPa.

The design variables are the horizontal wall length, a, slanted wall length, l, wall thickness d, and cell angle, θ, see Figure 51. The depth of the cell and skin weight were not included as design variables as only in plane performance was considered.

The objective of the design is to minimize Equation (47) resulting in the lowest actuation cost in both the x and y direction.

$$E_{c_x} + E_{c_y} \tag{47}$$

The cell angle was constrained to en sure the optimized design would be capable of meeting the MAS strain requirements. The cell wall thickness, d, had a lower bound constraint of 0.2 mm which is the lowest manufactured honeycomb cell wall width. The horizontal and slanted wall lengths were also given an arbitrary upper bound.

$$55° \le \theta \le 75° \tag{48}$$

$$0.2\ mm \le d \tag{49}$$

$$l, a \le 100\ mm \tag{50}$$

The weight of the panel was initially constrained by using the depth of the cell as a design variable, however it was discovered that both the weight and deflection constraints could not be simultaneously met with the infill in the soft state. The design with the lowest weight maintaining a panel center point deflection below 2.5 mm weighed 8.3 kg; significantly violating the MAS requirement.

The optimization was run with MatLAB© Optimtool. Optimtool selects the 'best' algorithm to use which was a mixture of the sequential quadratic programming, Quasi-Newton, and line search algorithms.

3.6.4.2 Optimization Results

A series of sensitivity studies were conducted by plotting E_{xc} and E_{yc} verses a set of two design variables. Figure 59 and Figure 60 look at the effect wall thickness, d, and slanted wall length, l, of the honeycomb have on the stiffness of the honeycomb in the x and y directions, E_{xc} and E_{yc}. As expected since the major mode of deformation within the honeycomb is bending, the wall thickness, d, has a large impact on the stiffness of the composite in both directions. Still significant however less drastic, shorter slanted honeycomb members result in higher stiffnesses in the x direction and at high values of d in the y direction.
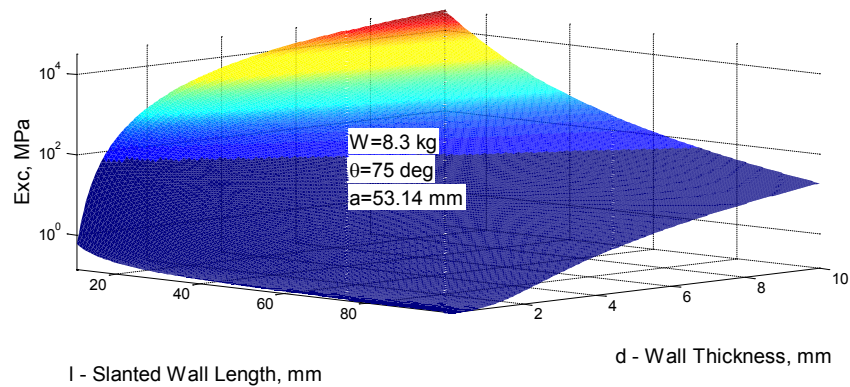
Figure 59: Young's modulus in the *x* direction, *E_{xc}*, of the optimal cell as a function of the slanted wall length, *l*, and cell wall thickness, *d*
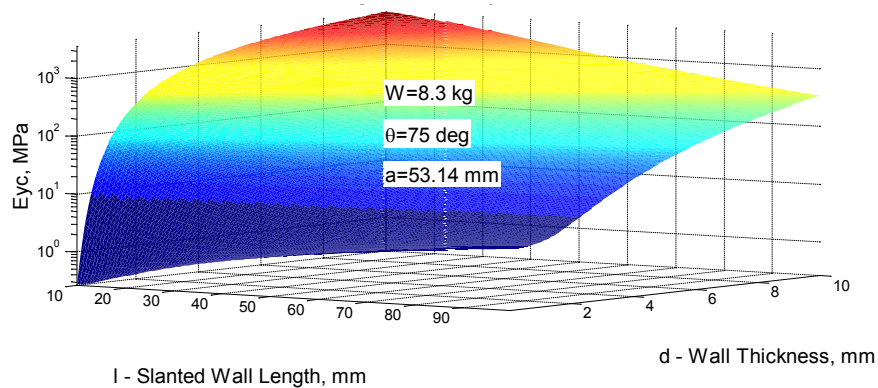
Figure 60: Young's modulus in the *y* direction, *E_{yc}*, of the optimal cell as a function of the slanted wall length, *l*, and the cell wall thickness, *d*

Figure 61 and Figure 62 show the effect of the horizontal wall length, *a*, with respect to wall thickness, *d*, on the stiffness of the composite in the x and y directions respectively. Opposite to the effect of the slanted wall length, shorter horizontal members result in less stiff geometries in the x direction. In the y direction, shorter horizontal members result in a stiffer composite.
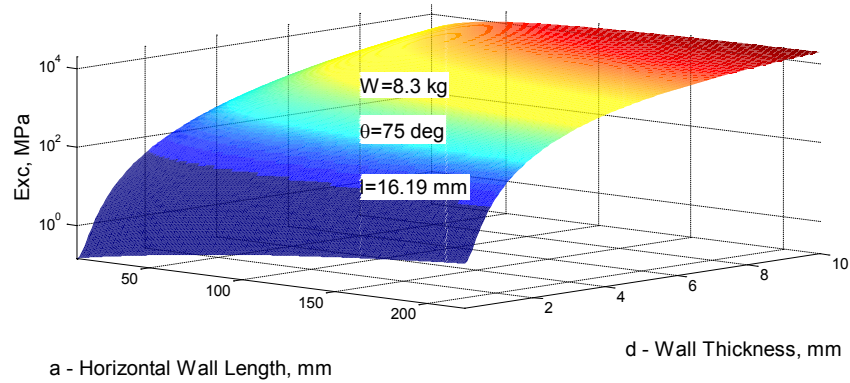
Figure 61: Young's modulus in the *x* direction, E_{xc}, of the optimal cell as a function of the horizontal wall length, *a,* and cell wall thickness, *d*
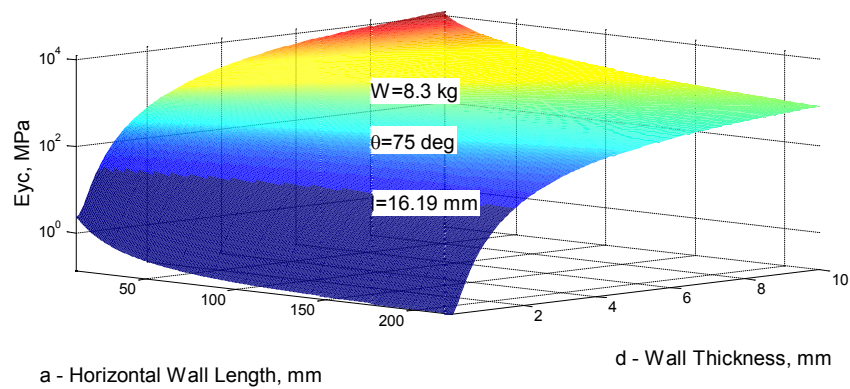
Figure 62: Young's modulus in the *y* direction, E_{yc}, of the optimal cell as a function of horizontal wall length, *a,* and cell wall thickness, *d*

Figure 63 and Figure 64 show the importance of honeycomb lengths *a* and *l* on E_{xc} and E_{yc}. In both directions, the length of the slanted member, *l*, is significantly more influential over the effective stiffness of the honeycomb than the horizontal member, *a*.
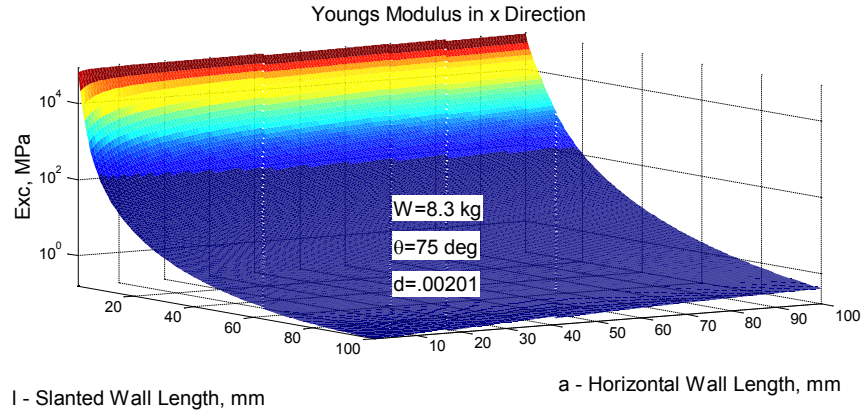
Figure 63: Young's modulus in the *x* direction, *E_xc*, of the optimal cell as a function of the slanted wall length, *l*, and cell angle, *θ*
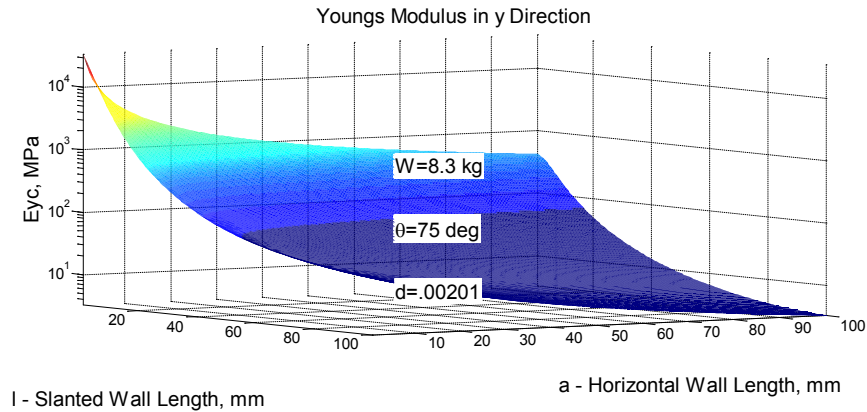
Figure 64: Young's modulus in the *y* direction, *E_xc*, of the optimal cell as a function of the slanted wall length, *l*, and cell angle, *θ*

Over the range of angles investigated ($55° < θ < 75°$), the internal honeycomb angle, $θ$, has little effect on the stiffness in the direction, E_{xc}, shown in Figure 65 and Figure 67. In the y direction, however, the angle is much more significant with larger angles resulting in higher stiffness as shown in Figure 66 and Figure 68.
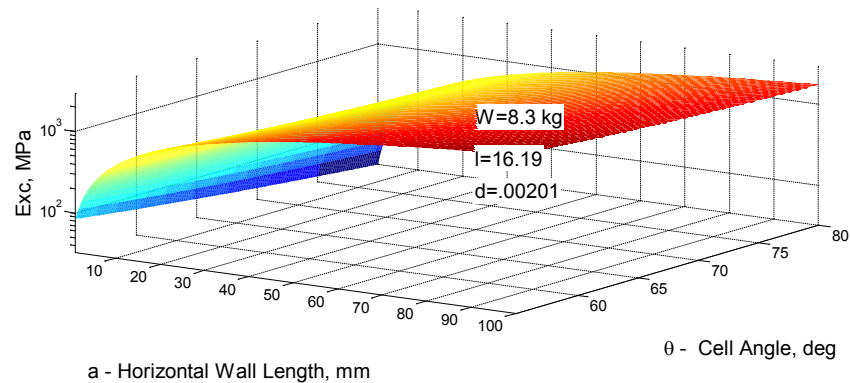
Figure 65: Young's modulus in the *x* direction, *E_xc*, of the optimal cell as a function of horizontal wall length, *a,* and cell angle, *θ*
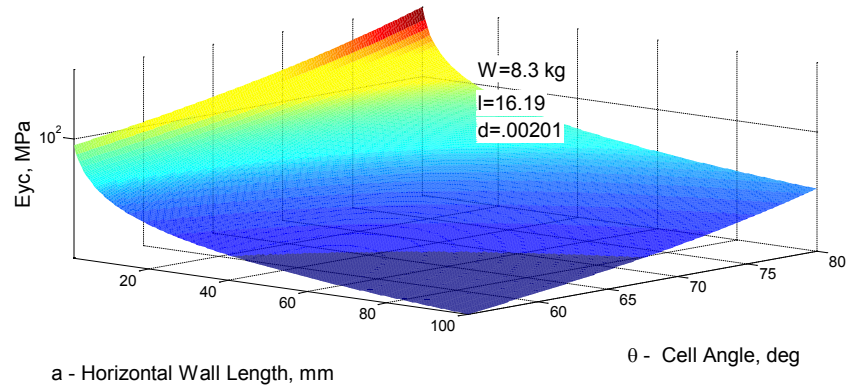
Figure 66: Young's modulus in the *y* direction, *E~yc~*, of the optimal as a function of the horizontal wall length, *a,* and cell angle, *θ*
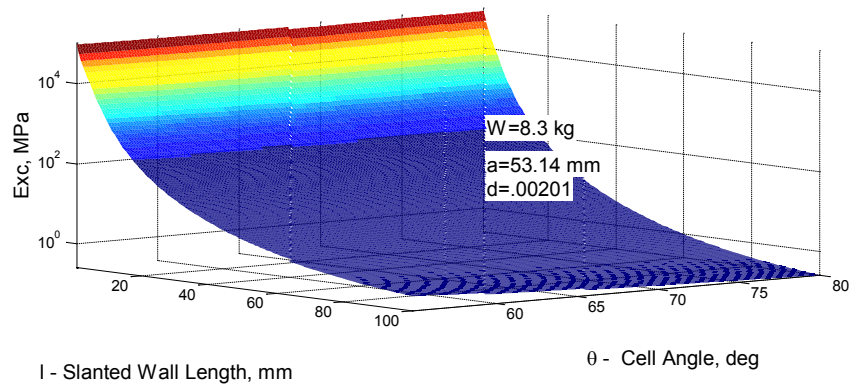
Figure 67: Young's modulus in the *x* direction, *E~xc~*, with the slanted wall length, *l,* and cell angle, *θ*
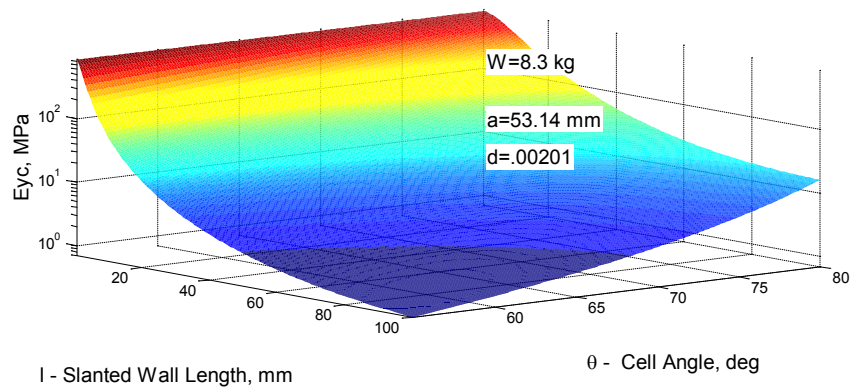
Figure 68: Young's modulus in the *y* direction, *E~yc~*, with the slanted wall length, *l,* and cell angle, *θ*
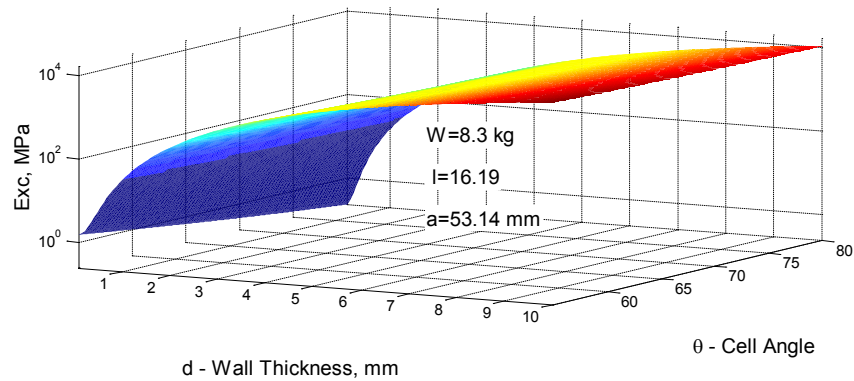
Figure 69: Young's modulus in the *x* direction, *Exc*, of the optimal cell as a function of the cell wall thickness, *d*, and cell angle, *θ*
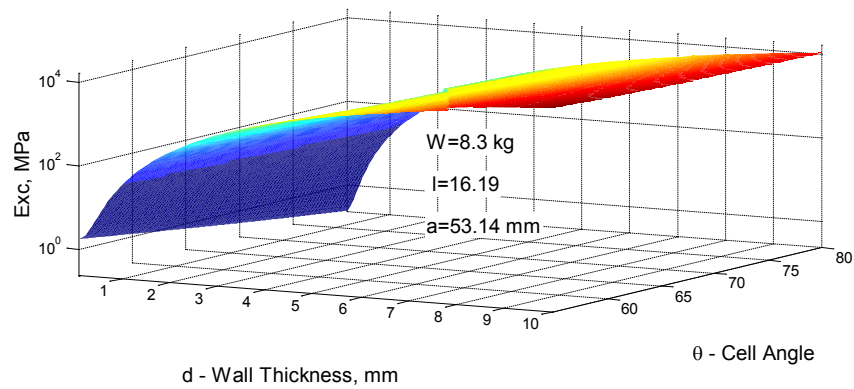
Figure 70: Young's modulus in the *y* direction, *Eyc*, of the optimal cell as a function of the cell wall thickness, *d*, and cell angle, *θ*

The sensitivity study illustrates that the largest contributing factor to the overall effective moduli of the composite is the wall thickness. Large angles of θ caused E_{yc} to increase and E_{xc} to decrease as expected.

The optimization was started at various initial starting points throughout the range of each variable producing different *l, d,* and *a* values depending on initial conditions. The angle θ was consistently limited by the upper bound constraint. The ratio of *a:l* and *a:d* were also constant for each solution at 0.3 and 26.4 respectively. Presented in Table 16, are two sets of results. Note that the moduli and θ are the same.

Table 16: Optimal Design Points

E_{xc}	E_{yc}	θ	l	d	a
GPa	GPa	deg	mm	mm	mm
1.55	1.36	75	16.19	2.01	52.14
1.55	1.36	75	1.619	.201	5.28

3.7 System Design and Optimization

3.7.1 Heating Patterns

Honeycomb structures are inherently flexible both in-plane and in bending due to their generally thin walled construction when not paired with face sheets. The structure can be made relatively stiff, however, by filling the voids in the honeycomb with a rigid material effectively resulting in a solid sheet. If the honeycomb is filled with a thermally activated SMP material and each cell heated individually, thus providing cellular level stiffness control, the filled honeycomb composite becomes a stiffness controllable, reconfigurable skin system. Patterns of heated cells, such as those shown in Figure 71, can then be used to alter the macroscopic properties of the material.

Pattern 1   Pattern 2   Pattern 3   Pattern 4

Pattern 5   Pattern 6   Pattern 7
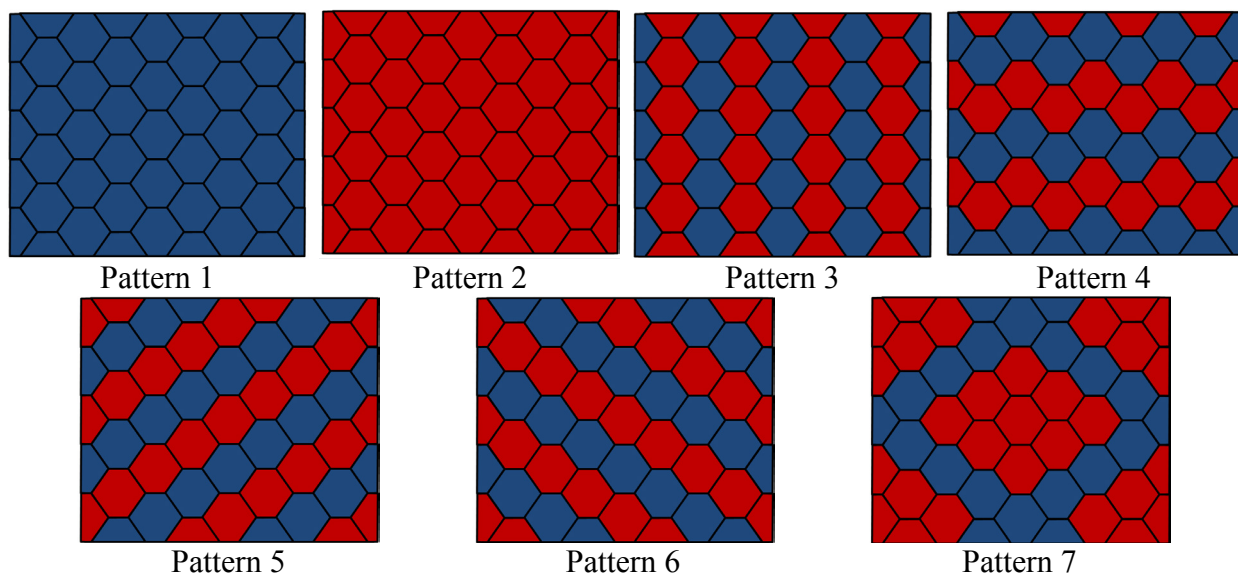
Figure 71. Honeycomb Heating Patterns

3.7.2 FEA Modeling

To estimate the effective stiffness of various heating patterns and assess their capabilities, a model that is eight cells wide by five cells high was generated in Abaqus using the geometry of the experimentally characterized honeycomb detailed previously. The aluminum honeycomb was modelled using beam elements while the SMP infill was modelled using 2D shell elements. All proper convergence studies were performed ensuring the model size, boundary conditions, and mesh densities were adequate. Each of the seven heating patterns shown in Figure 71 was modelled as well as empty honeycomb. Figure 72 is representative of the data obtained showing Pattern 7.
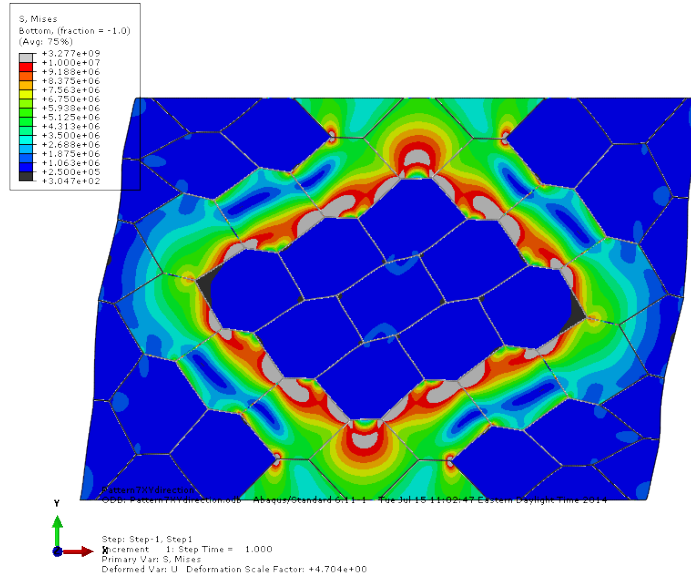
Figure 72: FEA Mises Stress Results for Pattern 7 (Figure 71) Under Shear

Numerical values for the effective stiffness in the x and y directions for epoxy and PEEK filled aluminum honeycomb are listed in Table 17 and shown in Figure 73. Material properties for the two polymers can be found in Table 18. Notably, for heating pattern three, epoxy produces a composite stiffer in the x direction than PEEK but less stiff in the y direction with the reverse true for Pattern 4. For Pattern 6, epoxy and PEEK result in nearly identical moduli in the x direction. In the y direction however, PEEK produces a modulus less than half that of epoxy. Comparing the stiffnesses produced by these two polymers clearly illustrates the complexity of material selection for the proposed system. The benefit of variable heating patterns is also clearly demonstrated when comparing the stiffnesses of patterns 3 and 4. As expected, Pattern 3 is stiff in the y direction and soft in the x while Pattern 4 is the opposite.

Table 17: FEA Predicted Effective Young's Modulus for PEEK and Epoxy Infill

		1	2	3	4	5	6	7	8
Ex	Epoxy	1.32E+09	2.53E+07	9.92E+07	5.00E+08	1.05E+08	1.01E+08	1.57E+08	1.55E+05
	PEEK	3.61E+09	6.05E+06	6.69E+07	1.31E+09	1.21E+08	1.05E+08	3.09E+08	1.55E+05
Ey	Epoxy	1.31E+09	2.01E+07	4.46E+08	7.98E+07	4.87E+07	4.93E+07	6.63E+07	5.30E+04
	PEEK	3.60E+09	2.94E+06	1.17E+09	3.72E+07	2.61E+07	2.38E+07	8.50E+07	5.30E+04
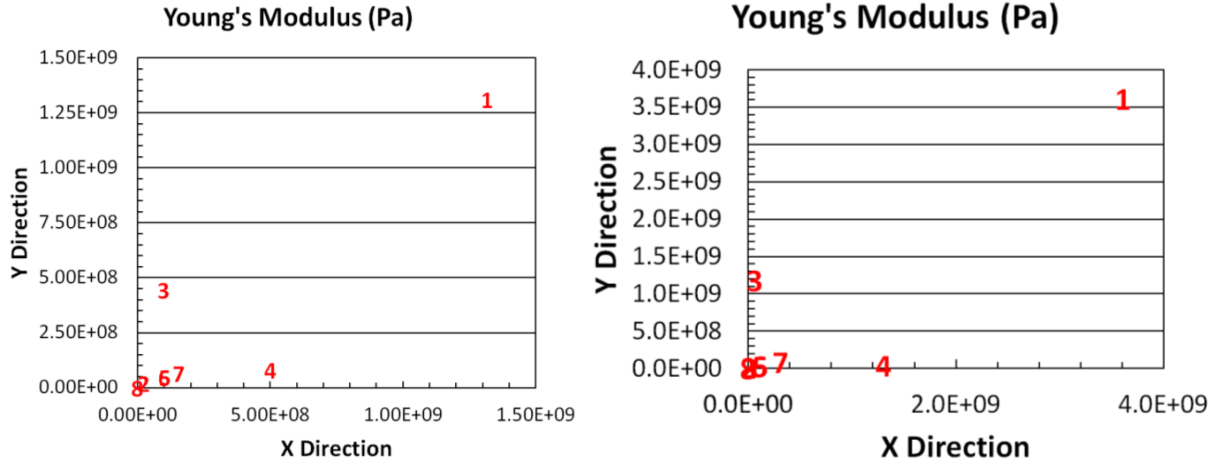
Figure 73: FEA Predicted Young's Modulus for Each Heating Pattern in the X and Y Directions for Epoxy (Left) and PEEK (Right) Filled Aluminum Honeycomb

3.7.3 Material Selection

With weight being the most limiting factor in the design, material specific strength is an important material property. Several shape memory polymers as well as silicone rubber are listed in Table 18 with their associated transition temperatures, densities, stiffnesses, and specific strengths. The highest listed specific strength in the cold state is PEEK indicating this material could result in the lowest weight. CRG's Veriflex and VeriflexE have the lowest specific strength above T_g indicating their potential to have the lowest actuator power requirements. As indicated by the FEA analysis and skin optimization, material selection is complexly related to desired heating patterns, which are determined by desired performance characteristics of the skin. The only SMP listed that meets Altera Corporation's temperature rating for military grade devices, Table 19, is PEEK. Other factors not included in this study that would need to be considered are cost, manufacturability, reliability, maintenance, toxicity, failure modes, and environmental factors such as resistance to dirt, oxidation, and moisture.

Table 18: Specific strength of available SMPs

Name	T_g °C	ρ kg/m³	<Tg Modulus Pa	Specific Strength MPa m³/kg	>Tg Modulus Pa	Specific Strength MPa m³/kg
PEEK polyether ether ketone	143	1320	3.60E9	2.73	2.60E6	0.00197
CRG VeriflexE epoxy	100	1153	3.03E9	2.63	6.60E5	0.00057
MHI MM4510 urethane-ester	45	1200	3.00E9	2.50	4.50E6	0.00375
EPON 826/Jeffamine D230	90	1153	2.70E9	2.34	2.00E7	0.01735
polyethylene terephthalate (PET)	67-81	1380	2.8E9-4.5E9	2.029-3.261	5.00E8	0.36232
MHI MM4520 urethane-ether	45	1250	2.00E9	1.60	4.00E6	0.00320
polyurethane MM3520	36.7	1250	1.60E9	1.28	2.30E6	0.00184
CRG Veriflex polystyrene	62	920	1.14E9	1.24	4.40E5	0.00048
EPON 826/Jeffamine D230	78	1153	1.31E9	1.14	1.90E7	0.01651
silicone rubber	NA	1100-2300	1.0E6-5.0E7	0.00044-0.045	1.0E6-5.0E7	0.00043-0.045

Table 19: Altera Corporation's temperature requirements for military grade programmable logic devices

Industry	Temperature Rating
Commercial	0 – 85 °C
Industrial	-40 – 100 °C
Automotive	-40 – 125 °C
Extended	-40 – 125 °C
Military	-55 - 125 °C

3.7.4   System Optimization

In parallel with the geometry optimization presented previously, the thickness and design of the skin can also be optimized for a given objective. The above heating patterns and experimental honeycomb geometry are used for the following demonstrative case. Assuming the skin consists of an unfilled honeycomb core with filled honeycomb on the top and bottom surfaces as in Figure 74, the overall thickness of the skin and the thickness of the SMP completely describe the system.
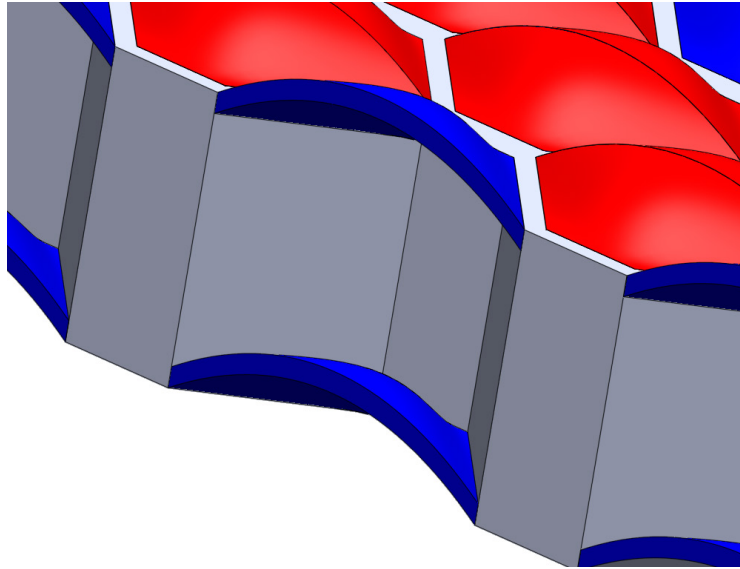
Figure 74: SMP/Honeycomb Skin Geometry Showing Unfilled Core and SMP Face Sheets

A variational solution to Huber's equation [62], Equations (A-12) through (A-19), can then be used to solve for the center point deflection of a rectangular panel with the dimensions and boundary conditions prescribed by the MAS program, Table 1. The remaining MAS requirements, namely weight, are then calculated directly and implemented as constraints.

$$D_x \frac{\partial^4 w}{\partial x^4} + 2H \frac{\partial^4 w}{\partial x^2 \partial x^2} + D_y \frac{\partial^4 w}{\partial x^4} = q \tag{51}$$

$$w = \frac{77q}{2048a^6Q}\left(4x^2 - a^2\right)^2\left(4y^2 - a^2c^2\right)^2 w_{f1} \tag{52}$$

$$Q = 25{,}025\left(c^{12}D_x^3 + D_y^3\right) + 834{,}635c^4\left(c^4D_{14} + D_{15}\right) +$$
$$129{,}740c^2\left(c^8D_{16} + D_{17}\right) + 77{,}363c^4\left(c^4D_{19} + D_{20}\right) + 7{,}436c^6H^3 \tag{53}$$

$$D_{11} = D_xD_y \qquad D_{12} = D_xH \qquad D_{13} = D_yH \qquad D_{14} = D_x^2D_y \qquad D_{15} = D_xD_y^2$$

$$D_{16} = D_x^2H \qquad D_{17} = D_y^2H \qquad D_{18} = D_xD_yH \qquad D_{19} = D_xH^2 \qquad D_{20} = D_yH^2 \tag{54}$$

$$w_{f1} = a^2w_1 + x^2w_2 + y^2w_3 \tag{55}$$

$$w_1 = 1430\left(c^8D_x^2 + D_y^2\right) + 73{,}036c^4D_{11} + 9{,}477c^2\left(c^4D_{12} + D_{13}\right) + 1183c^4H^2 \tag{56}$$

$$w_2 = 1404c^4D_{11} + 37{,}180D_y^2 + 1144c^6D_{12} + 64{,}220c^2D_{13} + 7436c^4H^2 \tag{57}$$

$$w_3 = 37{,}180c^6D_x^2 + 1404c^2D_{11} + 64{,}220c^4D_{12} + 1144D_{13} + 7436c^2H^2 \tag{58}$$

The optimization can then be executed for each of the heating patterns shown in Figure 71. Figure 75 shows the area density of the optimal design for each heating pattern for various total thicknesses. To generate Figure 75, the total thickness is prescribed and the thickness of the SMP layers is varied. The solid horizontal red line represents the maximum area density as prescribed by the MAS requirements. If the skin is required to meet all MAS requirements in any of the heating configurations except for pattern two, the best possible design is the thinnest total thickness where all patterns are below the density requirement, occurring at a total thickness of 27.8 mm. Notice that the curve for pattern two never falls below the MAS density requirement indicating that there is no geometry/skin thickness meeting both the deflection and weight requirement when the skin is entirely in the soft state. Minimum density and skin thickness designs using both PEEK and epoxy are also listed in Table 20. As expected, minimum thickness designs result in no empty honeycomb while minimum density designs result in extremely thick skins consisting of almost entirely empty honeycomb.
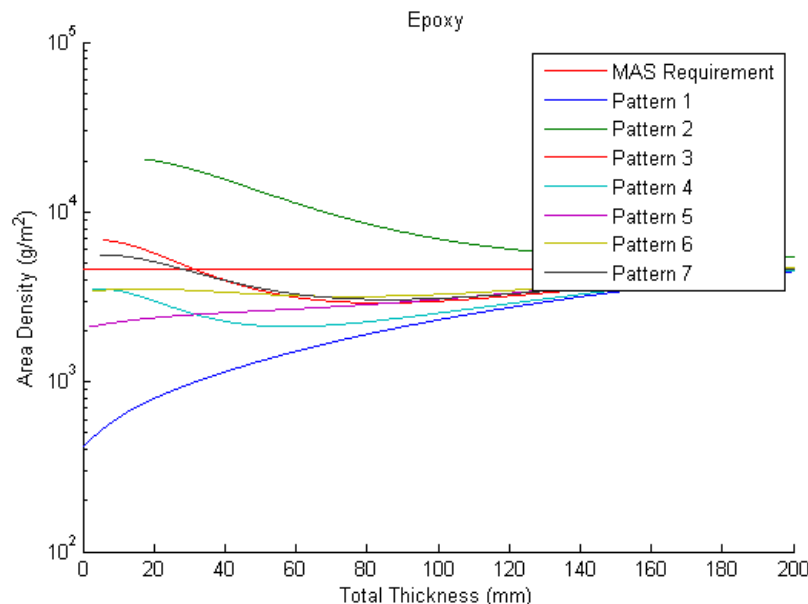
Figure 75: Optimal Skin Design Meeting MAS Requirements for Each Heating Pattern with Respect to Area Density and Total Skin Thickness

Table 20: Optimal Minimum Density, Minimum Thickness, and Best Overall Skin Designs

		Minimum Density	Minimum Thickness	Best Overall
	Limiting Pattern	3	3	3
	SMP thickness (m)	0.00032436	0.0047197	0.0014848
PEEK	Core thickness (m)	0.076249	4.86E-17	0.030099
	Max Deflection (m)	0.0025	0.0025	0.0025
	Area Density (g/m2)	2561.9942	12,568.5002	4624.4238
	Limiting Pattern	6	3	7
	SMP thickness (m)	0.00065384	0.0029169	0.0017489
Epoxy	Core thickness (m)	0.074139	5.42E-08	0.02433
	Max Deflection (m)	0.0025	0.0025	0.0025
	Area Density (g/m2)	3179.6866	6818.85257	4630.266

Figure 76 highlights another design using epoxy showing the center point deflection of the panel of each heating pattern with respect to the MAS requirement of 2.5 mm. All investigated heating patterns, except for when the entire skin is soft, meet MAS requirements.

Approved for public release; distribution unlimited.
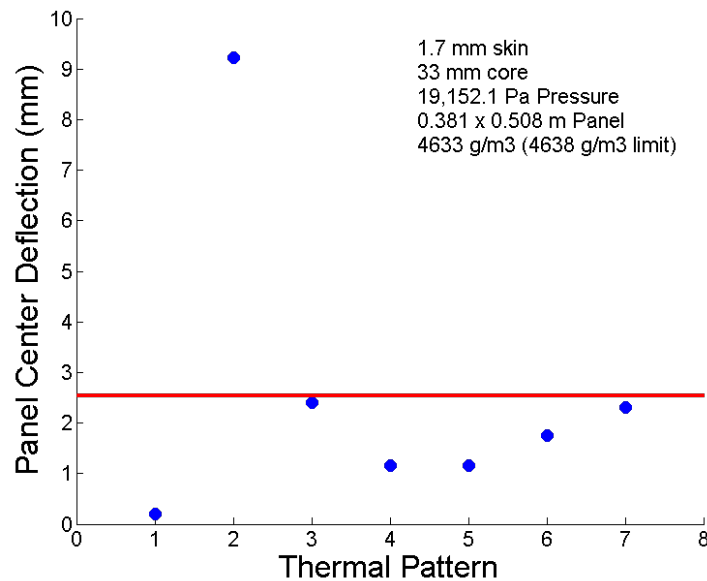
Figure 76: Panel Center Point Deflection Under Uniform Pressure for Each Heating Pattern

3.8 Reconfigurable Skin System Design Conclusions

3.8.1 Technological Advances

One of the key benefits of the presented model is its ability to predict axial and shear stiffness in any direction. The equations can easily be incorporated into an optimization scheme to take advantage of the anisotropies that occur with honeycomb geometries having different *a* and *l* member lengths. Designs such as those that maintain axial stiffness while minimizing shear strength in certain directions are easily envisioned. Currently available models calculating the in-plane stiffness of filled honeycomb have been shown to be inaccurate at infill moduli approaching that of epoxy shape memory polymer above the glass transition temperature. The presented experimental data, however, for filled honeycomb above T_g correlates well with moduli calculated from Equations (38) and (42). This suggests that modeling the composite as a mechanism where the effect of the infill manifests as a linearly distributed load along honeycomb members is appropriate. While deformation due to shear and torque and non-perfect geometric conditions such as rounded edges and non-perfectly bonded layers are neglected, the presented equations are sufficiently complex to capture the physics of the deformation experienced by the composite above T_g. As the infill modulus approaches that of the honeycomb, however, bending no longer dominates deformation and the presented equations become invalid. In this regime, traditional rule of mixtures has been shown to be sufficiently accurate. To determine a specific limit, or more likely to define the accuracy of the model with respect to component relative modulus, experimental data for many more infill moduli is required. With only two data points, it has only been shown here that the model is accurate at a relative stiffness of 3800:1 and inaccurate at a relative stiffness of 56:1. Also, the presented linear model is only valid for strains within the linear elastic regions of the honeycomb and infill materials. From FEA analysis of a unit cell, the strain concentration ratio or maximum infill

strain relative to the global strain was calculated to be 3.4 for small deflections, which can be used to estimate the displacement limitation of the model.

Also demonstrated was a novel heating scheme for shape memory polymer. Aligning Nickel particles into chains using linear vibrations and a uniform magnetic field was shown to produce relatively evenly spaced conductive paths through the sample. Although untested, it is believed that the presented method could be used for sample thicknesses much greater than the ones shown. The method produced quick, even heat of samples with minimal energy and minimal additional weight. Due to local thermal expansion of the SMP matrix, the nickel chains can also be used as an embedded temperature sensor. Resistance as a function of temperature was characterized and used as a thermal switch indicating when a sufficient temperature had been reached experimentally. Such functionality will reduce weight and complexity in future systems.

3.8.2 Future Work

Although many advances were made during the progress of this program, much more research is needed to fully exploit the possibilities of the proposed system. The method used to align the nickel particles creating embedded joule heating elements could benefit from more detailed modeling and optimization. Supporting technologies such as flexible electrodes and wiring need to be investigated to properly integrate the system into host vehicle platforms and to fully take advantage of the strain capabilities of the skin. More research beyond what was conducted as part of this effort is needed to increase the adhesion between the polymer and the honeycomb, which was the main failure mode of most samples. Control methods and algorithms are needed to optimally heat the SMP in a manner consistent with desired motions of the skin. More work is needed to maintain heat where it is needed preventing heat loss to the environment as well as spreading to areas of the skin where it is undesired. Such thermal diffusivity is a driving factor in the utility of the skin and the time available to reconfigure the structure under load. While there are issues that need addressed to fully exploit the potential functionality of the skin, many advances have been made during the project including the method used to heat the SMP and the models and optimization schemes developed used to map the performance of various designs that support further research and implementation of the system.

4   PROGRAM PRODUCTS

4.1   Publications

R.V. Beblo, J.J. Joo, G.W. Reich,"Joule Heating of Shape Memory Polymer with Magnetically Aligned Nickel Particles", *25th International Conference on Adaptive Structures and Technologies*, Oct 6 - 8 2014, The Hague, The Netherlands.

R.V. Beblo, J.P. Puttmann,N.E. DeLeon, J.J. Joo, G.W. Reich,"SMP Filled Honeycomb as a Reconfigurable Skin: Model and Experimental Validation", *19th International Conference on Composite Materials*, July 28 – Aug 2 2013, Montreal, Canada.

R.V. Beblo, J.J. Joo, G.W. Reich, "Aligning nickel particles for joule heating in epoxy shape memory polymer using a magnetic field and linear vibration" under consideration by the *Journal of Intelligent Material Systems and Structures*.

J.P. Puttmann, R.V. Beblo, J.J. Joo, B. Smyers, G.W. Reich,"Design of a Morphing Skin by Optimizing a Honeycomb Structure with a Two Phase Material Infill", *Smart Materials, Adaptive Structures and Intelligent Systems Conference*, Sept 19 – 21 2012, Stone Mountain, Georgia, USA

R.V. Beblo, J.P. Puttmann, J.J. Joo, G.W. Reich, "Shape memory polymer filled honeycomb model and experimental validation", *Smart Materials and Structures*, Vol. 24, No. 2, January 2015

4.2   Patents

Joo, James Jinyong; Smyers, Brain M; Reich, Gregory W; Beblo, Richard Vincent; Puttmann, John P "Spatially targeted activation of a shape memory polymer based reconfigurable skin system" provincial patent awarded

Approved for public release; distribution unlimited.

REFERENCES

[1] S. Sterbing-D'Angelo, M. Chadha, C. Chiu, B. Falk, W. Xian, J. Barelo and C. Moss, "Bat wing sensors support flight control," *Proceedings of the National Academy of Sciences,* vol. 108, no. 27, pp. 11291-11296, 2011.

[2] C. Ray, "Modeling, control, and estimation of flexible, aerodynamic structures," Oregon State University, 2012.

[3] T. Shimozawa, J. Mirakami and T. Kumagai, "Cricket wind receptors: thermal noise for the highest sensitivity known," *Sensors and Sensing in Biology and Engineering,* pp. 145-157, 2003.

[4] H. Barlow, "Redundancy reduction revisited," *Network: Computation in Neural Systems,* vol. 12, no. 3, pp. 241-253, 2001.

[5] M. Lungarella and O. Sporns, "Mapping information flow in sensorimotor networks," *PLoS Computational Biology,* vol. 2, no. 10, p. 144, 2006.

[6] G. Bekey, "Autonomous Robots: From Biological Inspiration to Implementation and Control," *Intelligent Robotics and Autonomous Agents Series, MIT Press,* 2005.

[7] S. Mangalam, "Phenomena based real time aerodynamic measurement system," in *IEEE Aerospace Conference*, 2003.

[8] A. Mangalam, S. Mangalam and P. Flick, "Unsteady aerodynamic observable for gust load alleviation and flutter suppression," in *26th AIAA Applied Aerodynamics Conference*, 2008.

[9] Y. Yang, N. Nguyen, N. Chen, M. Lockwood, C. Tucker, H. Hu, H. Bleckmann, C. Jiu and D. Jones, "Artificial laterial line with biomimetic neuromasts to emulate fish sensing," *Bioinspiration and Biomimetics,* vol. 5, no. 1, 2010.

[10] J. Tao and X. Yu, "Hair flow sensors from bio-inspiration to bio-mimicking - a review," *Smart Materials and Structures,* vol. 21, no. 11, 2012.

[11] T. Pitcher, B. Partridge and C. Wardle, "A blind fish can school," *Science,* vol. 194, no. 4268, pp. 963-965, 1976.

[12] J. Casas, T. Steinmann and G. Krijnen, "Why do insects have such a high density of flow sensing hairs? Insights from the hydromechanics of biomimetic MEMS sensors," *Journal of The Royal Society,* vol. 7, no. 51, pp. 1487-1495, 2010.

[13] B. Dickinson, "Hair receptor sensitivity to changes in laminar boundary layer shape," *Bioinspiration and Biomimetics,* vol. 5, no. 1, 2010.

Approved for public release; distribution unlimited.

[14] G. Krijnen, H. Droogendijk, A. Dagamseh, R. Jaganatharaja and J. Casas, "Imitating teh cricket cerecal system: The beauty of the beat with a twist of the engineer," *Advances in Science and Technology,* vol. 84, pp. 19-28, 2013.

[15] J. Keshavan and J. Humbert, "MAV stability augmentation using weighted outputs from distributed hair sensor arrays," in *Proc. of American Control Conference (ACC)*, 2010.

[16] B. Dickinson, J. Singler and B. Batten, "Mathematical modeling and simulation of biologically insired hair receptor arrarys in laminar unsteady flow separation," *Journal of Fluids and Structures,* vol. 29, pp. 1-17, 2012.

[17] M. Goman and A. Khrabrov, "State space representation of aerodynamic characteristics of an aircraft at high angles of attack," *Journal of Aircraft,* vol. 31, no. 5, pp. 1109-1115, 1994.

[18] S. Haykin, Neural networks and learning machines 3rd edition, Pearson Education, Inc., 2009.

[19] J. Zeng, B. Moulin, R. Callafon and M. Brenner, "Adaptive feedforward control for gust load alleviation," *Journal of Guidance, Control, and Dynamics,* vol. 33, no. 3, pp. 862-872, 2010.

[20] S. Haykin, Kalman Filtering and Neural Networks, Wiley Series on Adaptive and Learning Systems for Signal Processing, New York: John Wiley & Sons, Inc., 2001.

[21] L. Milne-Thomson, Theoretical Aerodynamics, Dover Publications, 1973.

[22] Z. Ren and K. Mohseni, "A model of the lateral line of fish for vortex sensing," *Bioinspiration and Biomimetics,* vol. 7, no. 3, 2012.

[23] P. Newton, The N-Vortex Problem: Analytical Techniques vol. 145, Springer, 2001.

[24] J. Puttmann, R. Beblo, J. Joo, B. Smyers and G. Reich, "Design of a Morphing Skin by Optimizing a Honeycomb Structure with a Two-Phase Material Infill," in *ASME Conference on SMASIS*, Stone Mountain, GA, 2012.

[25] K. R. Olympio and F. Gandhi, "Flexible Skins for Morphing Aircraft Using Cellular Honeycomb Cores," vol. 21, pp. 1719-1735, 2010.

[26] K. R. Olympio and F. Gandhi, "Zero Poisson's Ratio Cellular Honeycombs for Flex Skins Undergoing One-Dimensional Morphing," *Journal of Intelligent Material Systems and Structures,* pp. 1737-1753, 2010.

[27] K. R. Olympio, F. Gandhi, L. Asheghian and J. Kudva, "Design of a Flexible Skin for a Shear Morphing Wing," *Journal of Intelligent Material Systems and Structures,* 2010.

[28] G. Andersen and D. Cowan, "Aeroelastic Modeling Analysis and Testing of a Morphing Wing Structure," in *AIAA/ASME/ASCE/AHS/ASC Structres, Structural Dynamics, and Materials Conference*, Honolulu, Hawaii, 2007.

[29] C. Thill, J. Etches, I. Bond, K. Potter and P. Weaver, "Morphing Skins," *The Aeronautical Journal,* 2008.

[30] G. Murray, F. Gandhi and E. Hayden, "Polymer Filled Honeycombs to Achieve a Structural Material with Appreciable Damping," in *Structures, Structural Dynamics, and Materials Conference*, Palm Springs, CA, 2009.

[31] C. Henry and G. McKnight, "Cellular variable stiffness materials for ultra-large reversible deformations in reconfigurable structures," in *Smart Structures and Materials 2006: Active Materials*, 2006.

[32] J. Joo, G. Reich and J. Westfall, "Flexible Skin Development for Morphing Aircraft Applications via Topology Optimization," *Journal of Intelligent Material Systems and Structures,* vol. 18, no. 6, pp. 1969-1989, 2009.

[33] M. Weber and M. Kamal, "Estimation of the Volume Resistivity of Electrically Conductive Composites," *Polymer Composites,* vol. 18, no. 6, 1997.

[34] M. Weber and M. Kamal, "Microstructure and Volume Resistivity of Composites of Isotactic Polypropylene Reinforced with Electrically Conductive Fibers," *Polymer Composites,* vol. 18, no. 6, 1997.

[35] J. Leng, W. Huang, X. Lan, Y. Liu and S. Du, "Significantly reducing electrical resistivity by forming conductive Ni chains in a polyurethane shape memory polymer/carbon black composite," *Applied Physics Letters,* vol. 92, 2008.

[36] J. Leng, X. Lan, Y. Liu, S. Du, W. Huang, N. Liu, S. Phee and Q. Yuan, "Electrical conductivity of thermoresponsive shape memory polymer with embedded micron sized Ni powder chains," *Applied Physics Letters,* vol. 92, 2008.

[37] M. Kujawski, J. Pearse and E. Smela, "Elastomers filled with exfoliated graphite as compliant electrodes," *Carbon,* vol. 48, pp. 2409-2417, 2010.

[38] T. Xie and I. A. Rousseau, "Facile Tailoring of Thermal Transition Temperatures of Epoxy Shape Memory Polymers," *Polymer,* pp. 1852-1856, 2009.

[39] R. Beblo, J. Joo, B. Smyers and G. Reich, "Thermal Properties of Magnetite Nanoparticle and Carbon Fiber Doped Epoxy Shape Memory Polymer," in *ASME Conferencec on Smart Materials Adaptive*

Structures and Intelligent Systems, Phoenix, AZ, 2011.

[40] D. Lyubimov, A. Baydin and T. Lyubimova, "Particle Dynamics in a Fluid Under High Frequency Vibrations of Linear Polarization," *Microgravity Sci. Technol.,* vol. 25, pp. 121-126, 2013.

[41] T. Xie and I. A. Rousseau, "Facile tailoring of thermal transition temperatures of epoxy shape memory polymers," *Polymer,* pp. 1852-1856, 2009.

[42] W. S. Burton and A. K. Noor, "Assessment of continuum models for sandwich panel honeycomb cores," *Computer methods in applied mechanics and engineering,* vol. 145, pp. 341-360, 1997.

[43] H. X. Zhu and N. J. Mills, "The in-plane non-linear compression of regular honeycombs," *International Journal of Solids and Structures,* vol. 37, pp. 1931-1948, 2000.

[44] H. Najamoto, T. Adachi and W. Araki, "In-plane impact behavior of honeycomb structures randomly filled with rigid inclusions," vol. 36, pp. 73-80, 2009.

[45] J. W. Klintworth and W. J. Stronge, "Elasto-Plastic Yield Limits and Deformation Laws for Transversely Crushed Honeycombs," *International Journal of Mechanical Sciences,* vol. 30, pp. 273-292, 1988.

[46] V. N. Burlayenko and T. Sadowski, "Effective elastic properties of foam-filled honeycomb cores of sandwich panels," *Composite Structures,* vol. 92, pp. 2890-2900, 2010.

[47] B. Atli-Veltin and F. Gandhi, "Effect of Cell Geometry on Energy Absorption of Honeycombs Under In-Plane Compression," vol. 48, no. 2, 2010.

[48] C. W. Schwingshackl, G. S. Aglietti and P. R. Cunningham, "Determination of Honeycomb Material Properties: Existing Theories and an Alternative Dynamic Approach," *Journal of Aerospace Engineering,* pp. 177-183, 2006.

[49] C. Henry and G. McKnight, "Cellular variable stiffness materials for ultra-large reversible deformations in reconfigurable structures," *Smart Structures and Materials,* vol. 6170, 2006.

[50] X. E. Guo and L. J. Gibson, "Behavior of intact and damaged honeycombs: a finite element study," *International Journal of Mechanical Sciences,* vol. 41, pp. 85-105, 1999.

[51] D. H. Chen and S. Ozaki, "Analysis of in-plane elastic modulus for a hexagonal honeycomb core: Effect of core height and proposed analytical method," vol. 88, pp. 17-25, 2009.

[52] M. Pagitz, M. Pagitz and C. Huhne, "A modular approach to adaptive structures," vol. 9, 2014.

[53] B. Gramuller, J. Boblenz and C. Huhne, "Realization of an adaptive concept using pressure actuated

Approved for public release; distribution unlimited.

cellular structures," vol. 23, 2014.

[54] R. Vos and R. Barrett, "Mechanics of pressure-adaptive honeycomb and its application to wing morphing," vol. 20, 2011.

[55] R. Vos and R. Barrett, "Pressure Adaptive Honeycomb: A New Adaptive Structure for Aerospace Applications," in *Proc. of SPIE*, 2010.

[56] R. Vos and R. Barrett, "Pressure Adaptive Honeycomb: Mechanics, Modeling, and Experimental Investigation," in *Structures, Structural Dynamics, and Materials Conference*, Orlando, FL, 2010.

[57] R. Vos, J. Scheepstra and R. Barrett, "Topology Optimization of Pressure Adaptive Honeycomb for a Morphing Flap," in *Proc. of SPIE*, 2011.

[58] I. G. Masters and K. E. Evans, "Models for the elastic deformation of honeycombs," *Composite Structures,* vol. 35, pp. 403-422, 1996.

[59] L. J. Gibson and M. F. Ashby, Cellular Solids: Structure and Properties, 2nd ed., Cambridge, UK: The Press Syndicate of the University of Cambridge, 1997.

[60] F. K. Abd El-Sayed, R. Jones and I. W. Burgess, "A theoretical approach to the deformation of honeycomb based composite materials," *Composites,* pp. 209-214, 1979.

[61] F. K. Abd El-Sayed, "PhD Thesis," University of Sheffield, 1976.

[62] F. Mbakogu and M. Pavlovic, "Bending of orthotropic rectangular plates: a variational symbolic solution," *Computers and Structures,* vol. 77, pp. 117-128, 2000.

APPENDIX

The forces due to the infill when calculating the in-plane stiffness of the composite at angles $\alpha = \theta$, $\theta + \pi/2$, and $\pi/2$ are

$$F_{\pi/2, ix}(s) = \frac{\delta_{\pi/2} c E_i y_0 (l - 2s)}{2 x_0 l (a + 2 x_0)} = F'_{\pi/2, ix} \delta_{\pi/2} (l - 2s)$$

$$F_{\pi/2, iya} = \frac{\delta_{\pi/2} c E_i a}{2 y_0} = F'_{\pi/2, iya} \delta_{\pi/2}$$

$$F_{\pi/2, iyl1}(s) = \frac{\delta_{\pi/2} c E_i x_0}{4 l y_0} = F'_{\pi/2, iyl1} \delta_{\pi/2}$$

$$\text{(A-1)}$$

$$F_{\theta, ixa}(s) = \frac{\delta_\theta c E_i (a - 2s)}{2 a y_0} = F'_{\theta, ixa} \delta_\theta (a - 2s)$$

$$F_{\theta, ixl2}(s) = \frac{\delta_\theta c E_i (l - 2s)}{l (a + 2 x_0)} = F'_{\theta, ixl2} \delta_\theta (l - 2s)$$

$$F_{\theta, iya}(s) = \frac{\delta_\theta c E_i x_1 (x_1 y_2 + x_2 y_1)}{4 a y_0 y_1 y_2} = F'_{\theta, iya} \delta_\theta$$

$$\text{(A-2)}$$

$$F_{\theta, iyl2}(s) = \frac{\delta_\theta c E_i x_2 (x_1 y_2 + x_2 y_1)}{4 l y_0 y_1 y_2} = F'_{\theta, iyl1} \delta_\theta$$

$$F_{\theta, iyl1} = \frac{\delta_\theta c E_i l (x_1 y_2 + x_2 y_1)}{2 y_0 y_1 y_2} = F'_{\theta, iyl1} \delta_\theta$$

$$F_{(\theta+\pi/2),ixa}(s) = \frac{\delta_{(\theta+\pi/2)}cE_i y_1 y_2 (a-2s)}{2ay_0(x_1 y_2 + x_2 y_1)}$$

$$= F'_{(\theta+\pi/2),ixa}\delta_{(\theta+\pi/2)}(a-2s)$$

$$F_{(\theta+\pi/2),ixl2}(s) = \frac{\delta_{(\theta+\pi/2)}cE_i y_1 y_2 (l-2s)}{l(a+2x_0)(x_1 y_2 + x_2 y_1)}$$

$$= F'_{(\theta+\pi/2),ixl2}\delta_{(\theta+\pi/2)}(l-2s) \qquad \textbf{(A-3)}$$

$$F_{(\theta+\pi/2),iya}(s) = \frac{\delta_{(\theta+\pi/2)}cE_i x_1}{4ay_0} = F'_{(\theta+\pi/2),iya}\delta_{(\theta+\pi/2)}$$

$$F_{(\theta+\pi/2),iyl2}(s) = \frac{\delta_{(\theta+\pi/2)}cE_i x_2}{4ly_0} = F'_{(\theta+\pi/2),iyl2}\delta_{(\theta+\pi/2)}$$

$$F_{(\theta+\pi/2),iyl1} = \frac{\delta_{(\theta+\pi/2)}cE_i l}{2y_0} = F'_{(\theta+\pi/2),iyl1}\delta_{(\theta+\pi/2)}$$

When α is either θ or $\theta+\pi/2$, $l1$ indicates the honeycomb member parallel with α. The components contributing to deflection of the composite are then

$$\delta_{\pi/2} = 2\delta_{l1s}\left(f_{\pi/2,0r}, f_{\pi/2,iyar}, f_{\pi/2,iyl1r}, f_{\pi/2,ixr} \right)$$
$$+ 2\delta_{l1r}\left(f_{\pi/2,0s}, f_{\pi/2,iyas}, f_{\pi/2,iyl1s}, f_{\pi/2,ixs} \right) \qquad \textbf{(A-4)}$$

$$\delta_\theta = \delta_{l1s}\left(f_{\theta,0s} \right)$$
$$+ \delta_{l2r}\left(f_{\theta,0l2r}, f_{\theta,iyl1r}, f_{\theta,iyl2r}, f_{\theta,ixl2r} \right)$$
$$+ \delta_{l2s}\left(f_{\theta,0l2s}, f_{\theta,iyl1s}, f_{\theta,iyl2s}, f_{\theta,ixl2s} \right) \qquad \textbf{(A-5)}$$
$$+ \delta_{ar}\left(f_{\theta,0ar}, f_{\theta,iyl1r}, f_{\theta,iyar}, f_{\theta,ixar} \right)$$
$$+ \delta_{as}\left(f_{\theta,0as}, f_{\theta,iyl1s}, f_{\theta,iyas}, f_{\theta,ixas} \right)$$

$$\delta_{(\theta+\pi/2)} = \delta_{l2r}\begin{pmatrix} f_{(\theta+\pi/2),0l2r}, f_{(\theta+\pi/2),iyl1r}, \\ f_{(\theta+\pi/2),iyl2r}, f_{(\theta+\pi/2),ixl2r} \end{pmatrix}$$
$$+\delta_{l2s}\begin{pmatrix} f_{(\theta+\pi/2),0l2s}, f_{(\theta+\pi/2),iyl1s}, \\ f_{(\theta+\pi/2),iyl2s}, f_{(\theta+\pi/2),ixl2s} \end{pmatrix}$$
$$+\delta_{ar}\begin{pmatrix} f_{(\theta+\pi/2),0ar}, f_{(\theta+\pi/2),iyl1r}, \\ f_{(\theta+\pi/2),iyar}, f_{(\theta+\pi/2),ixar} \end{pmatrix}$$
$$+\delta_{as}\begin{pmatrix} f_{(\theta+\pi/2),0as}, f_{(\theta+\pi/2),iyl1s}, \\ f_{(\theta+\pi/2),iyas}, f_{(\theta+\pi/2),ixas} \end{pmatrix}$$

(A-6)

The deflection equation for each of the three directions becomes

$$\delta_{\pi/2} = 2F_{\pi/2,0}\left[\frac{y_0^2}{Ecd_1 l} + \frac{lx_0^2}{Ecd_1^3}\right] - 2F'_{\pi/2,iya}\delta_{\pi/2}\left[\frac{lx_0^2}{Ecd_1^3} + \frac{y_0^2}{Ecd_1 l}\right]$$
$$-2F'_{\pi/2,iyl}\delta_{\pi/2}\left[\frac{l^2 x_0^2}{2Ecd_1^3} + \frac{y_0^2}{2Ecd_1}\right] - 2F'_{\pi/2,ix}\delta_{\pi/2}\left[\frac{l^3 x_0 y_0}{5Ecd_1^3} - \frac{lx_0 y_0}{6Ecd_1}\right]$$

(A-7)

$$\delta_\theta = F_{\theta,0}\left[\frac{l}{Ecd_1} + \frac{n^2 ay_1^2}{Ecd_2^3} + \frac{n^2 x_1^2}{Ecd_2 a} + \frac{(1-n)^2 ly_2^2}{Ecd_1^3} + \frac{(1-n)^2 x_2^2}{Ecd_1 l}\right]$$
$$-F'_{\theta,iyl1}\delta_\theta\left[\frac{nax_1 y_1}{Ecd_2^3} + \frac{(1-n)lx_2 y_2}{Ecd_1^3} - \frac{nx_1 y_1}{Ecd_2 a} - \frac{(1-n)x_2 y_2}{Ecd_1 l}\right]$$
$$-F'_{\theta,iya}\delta_\theta\left[\frac{na^2 x_1 y_1}{2Ecd_2^3} - \frac{nx_1 y_1}{2Ecd_2}\right] - F'_{\theta,ixl}\delta_\theta\left[\frac{(1-n)lx_2^2}{6Ecd_1} + \frac{(1-n)l^3 y_2^2}{5Ecd_1^3}\right]$$
$$-F'_{\theta,ixa}\delta_\theta\left[\frac{nax_1^2}{6Ecd_2} + \frac{na^3 y_1^2}{5Ecd_2^3}\right] - F'_{\theta,iyl2}\delta_\theta\left[\frac{(1-n)l^2 x_2 y_2}{2Ecd_1^3} - \frac{(1-n)x_2 y_2}{2Ecd_1}\right]$$

(A-8)

$$\delta_{(\theta+\pi/2)} = F_{(\theta+\pi/2),0}\left[\frac{y_1^2}{Ecd_2 a} + \frac{ax_1^2}{Ecd_2^3} + \frac{y_2^2}{Ecd_1 l} + \frac{lx_2^2}{Ecd_1^3}\right] - F'_{(\theta+\pi/2),iyl1}\delta_{(\theta+\pi/2)}\left[\frac{ax_1^2}{Ecd_2^3} + \frac{lx_2^2}{Ecd_1^3} + \frac{y_1^2}{Ecd_2 a} + \frac{y_2^2}{Ecd_1 l}\right]$$
$$-F'_{(\theta+\pi/2),iya}\delta_{(\theta+\pi/2)}\left[\frac{y_1^2}{2Ecd_2} + \frac{ax_1^2}{2Ecd_2^3}\right] - F'_{(\theta+\pi/2),iyl2}\delta_{(\theta+\pi/2)}\left[\frac{y_2^2}{2Ecd_1} + \frac{lx_2^2}{2Ecd_1^3}\right]$$
$$-F'_{(\theta+\pi/2),ixa}\delta_{(\theta+\pi/2)}\left[\frac{a^3 x_1 y_1}{5Ecd_2^3} - \frac{ax_1 y_1}{6Ecd_2}\right] + F'_{(\theta+\pi/2),ixl}\delta_{(\theta+\pi/2)}\left[\frac{l^3 x_2 y_2}{5Ecd_1^3} - \frac{lx_2 y_2}{6Ecd_1}\right]$$

(A-9)

Finally, the effective modulus of the composite for each direction is then calculated using

$$E_{c\pi/2} = \frac{F_{0\pi/2}}{\delta_{\pi/2}} \frac{2y_0}{c(a + x_0)} \tag{A-10}$$

$$E_{c\theta} = \frac{F_{0\theta}}{\delta_\theta} \frac{(l + x_1)}{c(y_1 + y_2)} \tag{A-11}$$

$$E_{c(\theta+\pi/2)} = \frac{F_{0(\theta+\pi/2)}}{\delta_{(\theta+\pi/2)}} \frac{(y_1 + y_2)}{c(l + x_1)} \tag{A-12}$$

A similar process is utilized to calculate the shear modulus of the composite in each direction. When modeling shear, the forces on the honeycomb members due to the infill are

$$F_{(\pi/2,0),iyl} = \frac{cE_i}{2y_0}\delta_{\pi/2} = F'_{(\pi/2,0),iyl}\delta_{\pi/2}$$

$$G_{(\pi/2,0),iya} = \frac{2cG_i y_0}{a^2}\delta_{\pi/2} = G'_{(\pi/2,0),iya}\delta_{\pi/2} \tag{A-13}$$

$$F_{(\theta,\theta+\pi/2),iyl2a} = \frac{cE_i N}{y_1 + y_2}\delta_\theta = F'_{(\theta,\theta+\pi/2),iyl2a}\delta_\theta$$

$$N = \frac{x_1 y_2 + x_2 y_1}{y_1 y_2} \tag{A-14}$$

$$F_{(\theta+\pi/2,\theta),iyl2a} = \frac{cE_i}{y_1 + y_2}\delta_{(\theta+\pi/2)}$$
$$= F'_{(\theta+\pi/2,\theta),iyl2a}\delta_{(\theta+\pi/2)} \tag{A-15}$$

$$G_{(\theta+\pi/2,\theta),iya} = \frac{cG_i(y_1 + y_2)}{l^2}\delta_{(\theta+\pi/2)}$$
$$= G'_{(\theta+\pi/2,\theta),iya}\delta_{(\theta+\pi/2)} \tag{A-16}$$

The components contributing to the shear deflection of the composite are then

$$\delta_{\pi/2} = 2\delta_{lr}\left(f_{(\pi/2,0),ilr}, f_{(\pi/2,0),0r}\right)$$

$$+2\delta_{ls}\left(f_{(\pi/2,0),ils}, f_{(\pi/2,0),0s}\right) \tag{A-17}$$

$$+\delta_{ar}\left(f_{(\pi/2,0),iar}, f_{(\pi/2,0),0r}\right)$$

$$\delta_{\theta} = \delta_{ar}\left(f_{(\theta,\theta+\pi/2),iar}, f_{(\theta,\theta+\pi/2),0r}\right)$$

$$+\delta_{as}\left(f_{(\theta,\theta+\pi/2),ias}, f_{(\theta,\theta+\pi/2),0s}\right)$$

$$+\delta_{l2r}\left(f_{(\theta,\theta+\pi/2),il2r}, f_{(\theta,\theta+\pi/2),0r}\right) \tag{A-18}$$

$$+\delta_{l2s}\left(f_{(\theta,\theta+\pi/2),il2s}, f_{(\theta,\theta+\pi/2),0s}\right)$$

$$\delta_{\theta+\pi/2} = \delta_{ar}\left(f_{(\theta+\pi/2,\theta),iar}, f_{(\theta+\pi/2,\theta),0r}\right)$$

$$+\delta_{as}\left(f_{(\theta+\pi/2,\theta),ias}, f_{(\theta+\pi/2,\theta),0s}\right)$$

$$+\delta_{l2r}\left(f_{(\theta+\pi/2,\theta),il2r}, f_{(\theta+\pi/2,\theta),0r}\right) \tag{A-19}$$

$$+\delta_{l2s}\left(f_{(\theta+\pi/2,\theta),il2s}, f_{(\theta+\pi/2,\theta),0s}\right)$$

$$+\delta_{l1}\left(f_{(\theta+\pi/2,\theta),0r}, g_{(\theta+\pi/2,\theta),il1r}\right)$$

The deflection equation for each of the three remaining directions then becomes

$$\delta_{\pi/2} = F_{0,\pi/2}\left[\frac{lx_0^2}{2Ecd^3} + \frac{a^3}{EcD^3} + \frac{y_0^2}{2Ecdl}\right]$$

$$-\delta_{\pi/2}\left[\begin{array}{c} F'_{(\pi/2,0),iyl}\left(\dfrac{l^2 x_0^2}{2Ecd^3} + \dfrac{y_0^2}{2Ecd}\right) \\ \\ +G'_{(\pi/2,0),iya}\dfrac{a^4}{2EcD^3} \end{array}\right] \tag{A-20}$$

$$\delta_{\theta} = F_{0,\theta}\left[\frac{ay_1^2}{EcD^3} + \frac{ly_2^2}{Ecd^3} + \frac{x_1^2}{EcDa} + \frac{x_2^2}{Ecdl}\right]$$

$$-\delta_{\theta}F'_{(\theta,\theta+\pi/2),iyl2a}\left(\begin{array}{c} \dfrac{a^2 x_1 y_1}{2EcD^3} + \dfrac{l^2 x_2 y_2}{2Ecd^3} \\ \\ -\dfrac{x_1 y_1}{2EcD} - \dfrac{x_2 y_2}{2Ecd} \end{array}\right) \tag{A-21}$$

$$\delta_{\theta+\pi/2} = F_{0,\theta+\pi/2} \left[\frac{ax_1^2}{4EcD^3} + \frac{lx_2^2}{4Ecd^3} + \frac{y_1^2}{4EcDa} + \frac{y_2^2}{4Ecdl} + \frac{l}{Ecd^3} \right]$$

$$-\delta_{\theta+\pi/2} \left[F'_{(\theta+\pi/2,\theta),iyl2a} \left(\frac{a^2x_1^2}{4EcD^3} + \frac{l^2x_2^2}{4Ecd^3} + \frac{y_1^2}{4EcD} + \frac{y_2^2}{4Ecd} \right) + G'_{(\theta+\pi/2,\theta),iya} \frac{l^4}{2Ecd^3} \right]$$

(A-22)

Finally, the effective shear modulus of the composite is calculated using

$$G_{c\pi/2 0} = \frac{F_{0\pi/2}}{\delta_{\pi/2}} \frac{(a+x_0)}{2y_0 c}$$

(A-23)

$$G_{c\theta(\theta+\pi/2)} = \begin{cases} \dfrac{F_{0\theta}}{\delta_\theta} \dfrac{(y_1+y_2)}{c(l+x_1)} & x_1 > x_2 \\[2ex] \dfrac{F_{0\theta}}{\delta_\theta} \dfrac{(y_1+y_2)}{c(l+x_2)} & x_1 < x_2 \end{cases}$$

(A-24)

$$G_{c(\theta+\pi/2)\theta} = \begin{cases} \dfrac{F_{0(\theta+\pi/2)}}{\delta_{(\theta+\pi/2)}} \dfrac{(l+x_1)}{c(y_1+y_2)} & x_1 > x_2 \\[2ex] \dfrac{F_{0(\theta+\pi/2)}}{\delta_{(\theta+\pi/2)}} \dfrac{(l+x_2)}{c(y_1+y_2)} & x_1 < x_2 \end{cases}$$

(A-25)

where the components F/δ are solved for using Equations A-20 through A-22.

LIST OF SYMBOLS, ABBREVIATIONS, AND ACRONYMS

Energy-Based Reconfigurable Micro-Aerial Vehicle (MAV) Flight Structures Design

A	Reference area
B	Linearized measurement matrix
C_D	Coefficient of drag
F_x	Force along x axis
G_n	Kalman gain
M_y	Moment about y axis
P	Measurement error covariance matrix
$Q_{v,w}$	Measurement/process noise covariance matrix
W_b	Input weight matrix
W_a	Neuron connectivity weight matrix
W_b	Neuron connectivity weight matrix
W_c	Output neurons
a	Cylinder radius
b_n	Function denoting RNN
n	Time step
v	velocity normal to hair sensor
w	Vector of RNN connection weights
w	Complex potential
α	Angle of incidence of the free stream
δ	Drag
κ	Vortex strength
ρ	Density of air

Reconfigurable Skin System Design

A	Cross sectional area
A_H	Area of honeycomb in a unit cell
A_I	Area of infill in a unit cell
B_1, B_2, D_1, D_2	Geometric parameters
C_p	Heat capacity
D_x, D_y	Flexural rigidity
E_{cx}, E_{cy}	Composite Young's modulus
E_h	Honeycomb Young's modulus
E_i	Infill Young's modulus
F	Force
F_b	Buoyancy force
F_g	Gravitational force
G_s	Honeycomb shear modulus
I	Second moment of area
J	Polar moment of inertia
M	Moment
M	Magnetic force

N	Axial load
N	Number of cells in a panel
T	Temperature
T	Torque
T_g	Glass transition temperature
V	Shear force
V	Vibrational force
V_p	Particle volume
W	Skin weight
a	Vibrational amplitude
a	Horizontal wall length of honeycomb
c	Depth of honeycomb
d	Wall thickness of honeycomb
$f(r)$	Initial temperature distribution
k	Correction coefficient for shear energy
k	Thermal conductivity
l	Slanted wall length of honeycomb
m	Moment
q	Applied pressure
qin	Heat flux
r	Particle radius
t	Time
w	Panel center point deflection
α	Angle between unit cell orientation and x axis
δ	Distance between two particles
δ	deflection
ν	Poisson's ratio
θ	Interior half angle of honeycomb
ρ_f	Fluid density
ρ_p	Particle density
τ	Unit normal vector
ω	Vibrational frequency

Abbreviations and Acronyms

AFOSR	Air Force Office of Scientific Research
AFRL	Air Force Research Laboratory
DIC	Digital Image Correlation
EKF	Extended Kalman Filter
FEA	Finite Element Analysis
FEMM	Finite Element Method Magnetics
IR	Infrared
LIDAR	Laser Imaging, Detection, and Ranging
MAS	Morphing Aircraft Structures
MIMO	Multi-Input Multi-Output

NI	National Instruments
RNN	Recurrent Neural Network
SI	Système Internationale
SMP	Shape Memory Polymer
2D	Two Dimensional
UDRI	University of Dayton Research Institute